# Moving Mesh Magnetohydrodynamics: Magnetic Processes in Star Formation and Cosmology

## Citation

Mocz, Philip. 2017. Moving Mesh Magnetohydrodynamics: Magnetic Processes in Star Formation and Cosmology. Doctoral dissertation, Harvard University, Graduate School of Arts & Sciences.

# Moving mesh magnetohydrodynamics: magnetic processes in star formation and cosmology

A DISSERTATION PRESENTED
BY
PHILIP MOCZ
TO
THE DEPARTMENT OF ASTRONOMY

IN PARTIAL FULFILLMENT OF THE REQUIREMENTS
FOR THE DEGREE OF
DOCTOR OF PHILOSOPHY
IN THE SUBJECT OF
ASTRONOMY AND ASTROPHYSICS

HARVARD UNIVERSITY
CAMBRIDGE, MASSACHUSETTS
APRIL 2017

Dissertation Advisor: Lars Hernquist Philip Mocz

# Moving mesh magnetohydrodynamics: magnetic processes in star formation and cosmology

## ABSTRACT

Magnetohydrodynamic (MHD) processes are ubiquitous in our Universe. From the largest cosmological scales where primordial magnetic fields may fill the cosmic web to scales of the formation of individual stars, the magnetic field affects the observable signatures of these systems and their dynamics. Numerical simulations of MHD processes are vital to gain an understanding of the fundamental physical processes that shape these systems and the physical parameters that describe them. Such simulations can be numerically challenging however, due to the large dynamic range in densities seen in these systems. Furthermore, the divergence-free condition on the magnetic field poses additional numerical challenges for evolving the field at the discretized level.

I develop a moving mesh MHD method that overcomes these two primary computational challenges. The moving mesh framework allows the code to automatically and adaptively follow material as it moves and collapses under self-gravity. Furthermore, I formulate the numerical MHD solver as a constraint transport algorithm that maintains Maxwell's law of a divergence-free magnetic field at the level of machine-precision.

I present simulation studies of magnetic field growth and amplification on scales of cosmology and star formation. Despite their differences, these two systems share some commonalities as they are both systems collapsing under self-gravity with magneto-turbulent processes present, which are responsible for how the magnetic field ultimately grows. Fundamental physical processes in these systems and their observational signatures are investigated in this dissertation.

# Contents

1 INTRODUCTION **1**
1.1 Physical symmetries and conservation laws in numerical methods . . . . . . . 1
1.2 MHD and constrained transport . . . . . . . . . . . . . . . . . . . . . . . . . . . . 8
1.3 MHD in star formation . . . . . . . . . . . . . . . . . . . . . . . . . . . . . . . . 12
1.4 MHD in cosmology . . . . . . . . . . . . . . . . . . . . . . . . . . . . . . . . . . 13
1.5 Structure of thesis . . . . . . . . . . . . . . . . . . . . . . . . . . . . . . . . . . 14

2 CONSTRAINED TRANSPORT AND VECTOR POTENTIAL SCHEMES FOR MHD **16**
2.1 Introduction . . . . . . . . . . . . . . . . . . . . . . . . . . . . . . . . . . . . . 17
2.2 Equations, notation, and base scheme . . . . . . . . . . . . . . . . . . . . . . . 21
2.3 Constrained transport and vector potential discretizations . . . . . . . . . . . . 22
2.4 Numerical tests . . . . . . . . . . . . . . . . . . . . . . . . . . . . . . . . . . . 33
2.5 Generalization to unstructured grids . . . . . . . . . . . . . . . . . . . . . . . . 42
2.6 Conclusions . . . . . . . . . . . . . . . . . . . . . . . . . . . . . . . . . . . . . 45

3 A 2D CONSTRAINED TRANSPORT SCHEME FOR MHD ON UNSTRUCTURED MESHES **47**
3.1 Introduction . . . . . . . . . . . . . . . . . . . . . . . . . . . . . . . . . . . . . 48
3.2 Numerical method for CT on static and moving unstructured mesh . . . . . . . 53
3.3 Numerical tests . . . . . . . . . . . . . . . . . . . . . . . . . . . . . . . . . . . 72
3.4 Discussion . . . . . . . . . . . . . . . . . . . . . . . . . . . . . . . . . . . . . . 85
3.5 Concluding remarks . . . . . . . . . . . . . . . . . . . . . . . . . . . . . . . . . 89

4 A 3D VECTOR POTENTIAL CONSTRAINED TRANSPORT SCHEME FOR MHD IN AREPO **92**
4.1 Introduction . . . . . . . . . . . . . . . . . . . . . . . . . . . . . . . . . . . . . 94
4.2 Numerical method for unstructured vector potential CT . . . . . . . . . . . . . 97
4.3 Numerical tests . . . . . . . . . . . . . . . . . . . . . . . . . . . . . . . . . . . 105
4.4 Discussion . . . . . . . . . . . . . . . . . . . . . . . . . . . . . . . . . . . . . . 118
4.5 Other gauge choices . . . . . . . . . . . . . . . . . . . . . . . . . . . . . . . . . 121

5 MOVING MESH SIMULATIONS OF STAR FORMING CORES IN MAGNETO-GRAVO-TURBULENCE **124**
5.1 Introduction . . . . . . . . . . . . . . . . . . . . . . . . . . . . . . . . . . . . . 125
5.2 Simulations . . . . . . . . . . . . . . . . . . . . . . . . . . . . . . . . . . . . . . 134

5.3 Projections . . . . . . . . . . 137
5.4 Density-scaling of the magnetic field . . . . . . . . . . 140
5.5 Collapse profiles . . . . . . . . . . 141
5.6 Discussion . . . . . . . . . . 144
5.7 Conclusions . . . . . . . . . . 152
5.8 Turbulent fragmentation in simulations . . . . . . . . . . 154

6 MOVING MESH SIMULATIONS OF COSMOLOGICAL MAGNETIC FIELDS **158**
6.1 Introduction . . . . . . . . . . 159
6.2 Numerical setup . . . . . . . . . . 161
6.3 Large-scale properties . . . . . . . . . . 162
6.4 Magnetic field in halos . . . . . . . . . . 170
6.5 Discussion and concluding remarks . . . . . . . . . . 171

7 CONCLUSIONS AND FUTURE DIRECTIONS **174**
7.1 Importance of constrained transport . . . . . . . . . . 174
7.2 Comparison of fundamental magnetic and turbulent processes in star formation and cosmology . . . . . . . . . . 176
7.3 Future directions . . . . . . . . . . 178

REFERENCES **180**

TO ANYU, APU, LUCI, AND ZIZZY

# Acknowledgments

EMBARKING ON THE SCIENTIFIC JOURNEY that has led with this thesis work has been one of the most exciting and rewarding enterprises of my life. As I continue my career path in academia, I am incredibly grateful for the people in my life who have allowed me to be where I am today. For my successes in graduate school, I am most humbly indebted to my advisor, Lars Hernquist. He has always provided scientific guidance, networking opportunities with other members of the field, and chances to have been on some of the most exciting and productive conferences and research trips. As a new graduate student, Lars provided me with some of the seeds that have grown into this dissertation, but has also helped and allowed me to quickly flourish from being a new student to an independent researcher and full-fledged member of the astronomical research community. Most importantly, Lars has not just been a colleague and mentor, but also treated me as a friend. I thank Lars for his kindness and support, the great wine selection and intriguing conversations at his weekly wine and cheese meetings, and for always being available to talk about any issue or topic.

Where I am today is not just the result of a single advisor, but a number of individuals. I owe substantial gratitude to a few other mentor-like figures. I am very grateful to Volker Springel, who wrote the AREPO code I use in my work, for making it available and learning so much about numerical methods from him when I visited the Heidelberg Institute of Theoretical Studies a couple times during my time as a PhD student. I am also indebted to Rüdiger Pakmor there for providing fantastic help with the details of the AREPO code and great discussions on the physical behavior of MHD. There are a few members of Lars' group I would also like to specifically mention who have really supported me with scientific discussion and hands-on advising on some of the projects I worked on. A special thank you to Mark Vogelsberger, Debora Sijacki, and Federico Marinacci for their interaction, support, and discussions.

I would like to thank my thesis advising committee Alyssa Goodman, Doug Finkbeiner, Ramesh Narayan who have been with me along this journey and have read this thesis. In addition to being on my committee, I have had the pleasure of having Alyssa as a co-author on my work related to star formation and found her group meetings invaluable. I thank Doug for his support over the years and for being a professor whom whom I could talk about any topic. I also thank Ramesh for taking time to discuss some of my research projects in full detail, and for his wonderful teaching and insightful questions at ITC lunches (sometimes they really increased the take-away I obtained from the talk that day). I am also grateful for my external reviewer, Eve Ostriker from Princeton, where I will be next year as a postdoctoral fellow, for taking time to read my dissertation and traveling to Harvard for my defense.

In addition, I would like to mention a couple of other professors at Harvard for their support and conversations: Avi Loeb and Karin Öberg. I am forever grateful.

I owe a great deal to all my other co-authors. It is a pleasure to collaborate with them. I especially thank Blakesley Burkhart and Chat Hull for the many hours we would sit down together and do science. They are not only fantastic scientists but true friends. I also owe a huge amount to Chris McKee at Berkeley for our long email conversation threads and for asking some very profound and insightful questions to helped steer parts of the project.

I am deeply appreciative of the many great faculty I have met outside my institution. I enormously enjoyed discussing the numerical aspects of MHD with Jim Stone, Gabor Tóth, Dinshaw Balsara, and Ethan Vishniac. I also thank Jim for being my host at my upcoming postdoctoral position at Princeton. A huge thank you to Eliot Quataert from Berkeley and Phil Hopkins from Caltech as well, who I really appreciated getting to know and hope to collaborate with in the future. Thank you for the discussions and interest in my work. I also am very grateful with my interactions with Dong Lai, Mikhail Medvedev, Jorge Moreno, David Spergel, and Hy Trac.

I am also thrilled to have had the chance to work on a number of diverse research projects outside my PhD over these last few years. I would especially like to thank Sauro Succi, with whom I developed a smoothed-particle hydrodynamic solver for the non-linear Schrödinger equations (superfluids) and a memory-efficient integer lattice technique to solve the 6D Vlassov-Poisson equations. I also thank Scott Tremaine for invaluable discussions on the latter project. I also loved having the chance to lead a research project in simulating turbulence in scalar field dark matter, and working with Victor Robles, Jerry Ostriker, Jesus Zavala, Mike Boylan-Kolchin, and Anastasia Fialkov in this subfield.

I wish to express a sincere thank you to everyone in Lars' research group for their feedback and fellowship. The postdocs associated with the group (at the time of my PhD) – Simeon

Bird, Ana Bonaca, Benedikt Diemer, John Forbes, Shy Genel, Rahul Kannan, Jill Naiman, Annalisa Pillepich, Laura Sales, and Kate Rubin – served as excellent role models for me and the other the graduate students. I would also like to thank Lars' other PhD students (and students associated with the group) who I had the pleasure to intersect paths with: Fernando Becerra, Gurtina Besla, Laura Blecha, Eddie Chua, Ben Cook, Chris Hayward, Matt Heising, Harshil Kamdar, Luke Zoltan Kelley, Diego Muñoz, Dylan Nelson, Roxana Pop, Vicente Rodriguez-Gomez, Josh Suresh, Paul Torrey, and Sarah Wellons.

I also would like the thank all the graduate students who's friendship and camaraderie helped make the PhD experience fun even in the most grueling times. I especially value the shared experiences, late night conversations, and adventures with the students in my incoming class: Kate Alexander, Fernando Becerra, Pierre Christian, Marion Dierickx, Xinyi Guo, George Miller, Stephen Portillo, Zachary Slepian, Yuan-Sen Ting, and Mary Zhang. I also thank my office mate Zack for many distracting conversations, snack breaks, and enriching the day-to-day office experience. I thank Pierre, Stephen, and Zack for the time spent as housemates.

I thank the department administrative staff Peg Herlihy, Robb Scholten, Uma Mirani, and Nina Zonnevylle for their tireless efforts and minimizing the amount of time I need to spend on bureaucratic details. I also welcomed their friendship and smiles, and do not know how the Harvard Smithsonian Center for Astrophysics would continue to operate without the work they do.

As a graduate student, I had the pleasure of serving on the library committee as the student representative, and greatly enjoyed discussing the future visions for the library with Daina Bouquin and Chris Erdmann.

I would not have been in graduate school without all the wonderful undergraduate research experiences I was fortunate to have. I thank Julia Lee, with whom I had my first exposure and introduction into astronomical research. I owe substantial gratitude to Andy Fabian at Cambridge and Katherine Blundell at Oxford for the two wonderful summers I spent doing research there. I am also ever indebted to Karl Glazebrook and Andy Green at Swinburne for the time I spent doing summer research there as an undergraduate.

I am obligated to acknowledge the fellowships that have supported my graduate school experience. I am greatly humbled to have completed my thesis research with the support of a National Science Foundation Graduate Research Fellowship and a NASA Earth and Space Science Fellowship.

I would not be where I am today without the support from my teachers at Mililani High School, Hawaii. A big mahalo especially to Mrs. Abe, Mrs. Higa, Mrs. Sitachitta, and Mrs. Webb for shaping my early interests and outlook on math and science.

Finally, I would like to thank my friends and family who have shaped my dreams and who I am. Especially my closest college friends Aaron Szasz and Charles Herrmann, thanks for the support and the many Google hangouts as we each pursue PhDs across the country. And of course I am most grateful for my mother Eva and father Gabor, and my sisters Lucia and Viola for being with me through life's journey. Thank you.

# 1

# Introduction

## 1.1 PHYSICAL SYMMETRIES AND CONSERVATION LAWS IN NUMERICAL METHODS

Symmetries and invariants lie at the heart of modern physics. Indeed, Noether's theorem states that given the action of a physical system, every differentiable symmetry has a corresponding conservation law. The well-known examples from classical mechanics are invariance in translation in time, which yields conservation of energy, invariance in translation in space, which yields conservation of linear momentum, and invariance in rotation in space, which yields conservation of angular momentum. Symmetries and invariants have important qualitative, not just quantitative implications about the dynamics of systems. If the symmetries were slightly broken, it can change the nature of stability and lead to non-physical effects such as decaying orbits.

Physical equations, such as the inviscid fluid equations (Euler equations) or the magneto-hydrodynamic (MHD) equations (which are the Euler equations coupled to magnetic fields, describing an ionized plasma), have nonlinear terms that usually make finding analytic solutions intractable. Therefore one must often resort to numerical simulations to obtain the time evolution of the solution to these partial differential equations. As computers can only represent discrete bits of information, this means that the physical equations describing a continuous solution need to be discretized onto a finite set of grid points, elements, or cells. Furthermore, spatial and time derivatives in the equation need to be estimated up to some order of accuracy. This is known as discretizing a set of equations, a framework used to obtain numerical solutions. The numerical solution is usually characterized by a resolution $N$, and the total error in the solution is often expected (i.e., can be proven) to decrease as some inverse power of $N$.

A common all-purpose method to solve partial differential equations is the Runge-Kutta method, which effectively uses Taylor expansion on the discretized grid to obtain the numerical solution. However, the method is agnostic about physical symmetries of the system and does not necessarily preserve conserved quantities to a machine-precision level of accuracy (machine-precision is the best a computer can do, due to finite precision arithmetic round-off errors). In the limit of infinite resolution, the exact solution is expected to be recovered. But at a fixed resolution, the conserved quantities may decay or grow with time due to truncation errors. Figure 1.1 demonstrates this problem for a simple physical system: two-body orbital dynamics. It compares a 4th-order Runge-Kutta with a lower (2nd) order leapfrog scheme. The leapfrog scheme is a time-symmetric, symplectic discretization which preserves its Hamiltonian to machine-precision (conserving total energy, linear momentum, and angular momentum). Despite being lower order, the leapfrog scheme has qualitatively better behavior in the presence of truncation errors at a fixed finite resolution. Orbits in Runge-Kutta schemes decay with time, due to lack of respecting the energy conservation condition (and angular momentum). The numerical effect of the leapfrog scheme due to truncation errors is less severe: the orbit instead precesses but the two bodies will never collide with each other.

The take-away from the above example is that it is important to preserve physical symmetries and invariants at the discretized level. The physical system can be thought of as a mathematical system, often a continuous one. But then, when the system is discretized for the purposes of numerical simulations, one can ask whether the discretized system can be thought of as it's own mathematical system. That is, does the discretized system have it's own set of conservation laws and symmetries, perhaps a Hamiltonian, that are guaranteed to be preserved to machine-precision as the system evolves with time? This concept of thinking about the discretized system as its own mathematical and physical system is illustrated in Figure 1.2. The discrete system should have qualitatively similar behavior to the continuous one and should

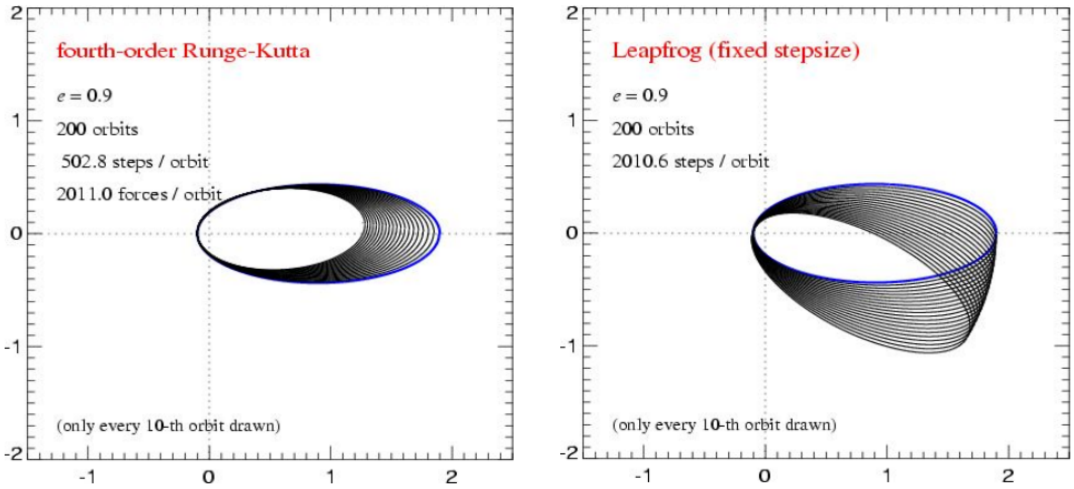

4th order Runge Kutta    2nd order leapfrog

**Figure 1.1:** Comparison of a 4th-order Runge-Kutta method with a 2nd-order leapfrog (symplectic) method for orbits. Even though the Runge-Kutta method is higher order, it does not preserve the total energy of the system to machine-precision and the effect of truncation error is that the orbit decays with time. On the other hand, the 2nd order leapfrog scheme is symplectic and conserves total energy so the worst that an orbit can do is precess due to truncation error, which is qualitatively better behavior in an $N$-body gravitational code. Resolution for these simulations is chosen to exaggerate the numerical effects. Image credit: Springel (2005).

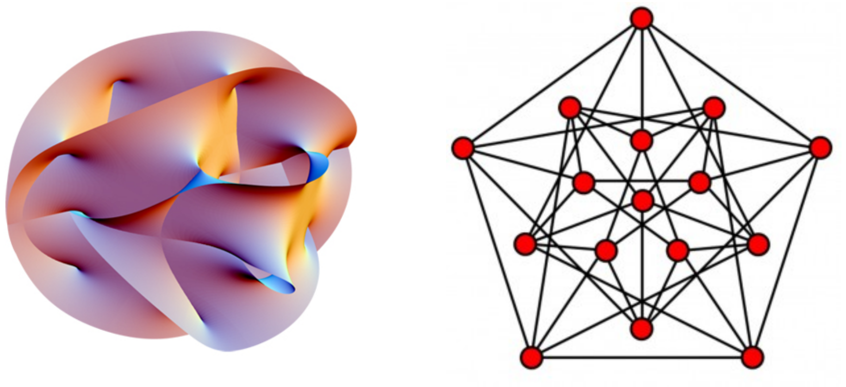

Physical System **(Continuous)**
– symmetries
– invariants
– conserved quantities

Computer Representation **(Discrete)**
– *discrete* symmetries?
– *discrete* invariants?
– *discrete* conserved quantities?

**Figure 1.2:** Continuous and discretized physical systems as their own systems. Image credit: Susskind (2003); National Museum of Mathematics (2017).

be expected to recover the continuous solution in the limit of infinite resolution. In a sense, scientific computing can be though of as a branch of mathematics where one seeks to describe analogous behaviors between continuous and discrete systems.

On the other hand, I also like to think about scientific computing as an art. There is an incredible amount of freedom for creating a discretization on a computer. In a sense it is similar to the brush stroke an artist chooses to approximate reality. This concept is illustrated in Figure 1.3. Common ways to discretize partial differential equations include finite difference, finite volume, finite element, and spectral methods. With finite difference methods, the values of functions are located on a finite set of regularly spaced grid points. Derivatives are estimated using extended stencils. In a sense, this representation is a little like the pointilist art style found in paintings such as “A Sunday Afternoon on the Island of La Grande Jatte” by Georges Seurat. Finite volume methods are often used for solving fluid equations such as the Euler equations because they take a slightly different approach. Here, the domain is split into cells and the volume averages of physical densities are evolved. Cells exchange material via fluxes (material flows from a cell to it’s neighbor), making the method conservative. The domain decomposition of such a method is a bit reminiscient of the color block paintings by Piet Mondrian. Finite element methods are an extension/generalization of the finite volume idea, where the solution is instead represented as a sum of local basis functions with compact support that span a few elements. The method is useful for irregular grids and obtaining higher order of accuracy. The representation is a little bit analogous to the patchy nature of “The Starry Night” by Vincent van Gogh. Finally spectral methods solve the equations in Fourier space, which can have advantages, such as turning derivatives into multiplications by the wave number, and may achieve exponential spatial convergence for smooth problems. Since it is hard to visualize physical space represented in Fourier space, the artwork chosen for our ongoing playful analogy is the chaotic drip painting “Cool White” by Lee Krasner.

In the spirit of maintaining physical symmetries and invariants at the discretized level, the recently developed moving mesh AREPO code (Springel 2010) is an interesting one to consider here. It is a finite volume solver for the Euler equations, meaning that it conserves total mass, linear momentum, and energy of the inviscid fluid. Additionally, the mesh cells move continuously with the fluid flow (using a mesh construction known as a Voronoi diagram at each timestep). Following gas parcels makes the code have a Lagrangian nature, as opposed

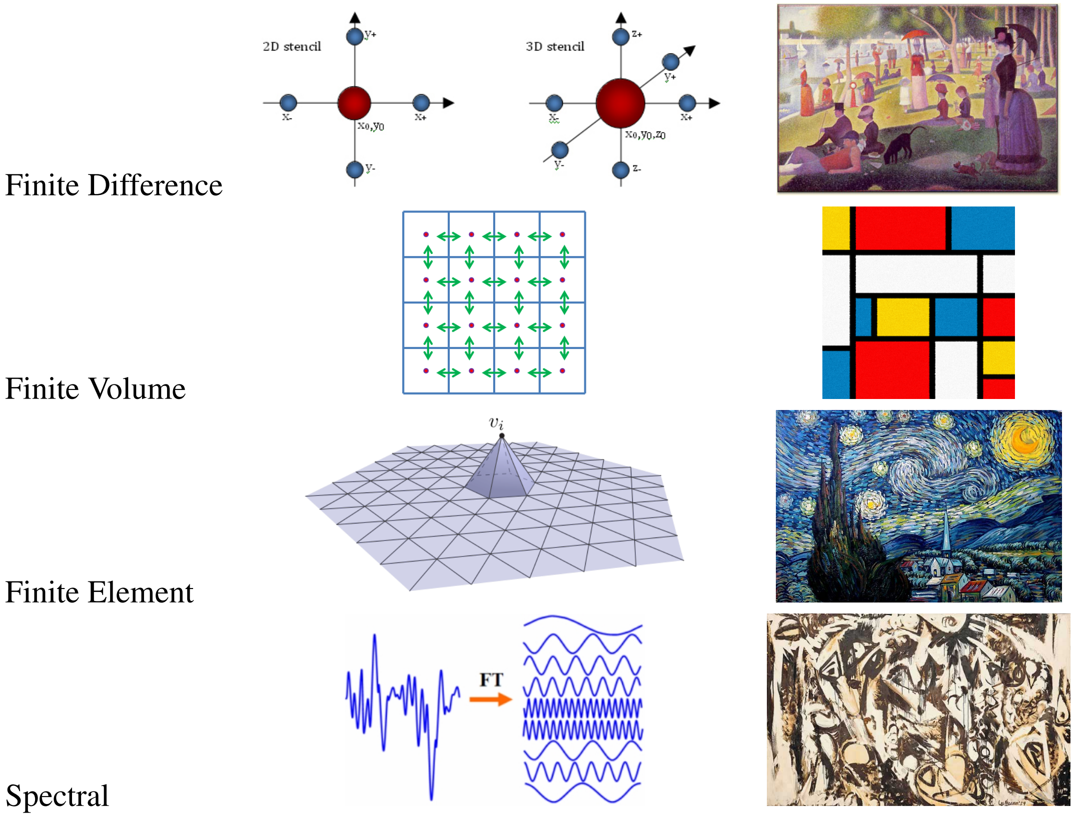

**Figure 1.3:** Analogy between different discretizations in scientific computing and styles of artwork. The art pieces are “A Sunday Afternoon on the Island of La Grande Jatte” by Georges Seurat, example of De Stijl art by Piet Mondrian, , and “Cool White” by Lee Krasner. Image credits: left column Gourlay (2017); Mocz (2017b); Solomon & Butscher (2017); Thummalapalli (2017), right column Douma (2017); Groe (2017); Goudis (2017); WikiArt (2017)

to the Eulerian nature of fixed grid finite volume codes. A consequence of this property is that the code is Galilean-invariant at the discretized level, meaning that truncation errors are unchanged by constant boosts in the velocity field. This is a useful property to have, as fluid instabilities can be artificially suppressed by truncation and round-off errors from large velocity boosts. The moving mesh codes combines the main advantages of the major types of fluid solvers commonly used in astrophysics: Eulerian grid based finite volume codes and Lagrangian smoothed-particle hydrodynamics codes (Figure 1.4). Finite volume codes are very useful because in addition to conserving total mass, energy, and linear momentum, they can capture shocks (discontinuities) in the fluid very accurately because they work with an integral form of the governing differential equations. In contrast smoothed-particle hydrodynamics have the advantage of being Lagrangian (conserving total mass, energy, linear momentum, and angular momentum) but fluid quantities are reconstructed using smooth kernels meaning that the solution is less accurate at shocks. The moving mesh code is a Lagrangian code that does capture shock structure accurately, a common feature in most astrophysical systems.

## 1.2 MHD AND CONSTRAINED TRANSPORT

Ionized plasmas are found on all scales of the universe, from clusters of galaxies to star forming regions, to accretion discs around black holes, and more. Often the relevant physics is captured by the ideal MHD equations. These are the Euler equations for a fluid coupled with Maxwell's equations, used to describe a magnetized plasma. The ideal MHD equations ne-

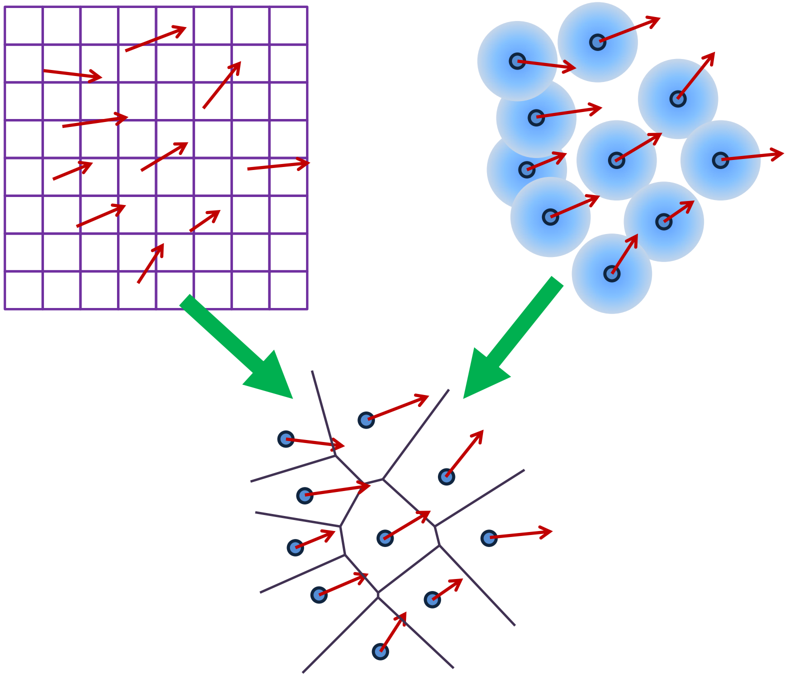

**Figure 1.4:** The moving mesh framework *(bottom)* captures the best of both worlds of fixed-grid, shock-capturing finite volume codes *(left)* and Lagrangian smoothed particle hydrodynamics codes *(right)*.

glect resistivity, which is often tiny in astrophysical applications. The solution to the ideal MHD equations obey Maxwell's law for magnetism (no monopoles):

$$\nabla \cdot \mathbf{B} = 0 \tag{1.1}$$

This condition has important topological consequences. The equation means that the magnetic field is "frozen" into the fluid. Flux freezing means that the magnetic flux through a surface that moves with the fluid flow remains constant. The divergence free condition also means that the helicity (linking of field lines) is preserved: e.g., initially unlinked filed lines cannot form knots. Importantly, this equation is *not* needed to evolve the equations. It is just a physical property that is preserved as all times if the condition is true in the initial condition.

It turns out that maintaining this local invariant property of magnetic fields at the discretized level is important for both numerical stability and accuracy. One does not simply evolve the magnetic field with a finite volume approach, like the rest of the fluid variables. Such an approach almost always leads to the solution blowing up for complex problems because small errors in the divergence-free condition can grow exponentially large (Tóth 2000; Mocz 2017a). Cleaning and divergence-correcting approaches are sometimes coupled with the finite volume approach to help alleviate the problem, such as the Powell scheme Powell et al. (1999), which effectively spreads around divergence errors and has them cancel out each other to some extent. The gold standard approach, however, for fixed grids, is the constrained transport (CT) algorithm (Yee 1966; Evans & Hawley 1988). The method picks a very natural

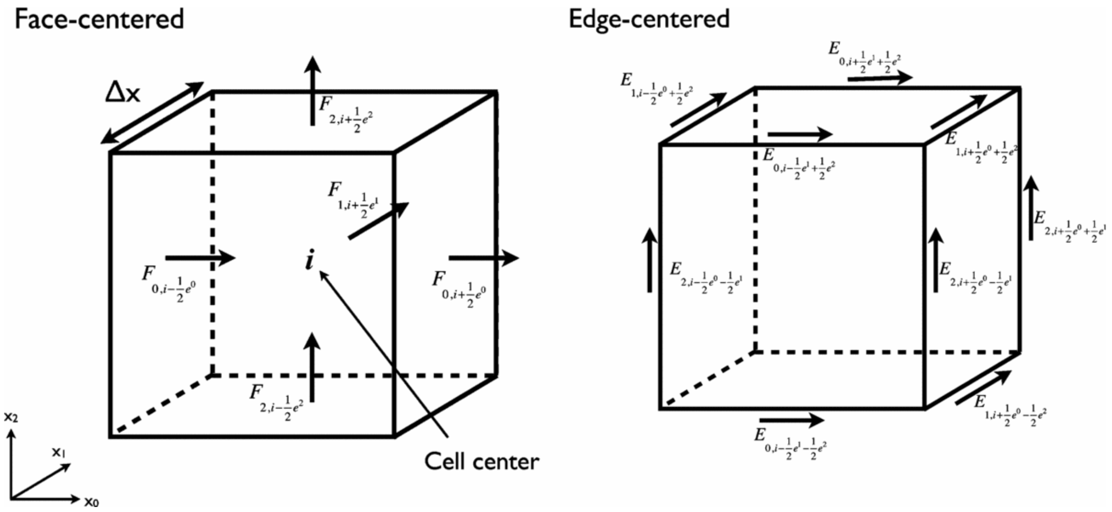

**Figure 1.5:** Constrained Transport. Rather than using a volume-centered approach of finite volume methods, the magnetic fields are face-centered, and the electromotive force is edge-centered. Image credit: Miniati & Martin (2011)

representation of the magnetic field. Rather than evolving volume-averaged values as finite approaches do, the CT method evolves face-averaged magnetic fields (Figure 1.5). The fields are then updated according to the electromotive force on 'circuits' along the edges of cells. By construction the net change in magnetic flux enclosed in a grid cell does not change from one timestep to the next (see Chapter 2 for details). The CT algorithm is a great example of the scientific computing artist picking a brush stroke that leads to physical symmetries being captured at the discretized level. Generalizing and extending the CT method to arbitrary static and moving meshes turns out to be a challenging task and is one of the goals of this thesis.

## 1.3 MHD IN STAR FORMATION

A proper introduction to the topic of magnetic fields in star formation is given in the beginning of Chapter 5, but we briefly discuss a few main ideas here. A modern understanding of star formation is rooted to the observation of the so-called Larson's laws (Larson 1981) which revealed that the velocity dispersion in star forming clouds is self-similar with region size, indicative of a turbulent cascade. Additionally, magnetic fields are known to be present in molecular clouds, recently well-characterized by Zeeman splitting observations (Crutcher et al. 2010). Turbulence and magnetic pressure, along with gas thermal pressure, are forces that act against the collapse of a gas cloud under its self-gravity. These physical processes regulate star formation. The understanding of which physical processes play the key role is still debated both observationally and theoretically. But in general, the collapse process fits into the framework of a magneto-gravo-turbulence model, and possibly non-ideal MHD terms and radiation are important too, at least on some length scales and during some stages of star formation. The magnetic field morphology of young stellar cores is seen to be diverse, observationally. Figure 1.6 shows the projected density and magnetic field in two young Class 0 protostars. One of the objects, NGC 1333 IRAS 4A, shows a classical hourglass shape, indicative of a dynamically important magnetic field that is primarily responsible for supporting the collapse against self-gravity. However, in the recent ALMA observations of Ser-emb 8, polarization measurements reveal a chaotic field morphology, perhaps indicative of the dominant role of turbulence. How the magnetic field amplifies as clouds collapse and the

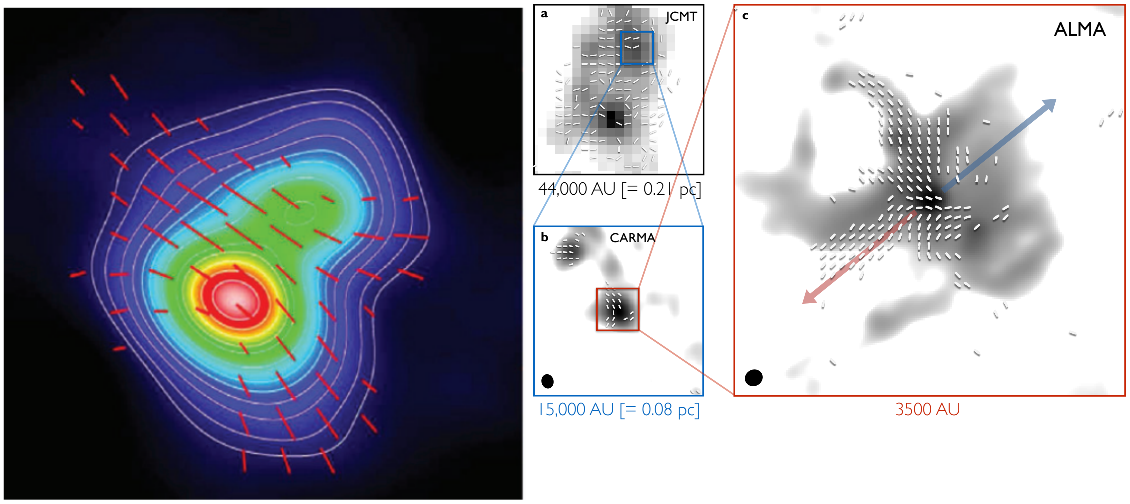

**Figure 1.6:** Comparison of the magnetic fields of two young (Class 0) protostars. NGC 1333 IRAS 4A *(left)* shows classic hourglass magnetic field morphology. Ser-emb 8 *(right)* shows a turbulent, chaotic field morphology. Image credit: Girart et al. (2006); Hull et al. (2017)

initial conditions from which they started are important questions to answer. They hold a key to understanding the ultimate fate of protostars and gain a theoretical understanding of the star formation process.

## 1.4 MHD IN COSMOLOGY

A proper introduction to the topic of cosmological primordial magnetic fields is given in the beginning of Chapter 6, but a few brief ideas are mentioned here. Magnetic fields may fill much of the cosmic web if they were created during inflation or generated in the Universe during cosmic accretion shocks or at ionization fronts during reionization. Active galactic nuclei (AGN) feedback may also be able to fill Mpc regions of the intergalactic medium with magnetized plasma. The nature of primordial magnetic fields is poorly understood, due to a lack of direct observation of magnetic fields outside of halos. This makes simulation work very important to help explore the possible parameter space of magnetic field strengths and topologies to aid in designing observational strategies to detect primordial magnetic fields and constrain the possible parameter space. Magnetic fields are measured on the cluster scale from Faraday rotation measurements, but whether they originate from the galaxy or from large scales is unknown. Magnetic fields are also possibly dynamically important and may alter structure formation of galaxy structure to a small extent. As such, we investigate simulating a cosmological volume with various initial conditions in Chapter 6, and learn about the amplification process of magnetic fields, and make theoretical predictions for observable properties. There are some important similarities and differences between cosmological magnetic field amplification and the case of star formation, discussed in Chapter 7.

## 1.5 STRUCTURE OF THESIS

The dissertation is structured as follows. In Chapter 1 we have given a basic introduction to the broad topics of this thesis. In Chapter 2 we discuss a new generalization of constrained transport methods for solving the MHD equation in terms of vector potentials on a static grid. In Chapter 3 we generalize and implement the classic constrained transport method on 2D moving meshes. The implementation for 3D moving meshes is greatly simplified using the ideas from Chapter 2 and therefore Chapter 4 presents the 3D implementation in the AREPO code using a vector potential formulation, and presents some astrophysically relevant simulations (cosmological volumes, turbulent boxes, and galactic disks). Chapter 5 applies the MHD module of AREPO to study the physics of star formation in a turbulent, magnetic medium, and identifies and characterizes two regimes in which it may occur. Chapter 6 looks at the effects of MHD on cosmological volumes, studying the impact of primordial magnetic fields on structure formation and how the magnetic field grows inside halos. Conclusions along with future directions are provided in Chapter 7, along with a comparison of the physics in the star formation and cosmological simulations.

*Thoroughly conscious ignorance is the prelude to*
*every real advance in science.*

James Clerk Maxwell

# 2

# Constrained transport and vector potential schemes for MHD

– based on –

Mocz, P. (2017). Correspondence between constrained transport and vector potential methods for magnetohydrodynamics. *Journal of Computational Physics*, 328, 221–233.

We show that one can formulate second-order field- and flux-interpolated constrained transport/central difference (CT/CD) type methods as cell-centered magnetic vector potential schemes. We introduce four vector potential CTA/CDA schemes – three of which correspond to CT/CD methods of Tóth (2000) and one of which is a new simple flux-CT-like scheme – where the centroidal vector potential is the primal update variable. These algorithms conserve a discretization of the $\nabla \cdot \mathbf{B} = 0$ condition to machine precision and may be combined with shock-capturing Godunov type base schemes for magnetohydrodynamics. Recasting CT in terms of a centroidal vector potential allows for some simple generalizations of divergence-preserving methods to unstructured meshes, and potentially new directions to generalize CT schemes to higher-order.

## 2.1 INTRODUCTION

It is well known that maintaining Maxwell's $\nabla \cdot \mathbf{B} = 0$ equation is important for numerically solving the magnetohydrodynamics (MHD) equations (Brackbill & Barnes 1980; Brackbill 1985; Evans & Hawley 1988; Tóth 2000). Keeping the magnetic field divergence-free is necessary for stability and accuracy. Simple finite volume numerical methods for MHD do not accomplish this, and as a result can be unstable or show numerical artifacts. The gold-standard solution to this problem is to use a staggered-mesh representation: the constrained transport (CT) approach (Evans & Hawley 1988), originally developed in the context of electrodynamics (Yee 1966). This method has machine-precision control on the divergence of $\mathbf{B}$. Most modern MHD codes employ the CT approach (Fromang et al. 2006; Mignone et al. 2007; Cunningham et al. 2009; Christlieb et al. 2014; White et al. 2016).

Alternatively, one may evolve instead the magnetic vector potential $\mathbf{A}$, and take curl $\mathbf{B} = \nabla \times \mathbf{A}$ to obtain a divergence-free magnetic field by construction. However, it has often been stated in the literature that the disadvantage of this approach is that the order of spatial derivatives increases by one, which reduces the order of accuracy by one (Evans & Hawley 1988; Tóth 2000). In this paper, we show that such a statement is not necessarily true: there exist cell-centered magnetic vector potential reformulations of CT approaches, which keep the order of accuracy by nature of being equivalent to the original formulations.

It is already known that in the framework of the CT approach, instead of updating *face*-averaged magnetic fields on the staggered mesh, one may equivalently update an underlying magnetic vector potential on the *edges* of cells (Evans & Hawley 1988; Tóth 2000). This approach has been employed successfully in some existing codes (Del Zanna et al. 2003; Etienne et al. 2015). However, in this work we show that *cell-centered* formulations of CT are also possible and are beneficial because they can be simpler to implement and generalize to unstructured grids (especially moving or adaptive grids), and also improve memory requirements and memory access. Face-centered formulations of CT for unstructured grids are, of course, possible, and have been recently developed (Mocz et al. 2014a; Balsara & Dumbser 2015a,b).

In this paper, we present four centroidal vector potential constrained transport methods. We call these methods flux-CTA, field-CTA, flux-CDA, field-CDA. These methods are akin to the flux- and field-interpolated CT and central difference (CD) schemes summarized and compared in Tóth (2000). In fact, we show the field-CTA, flux-CDA, field-CDA formulations are equivalent to field-CT (Dai & Woodward 1998a,b), flux-CD (Tóth 2000), field-CD (Tóth 2000) respectively, and flux-CTA closely resembles flux-CT (Balsara & Spicer 1999) but uses a more extended stencil. We restrict our focus to 2D Cartesian grids, but in general the methods may be extended to unstructured grids, and we have recently done so for the field-CDA method in Mocz et al. (2016).

Our centroidal vector potential schemes are different from the centroidal vector potential schemes of Helzel et al. (2011, 2012), where the authors evolve the induction equation for $\mathbf{A}$ assuming that the velocity flow is fixed by the base-scheme, and the method assumes $\mathbf{A}$ is differentiable. In our approach, the induction equation for $\mathbf{A}$ is evolved by the electric field obtained from the base scheme, which is responsible for making it equivalent to CT schemes.

We note that many flavors of CT algorithms exist, including modifications to the flux-CT schemes that reduce exactly to the equivalent one-dimensional solver for plane-parallel, grid-aligned flow (Ryu et al. 1998b; Gardiner & Stone 2005, 2008). Thus other, more sophisticated centroidal vector potential scheme formulations are possible to design. Here, we restrict ourselves to constructing vector potential schemes similar to the second-order schemes of Tóth (2000). But in general it may be possible to incorporate many of the recent advances in face-centered CT into centroidal vector potential schemes.

A number of important advancements have been made to the CT algorithm in the recent years. First, face-centered formulations of CT have been extended to and tested on arbitrary unstructured meshes in Mocz et al. (2014a); Balsara & Dumbser (2015a,b), including moving

Voronoi meshes (Mocz et al. 2014a). Second, genuinely multi-dimensional Riemann solvers have been developed for two-and three-dimensional problems (Balsara 2012, 2014, 2015), and can be designed for use on unstructured meshes as well (Balsara et al. 2014; Balsara & Dumbser 2015b). These Riemann solvers accept input from all the neighboring states that come together at a face and output multi-dimensionally upwinded fluxes in all directions. Having the multi-dimensionally upwinded property has been shown to be important for stability in extreme applications. Third, globally divergence-free reconstruction techniques have been developed in Balsara (2004, 2009); Balsara et al. (2016). Such techniques are important for divergence-free reconstruction of adaptively refined meshes, as well as achieving higher-order divergence-free reconstruction. Fourth, CT implementations, incorporating many of the mentioned advancement techniques, have been extended to higher-order (i.e., beyond second-order) (Balsara & Dumbser 2015b; Balsara 2009; Balsara et al. 2016). We note that some of the basic CT schemes presented in Tóth (2000), on which we base our methods, are not directly extendable beyond second-order, but may be combined with multi-dimensional Riemann solvers and unstructured meshes. The scope of the present work investigates cell-centered vector potential versions of CT in the simplest second-order formulations, and extensions to higher-order and use of multi-dimensional Riemann solvers are left for future work.

The paper is organized as follows. In Section 2.2 we lay out basic notation. Section 2.3 describes the four CT schemes expressed in terms of centroidal vector potentials. Numerical testing of the methods are shown in Section 2.4. Concluding remarks are offered in Section 2.6.

The manuscript follows the notation of Tóth (2000) in order to facilitate the connection between the CTA/CDA and CD/CT schemes.

## 2.2 EQUATIONS, NOTATION, AND BASE SCHEME

The ideal MHD equations can be expressed in conservative form as:

$$\frac{\partial \mathbf{U}}{\partial t} + \nabla \cdot \mathbf{F} = 0 \tag{2.1}$$

where $\mathbf{U}$ is the vector of the conserved variables and $\mathbf{F}(\mathbf{U})$ is the flux:

$$\mathbf{U} = \begin{pmatrix} \rho \\ \rho\mathbf{v} \\ \rho e \\ \mathbf{B} \end{pmatrix}, \quad \mathbf{F}(\mathbf{U}) = \begin{pmatrix} \rho\mathbf{v} \\ \rho\mathbf{v}\mathbf{v}^T + p - \mathbf{B}\mathbf{B}^T \\ \rho e\mathbf{v} + p\mathbf{v} - \mathbf{B}(\mathbf{v}\cdot\mathbf{B}) \\ \mathbf{B}\mathbf{v}^T - \mathbf{v}\mathbf{B}^T \end{pmatrix} \tag{2.2}$$

and $p = p_{\text{gas}} + \frac{1}{2}\mathbf{B}^2$ is the total gas pressure, $e = u + \frac{1}{2}\mathbf{v}^2 + \frac{1}{2\rho}\mathbf{B}^2$ is the total energy per unit mass, and $u$ is the thermal energy per unit mass. The system is closed with the equation of state of the fluid given by the ideal gas law $p = (\gamma - 1)\rho u$.

We will denote the discretized time levels by superscripts and spatial discretization by subscripts. In 2D, the cell centers are indexed by integer subscripts $i, j$. Face-averaged values are indexed by half-integers, e.g., $i, j + 1/2$.

The *base scheme* we use for the MHD equations is a second-order finite-volume Godunov's method in the form of the MUSCL-Hancock scheme (Toro 2013; Van Leer 2006). The base scheme advances the solution $U^n$ at time level $n$ to the auxiliary solution at time level $n+1$, denoted by $U^*$. This auxiliary solution is used in some cases to obtain the final solution $U^{n+1}$. Our base scheme uses the robust and accurate 5-wave HLLD approximate Riemann solver (Miyoshi & Kusano 2005) and the *minmod* total variation diminishing slope limiter to handle discontinuous solutions.

## 2.3 CONSTRAINED TRANSPORT AND VECTOR POTENTIAL DISCRETIZATIONS

We describe the CT algorithms in 2D, for simplicity. The ideas can be readily carried over to 3D.

The original CT scheme of Evans & Hawley (1988) uses a staggered grid representation of the magnetic field to maintain the divergence-free condition. The magnetic field is represented by primal variables $\mathbf{b}$ on the faces of cells. These are updated in time, and can be used to obtain cell averaged magnetic fields $\mathbf{B}$ (auxiliary variables) at the end of each timestep. In 2D, the $b^x$ components of the magnetic field are located at $x_{i+1/2}, y_j$. and the $b^y$ components are located at $x_i, y_{j+1/2}$. Electric fields $\Omega \equiv E_z \equiv -\mathbf{v} \times \mathbf{B}$ are calculated at the corners $x_{i+1/2}, y_{j+1/2}$ (estimated at the middle of the timestep, for second-order accuracy) and used to update the face-averaged magnetic fields. Figure 2.1 shows a representation of the CT discretization.

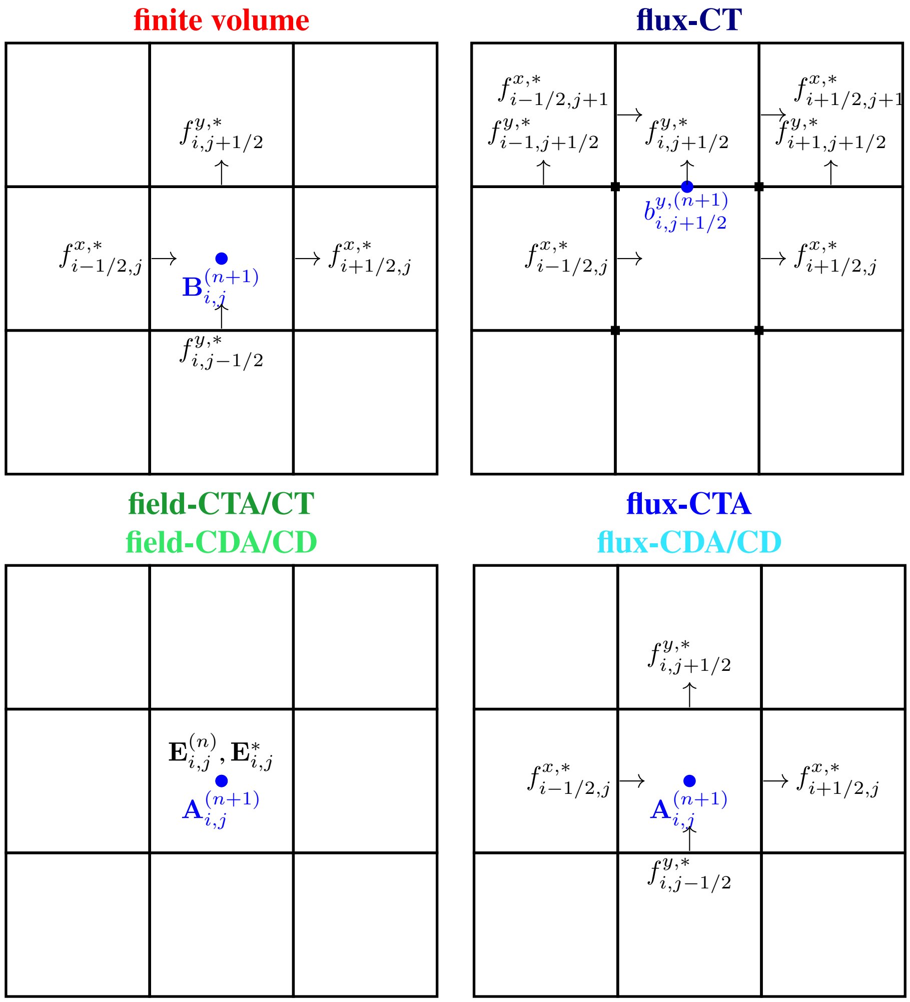

**Figure 2.1:** Representation of the update of the primal variable in each of the schemes. In the finite volume approach (the base scheme), the cell-centered $B$ field is updated via the numerical fluxes from the Riemann solver. In the flux-CT scheme, the face-averaged magnetic fields are updated via recovering the electric field at the face edges from the surrounding numerical fluxes. In field-CTA/CDA approaches, the cell-centered magnetic vector potential is updated from the time-averaged electric field obtained with the base scheme. In the flux-CTA/CDA approaches, the cell-centered magnetic vector potential is updated from the electric field obtained from the numerical fluxes across surrounding faces

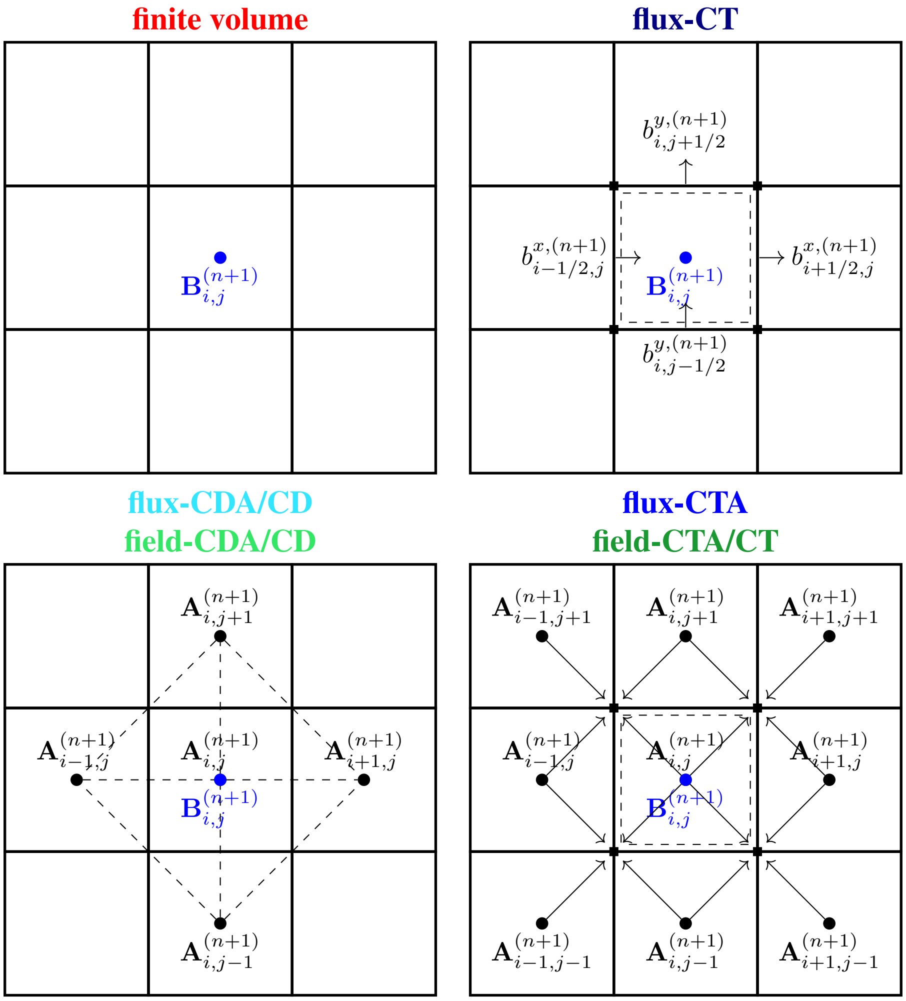

**Figure 2.2:** Representation of the recovery of the cell-centered $B$-field in each of the schemes. Dashed lines show surfaces on which the sum of magnetic fluxes is $0$ (i.e., $\nabla \cdot \mathbf{B} = 0$ constraint satisfied to machine-precision). In the finite volume approach (the base scheme), the cell-centered $B$-field is the primal variable, and no divergence-free condition is enforced. In the flux-CT approach, the cell-centered $B$-field is recovered by averaging the neighboring face-averaged $B$-fields. Equivalently one could use the vector potentials at the face edges (marked with square node markers) rather than face magnetic fields as the primal variable to update and recover the face-averaged $B$-fields. In the CDA schemes, the volume-averaged $B$-field is recovered from the immediate surrounding vector potentials (in fact, $B$-fields can be recovered for each of the triangles outlined with dashed lines, with continuous $B$-fields across the faces). In the CTA schemes, the volume-averaged $B$-field is recovered by extrapolating the cell-centered vector potentials to the edges and thus obtaining face-averaged $B$-fields, from which the volume-averaged $B$-fields are recovered as in the CT scheme.

The general CT scheme is given by:

$$\begin{aligned} b^{x,n+1}_{i+1/2,j} &= b^{x,n}_{i+1/2,j} - \Delta t \frac{\Omega_{i+1/2,j+1/2} - \Omega_{i+1/2,j-1/2}}{\Delta y} \\ b^{y,n+1}_{i,j+1/2} &= b^{y,n}_{i,j+1/2} + \Delta t \frac{\Omega_{i+1/2,j+1/2} - \Omega_{i-1/2,j+1/2}}{\Delta x} \end{aligned} \tag{2.3}$$

and preserves the divergence-free condition as long as it is satisfied in the initial conditions, due to exact cancellation of the electric field update terms. Namely, the following discretization of $\nabla \cdot \mathbf{B}$ is preserved:

$$(\nabla \cdot \mathbf{b})_{i,j} = \frac{b^x_{i+1/2,j} - b^x_{i-1/2,j}}{\Delta x} + \frac{b^y_{i,j+1/2} - b^y_{i,j-1/2}}{\Delta y} \tag{2.4}$$

There are various flavors of CT schemes, which differ in how one obtains the electric fields at the cell corners. These may be obtained either through *field*-interpolation of the electric fields at cell centers, or interpolation of the electric fields deduced from the Riemann solver fluxes of the base scheme at the cell interfaces (i.e., *flux*-interpolation).

The cell-averaged magnetic field is obtained from the face-averaged values by simple averaging:

$$\begin{aligned} B^x_{i,j} &= \frac{b^x_{i+1/2,j} + b^x_{i-1/2,j}}{2} \\ B^y_{i,j} &= \frac{b^y_{i,j+1/2} + b^y_{i,j-1/2}}{2} \end{aligned} \tag{2.5}$$

It is well known (Evans & Hawley 1988) that one can equivalently reformulate CT schemes by keeping track of the magnetic vector potential at cell corners as the primal update variables instead of the face-averaged magnetic fields. Simply update the magnetic vector potential $A^z_{i+1/2,j+1/2}$ via its induction equation

$$A^{z,n+1}_{i+1/2,j+1/2} = A^{z,n}_{i+1/2,j+1/2} - \Delta t \Omega_{i+1/2,j+1/2} \tag{2.6}$$

and recover the face averaged magnetic fields via the discretization of the curl-operator ($\mathbf{B} = \nabla \times \mathbf{A}$):

$$\begin{aligned} b^{x,n}_{i+1/2,j} &= \frac{A^{z,n}_{i+1/2,j+1/2} - A^{z,n}_{i+1/2,j-1/2}}{\Delta y} \\ b^{y,n}_{i+1/2,j} &= -\frac{A^{z,n}_{i+1/2,j+1/2} - A^{z,n}_{i-1/2,j+1/2}}{\Delta x} \end{aligned} \tag{2.7}$$

Now, we note that $\Omega$ at cell corners is typically obtained by interpolation. If $\Omega$ is obtained from an interpolation of cell-centered quantities*:

$$\Omega_{i+1/2,j+1/2} = \frac{\Omega_{i,j} + \Omega_{i+1,j} + \Omega_{i,j+1} + \Omega_{i+1,j+1}}{4} \tag{2.8}$$

then we could *instead* add the $\Omega_{i,j}$ terms to a cell-centered vector potential $A^z_{i,j}$ and then perform the interpolation to the cell corner to obtain $A^z_{i+1/2,j-1/2}$, as these operations commute. We note that the basic flux-CT scheme cannot be reformulated as such an interpolation. How-

---

* Note that alternatively, recently developed, fully multi-dimensional upwinded approaches may be used for interpolation (Balsara 2012, 2014, 2015; Balsara et al. 2014; Balsara & Dumbser 2015b) The simple interpolation from Tóth (2000) used here in Equation 2.7 is not multi-dimensionally upwinded and therefore may not be stable in extreme applications. In the scope of the present work, we will just consider this simple case, and extensions to multi-dimensional Riemann solvers is left for future work.

ever, as we'll show, the field-CT schemes, as well as the centered difference (CD) CT-like schemes of Tóth (2000) (flux-CD and field-CD) can be reformulated as cell-centered vector potential schemes. We deem these methods CTA/CDA schemes. Additionally, with our formalism, we can construct a new flux-CTA method that is very similar to flux-CT, but effectively uses an extended stencil of numerical fluxes from the Riemann solver to recover the electric fields at the corners. Thus, in the unstructured cell-centered vector potential methods, one updates the cell-averaged vector potential (the primal variable) by the induction equation simply as:

$$A_{i,j}^{z,n+1} = A_{i,j}^{z,n} - \Delta t \Omega_{i,j} \tag{2.9}$$

and from this can recover the vector potential at the corners (auxiliary variables).

Before continuing, we present a brief interlude describing the CD schemes of Tóth (2000) we just introduced. These are variants of the CT method that update a centroidal magnetic field and instead preserve a different discretization of the divergence-free condition. Namely, the sum of the magnetic fluxes through the faces of tilted-squares that enclose each grid cell (see Figure 2.2) is preserved to 0 (sum of fluxes over an enclosed surface adding to 0 is just the integral version of the divergence-free condition per Gauss' Theorem). In concrete terms, the following divergence is preserved:

$$(\nabla \cdot \mathbf{B})_{i,j} = \frac{B_{i+1,j}^{x} - B_{i-1,j}^{x}}{2\Delta x} + \frac{B_{i,j+1}^{y} - B_{i,j-1}^{y}}{2\Delta y} \tag{2.10}$$

With CD schemes, the centroidal magnetic fields are updated as:

$$\begin{aligned} B^{x,n+1}_{i,j} &= B^{x,n}_{i,j} - \Delta t \frac{\Omega_{i,j+1} - \Omega_{i,j-1}}{2\Delta y} \\ B^{y,n+1}_{i,j} &= B^{y,n}_{i,j} + \Delta t \frac{\Omega_{i+1,j} - \Omega_{i-1,j}}{2\Delta x} \end{aligned} \tag{2.11}$$

again, the electric fields may be field or flux interpolated.

It is easy to see that we can reformulate the CD method by updating instead cell-centered magnetic vector potentials according to the induction equation (Equation 2.9), followed by applying the curl-operator:

$$\begin{aligned} B^{x,n}_{i,j} &= \frac{A^{z,n}_{i,j+1} - A^{z,n}_{i,j-1}}{2\Delta y} \\ B^{y,n}_{i,j} &= -\frac{A^{z,n}_{i+1,j} - A^{z,n}_{i-1,j}}{2\Delta x} \end{aligned} \tag{2.12}$$

Thus it becomes clear that we can formulate $4$ basic versions of centroidal vector potential methods: using either the numerical fluxes from the Riemann solver or the field quantities from the base-scheme to obtain $\Omega$ at cell-centers, and preserving either the CT or the CD discretizations of the divergence. We call these methods flux-CTA, field-CDA, flux-CTA, and field-CDA. It turns out (Section 2.3.3) that the last 3 of these methods are identical to the field-CD, flux-CT, and flux-CD methods of Tóth (2000), while the flux-CTA method is similar to flux-CT, but uses a more extended stencil. We can divide each method into two steps: (1) the 'update' step, used to update the primal magnetic vector potentials, and (2) the 'recovery' step, used to obtain the centroidal $B$-field. These steps for the $4$ methods are described in the following subsections.

### 2.3.1 UPDATE STEP

Figure 2.1 shows the stencils used for the update of the primal magnetic vector potentials with the various CTA/CDA schemes.

#### FIELD- UPDATE STEP

In the field-interpolated schemes (field-CTA and field-CDA), the electric field $\mathbf{E} = -\mathbf{v} \times \mathbf{B}$ is estimated at the middle of the timestep by time-averaging the initial state with auxiliary value obtained from the base scheme:

$$\Omega_{i,j} = -\frac{(\mathbf{v} \times \mathbf{B})^n_{i,j} + (\mathbf{v} \times \mathbf{B})^*_{i,j}}{2} \tag{2.13}$$

This electric field is used to update the cell-centered magnetic vector potential $\mathbf{A}_{i,j}$ via the induction equation (Equation 2.9) in the field-CTA and field-CDA schemes.

#### FLUX- UPDATE STEP

In the flux-interpolated schemes (flux-CTA and flux-CDA), the electric field is obtained from combining the upwind flux components of the base scheme

$$\Omega_{i,j} = \frac{1}{4}\left(-f^{x,*}_{i-1/2,j} - f^{x,*}_{i+1/2,j} + f^{y,*}_{i,j-1/2} + f^{y,*}_{i,j+1/2}\right) \tag{2.14}$$

This electric field is used to update the cell-centered magnetic vector potential $\mathbf{A}_{i,j}$ via the induction equation (Equation 2.9) in the flux-CTA and flux-CDA schemes.

### 2.3.2 RECOVERY STEP

Figure 2.2 shows the stencils for the recovery of the centroidal magnetic fields with the various CTA/CDA schemes.

#### CT RECOVERY STEP

To recover the centroidal $B$-field, first the magnetic vector potentials are interpolated to the corners via Equation 2.8, followed by recovery of the face-averaged magnetic fields by Equation 2.7, and finally by the computation of the cell-averaged magnetic fields using Equation 2.5. The field-CTA and flux-CTA schemes use this recovery method, which preserves the discretized divergence of Equation 2.4.

#### CD RECOVERY STEP

To recover the centroidal $B$-field, use Equation 2.12. The field-CDA and flux-CDA schemes use this recovery method, which preserves the discretized divergence of Equation 2.10.

### 2.3.3 CORRESPONDENCE BETWEEN CTA/CDA AND CT/CD METHODS

The field-CD and field-CDA schemes are identical. In field-CD, one calculates cell-centered temporally interpolated electric fields (Equation 28 of Tóth (2000)) to update the cell-centered magnetic fields via Equation 2.11. The field-CDA uses the same electric fields (Equation 2.13) added to cell-centered magnetic vector potentials, and the identical cell-centered magnetic field is obtained via Equation 2.12.

The flux-CD and flux-CDA schemes are identical. In flux-CD, one calculates cell-centered spatially-interpolated electric fields obtained from the numerical flux (Equation 31 of Tóth (2000)) to update the cell-centered magnetic fields via Equation 2.11. The field-CDA uses the same electric fields (Equation 2.14) added to cell-centered magnetic vector potentials, and the identical cell-centered magnetic field is obtained via Equation 2.12. The field-CT and field-CTA schemes are also identical. In field-CT, one uses spatial and temporal interpolation of the electric fields at the surrounding cell centers to cell corners (Equation 16 of Tóth (2000)). As the operations are linear and hence commutative one can equivalently add the same temporally interpolated electric fields terms to the vector potentials at the cell centers and then perform the spatial interpolation (as is done in the field-CTA scheme). This recovers the same vector potential at the cell corner as the 'underlying' vector potential being evolved with the field-CT scheme.

The flux-CT and flux-CTA schemes differ slightly in that flux-CTA uses a more extended stencil in the recovery of the centroidal magnetic field. In flux-CT, one uses spatial interpolation of the numerical fluxes from the Riemann solver to deduced electric fields at the surrounding faces to cell corners (Equation 19 of Tóth (2000)). This electric field can be thought of as being added to the 'underlying' cell-corner vector potential in the CT scheme. In 2D, this corner electric field is recovered from 4 surround fluxes. But in the field-CTA scheme, the obtained cell-corner electric field is instead obtained using 12 surround fluxes. That is, the field is obtained from spatial interpolation of flux-deduced electric fields at the 4 surrounding cell centers (Equation 2.8), and the electric fields at each cell center are deduced by the fluxes of the 4 cell faces (Equation 2.14).

We point out that the CTA/CDA schemes are conservative, meaning that they preserve the mean magnetic field (a conserved quantity of ideal MHD), as they are equivalent to the conservative CT/CD schemes. Tóth (2000) shows how to reformulate CT/CD schemes as conservative finite volume schemes with extended stencils, which illustrates by the mean magnetic field is preserved by the method.

### 2.3.4 PERIODIC BOUNDARY CONDITIONS

The magnetic vector potential is not periodic under periodic boundary conditions (only its curl is). Instead, **A** can always be decomposed into a time-variable periodic part and a static mean-field part:

$$\mathbf{A}(x,y,t) = \mathbf{A}_{\text{periodic}}(x,y,t) + \mathbf{A}_{\text{mean}}(x,y) \tag{2.15}$$

$\mathbf{A}_{\text{mean}}(x,y)$ is a function chosen to recover the mean magnetic field, which is an invariant of ideal MHD. The function $\mathbf{A}_{\text{mean}}(x,y)$ is used to adjust the vector potential of translated 'ghost' cell copies when considering neighbors of cells beyond the boundary of the domain.

## 2.4 NUMERICAL TESTS

We carry out a few simple tests to demonstrate the four CTA/CDA schemes, and compare the results to those obtained with the base finite volume scheme and the flux-CT scheme. As three out of the four CTA/CDA schemes are equivalent to CT/CD schemes tested extensively elsewhere (Tóth 2000), we do not delve into carrying out many test problems. The purpose of this section is to show the proof-of-concept that these schemes can be recast in terms of a vector potential, and to highlight that all the CTA/CDA schemes perform better than and avoid artifacts of the base finite volume scheme. We do, however, show that the vector potential schemes are indeed second-order, and free of numerical artifacts seen in non divergence-preserving methods such as the finite volume scheme.

### 2.4.1 ROTATED ALFVÉN WAVE

First, we solve a smooth 1D problem rotated by an angle $\alpha$ on a 2D mesh to test the capabilities of the schemes in 2D and demonstrate second-order convergence. We use the circularly polarized Alfvén wave initial conditions (Tóth 2000), propagating at an angle $\alpha = 30°$. The domain is periodic with size $[1/\cos\alpha, 1/\sin\alpha]$. The initial conditions are $\rho = 1$, $v_{||} = 0$, $p = 0.1$, $B_{||} = 1$ $v_{\perp} = B_{\perp} = 0.1 \sin\left[2\pi\left(x\cos\alpha + y\sin\alpha\right)\right]$, $v_z = B_z = 0.1\cos\left[2\pi\left(x\cos\alpha + y\sin\alpha\right)\right]$, $\gamma = 5/3$.

The computational domain is an $N \times N$ grid with $\Delta x/\Delta y = \tan\alpha$. The simulation is run until $t = 1$, where the wave returns to its initial state.

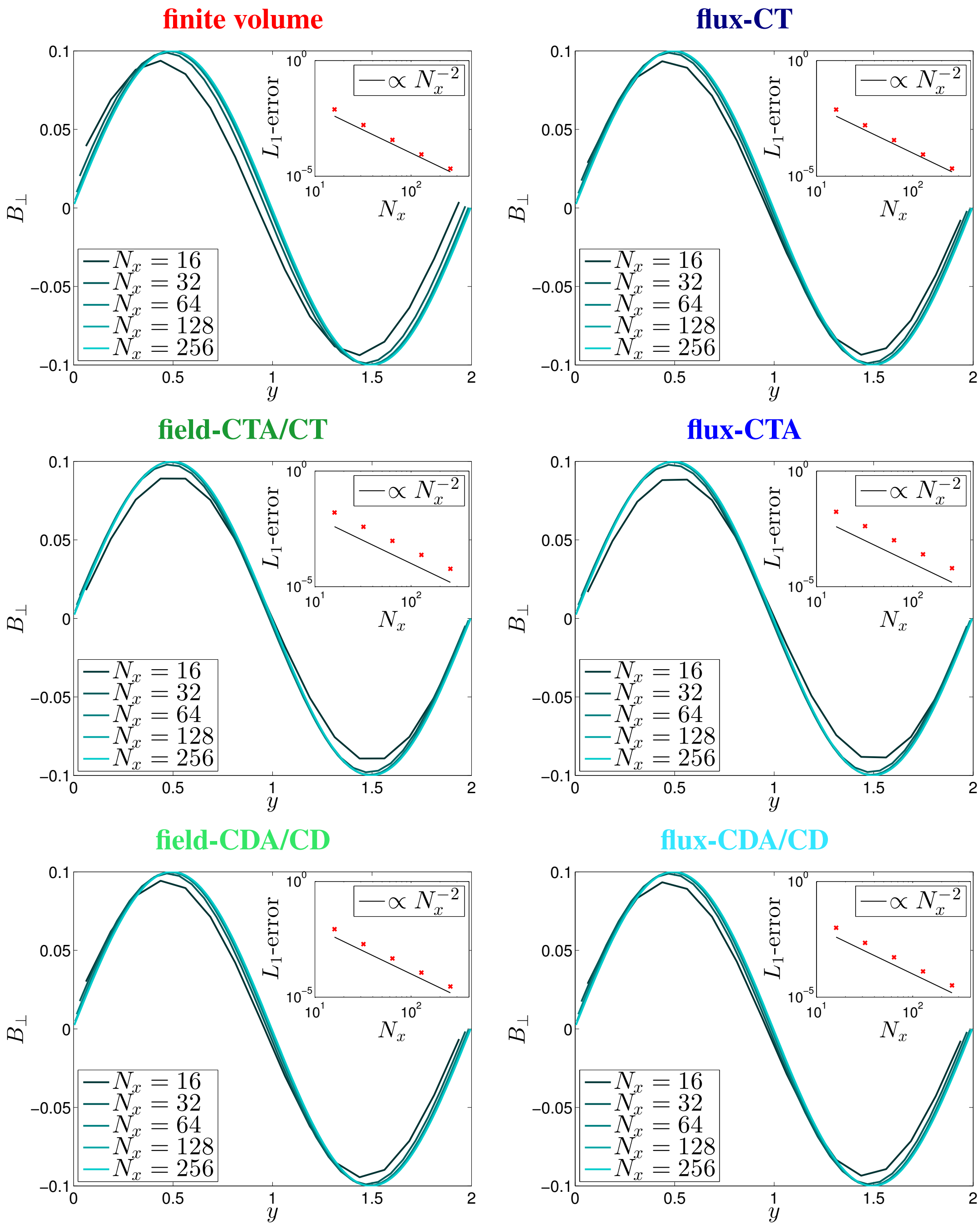

finite volume

flux-CT

field-CTA/CT

flux-CTA

field-CDA/CD

flux-CDA/CD

**Figure 2.3:** Convergence test of the rotated Alfvén-wave problem for the various methods. All methods show good behavior and second-order convergence, as expected.

Figure 2.3 shows the results of $B_\perp$ along the $y$-axis at $t = 1$ for the various schemes. Computed is the $\mathrm{L}_1$ norm error for the magnetic field in the entire domain. All schemes show good behavior and second-order convergence, as expected. The base finite volume scheme performs well on this simple test problem, showing the smallest errors. However, as we'll see in the following subsections, the finite volume scheme can show artifacts from the lack of enforcing the $\nabla \cdot \mathbf{B} = 0$ condition for more complicated tests.

The vector potential methods are shown to be second-order accurate, (unsurprisingly, as they are equivalent to second-order CT schemes), despite the fact that the order of spatial derivatives in the MHD equations using the vector potential increases by one.

### 2.4.2 MAGNETIC VORTEX

We solve the advection of the magnetized vortex problem from Balsara (2004, 2009), which consists of a smoothly varying and dynamically stable configuration. This genuinely two-dimensional, dynamically active problem is a useful test of second-order convergence. The problem is set up on a two-dimensional periodic domain $[-5, 5] \times [-5, 5]$. The adiabiatic index is $\gamma = 5/3$. The initial condition is given by an unperturbed component $(\rho, P, v_x, v_x, B_x, B_y) = (1, 1, 1, 1, 0, 0)$ and a perturbed component describing the vortex:

$$\delta P = \frac{1}{8\pi}\left(\frac{\mu}{2\pi}\right)^2 (1 - r^2)e^{1-r^2} - \frac{1}{2}\left(\frac{\kappa}{2\pi}\right)^2 e^{1-r^2}, \tag{2.16}$$

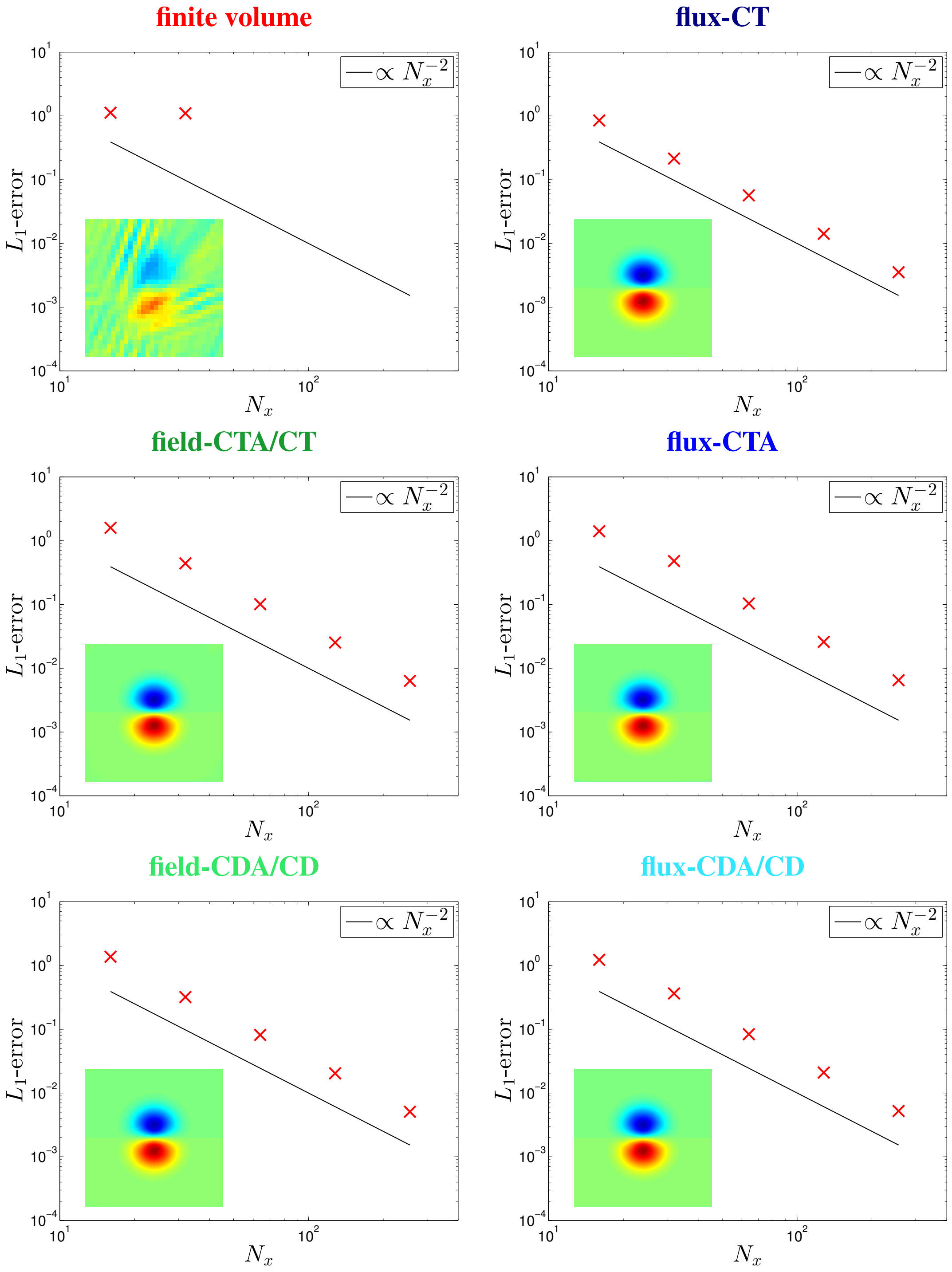

**Figure 2.4:** Convergence test of the dynamical vortex problem. All methods show second-order convergence, except the base finite volume scheme, which is numerically unstable due to divergence errors. Insets show the solution of $B_x$ at $t = 10$ at the highest resolution run (except for the finite volume scheme, where we show the solution at lower resolution because the higher resolution solution completely blew up).

$$(\delta v_x, \delta v_y) = (-y, x)\frac{\kappa}{2\pi}e^{0.5(1-r^2)}, \tag{2.17}$$

and

$$\delta A_z = \frac{\mu}{2\pi}e^{0.5(1-r^2)}. \tag{2.18}$$

with $\kappa = 1$, $\mu = \sqrt{4\pi}$, and $r = \sqrt{x^2 + y^2}$. These equations describe a vortex in dynamical balance, in which the circular motion in the vortex produces a centrifugal force and the magnetic field produces a centripetal force.

The solution returns to its initial state at $t = 10$, and we compute the error of $B_x$. Figure 2.4 shows that all the CTA/CDA schemes are indeed second-order accurate for this complex, dynamical problem. Our implementation of the base finite volume scheme, however, is numerically unstable by $t = 10$ due to divergence errors.

### 2.4.3 ROTATED SHOCK

We simulate a shock tube traveling at an angle $\alpha = \tan^{-1}(2)$ with respect to the grid, similar to the setup of Tóth (2000). The left initial state is $(\rho, v_{||}, v_{\perp}, p, B_{||}, B_{\perp}) = (1, 10, 0, 20, 5/\sqrt{4\pi}, 5/\sqrt{4/\pi})$ and the right initial state is $(\rho, v_{||}, v_{\perp}, p, B_{||}, B_{\perp}) = (1, -10, 0, 1, 5/\sqrt{4\pi}, 5/\sqrt{4/\pi})$. The fluid has adiabatic index $\gamma = 5/3$. We perform the test on a $256 \times 128$ resolution domain $[0, 4] \times [0, 2]$, and evolve the simulation until $t = 0.04$

Figure 2.5 shows the normal component of the magnetic field across the shock. The exact solution is constant, while the numerical methods show oscillation about this value but gen-

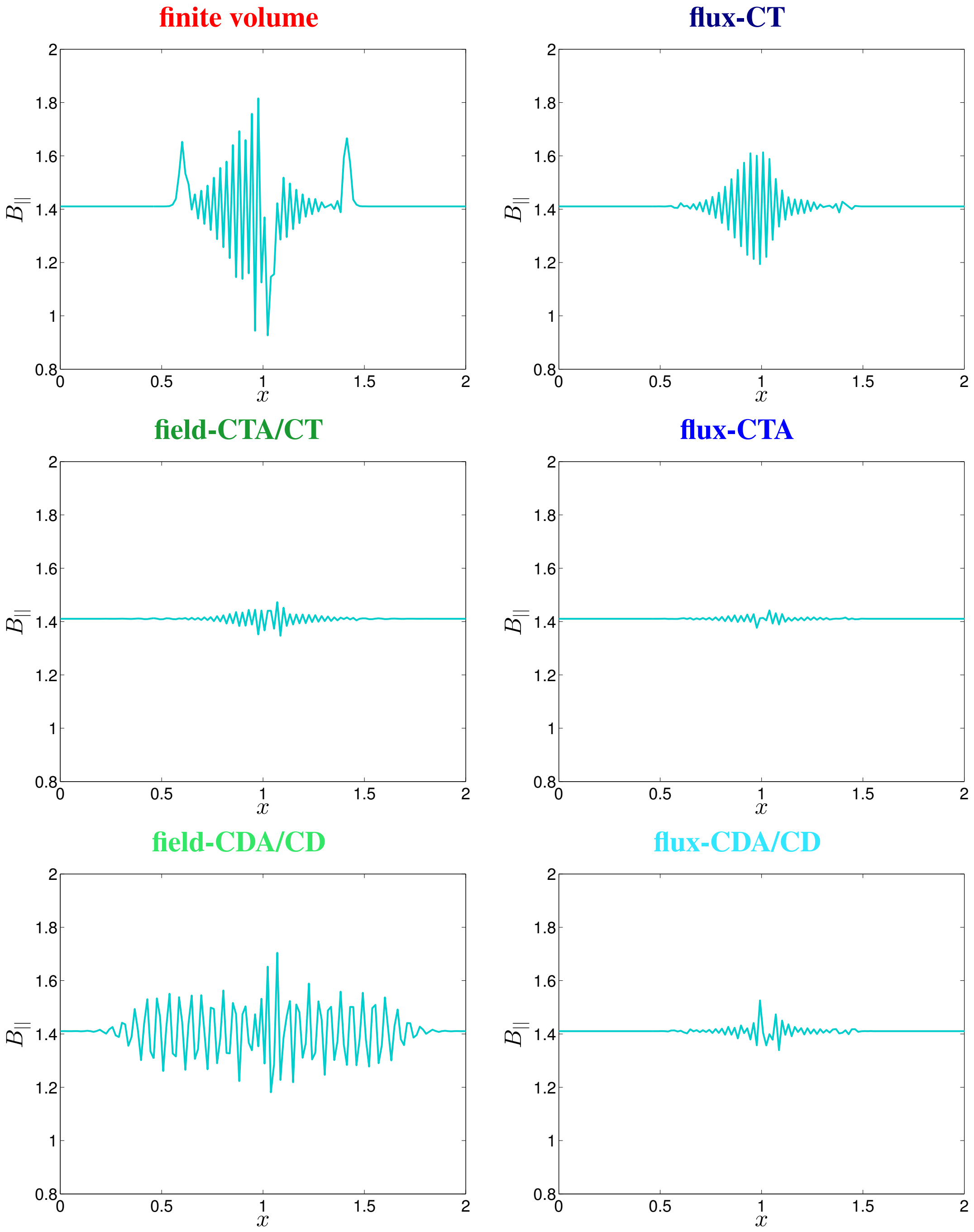

finite volume

flux-CT

field-CTA/CT

flux-CTA

field-CDA/CD

flux-CDA/CD

**Figure 2.5:** The normal component of the magnetic field across the rotated strong shock problem for the various methods. The exact solution is constant. The various methods recover this value, but show oscillations around it.

erally have good behavior and recover the right jump conditions in the other fluid variables (not shown). Non-conservative methods are known to perform poorly and give incorrect jump conditions for this test (Tóth 2000).

### 2.4.4 ORSZAG-TANG VORTEX

We simulate the classic decaying supersonic turbulence test of Orszag & Tang (1979). The initial conditions are given by $\rho = \gamma^2/(4\pi)$, $v_x = -\sin(2\pi y)$, $v_y = \sin(2\pi x)$, $p = \gamma/(4\pi)$, $A_z = \cos(4\pi x)/(4\pi\sqrt(4\pi)) + \cos(2\pi y)/(2\pi\sqrt(4\pi))$. The domain is a periodic unit square $[0,1] \times [0,1]$ and the adiabatic index is $\gamma = 5/3$.

Figure 2.6 shows the results of the simulation at $t = 0.5$. The CTA/CDA and CT schemes give consistent results, while the finite volume scheme shows ringing pattern artifacts in the density field.

### 2.4.5 SUMMARY

A summary of the accuracies of all the schemes is shown in Figure 2.7. All the CTA/CDA and CT schemes perform well. Our finite volume scheme however is unable to solve the dynamical vortex problem and also shows artifacts in the density field in the Orszag-Tang test. This illustrates the importance of maintaining the divergence-free condition when solving the MHD equations.

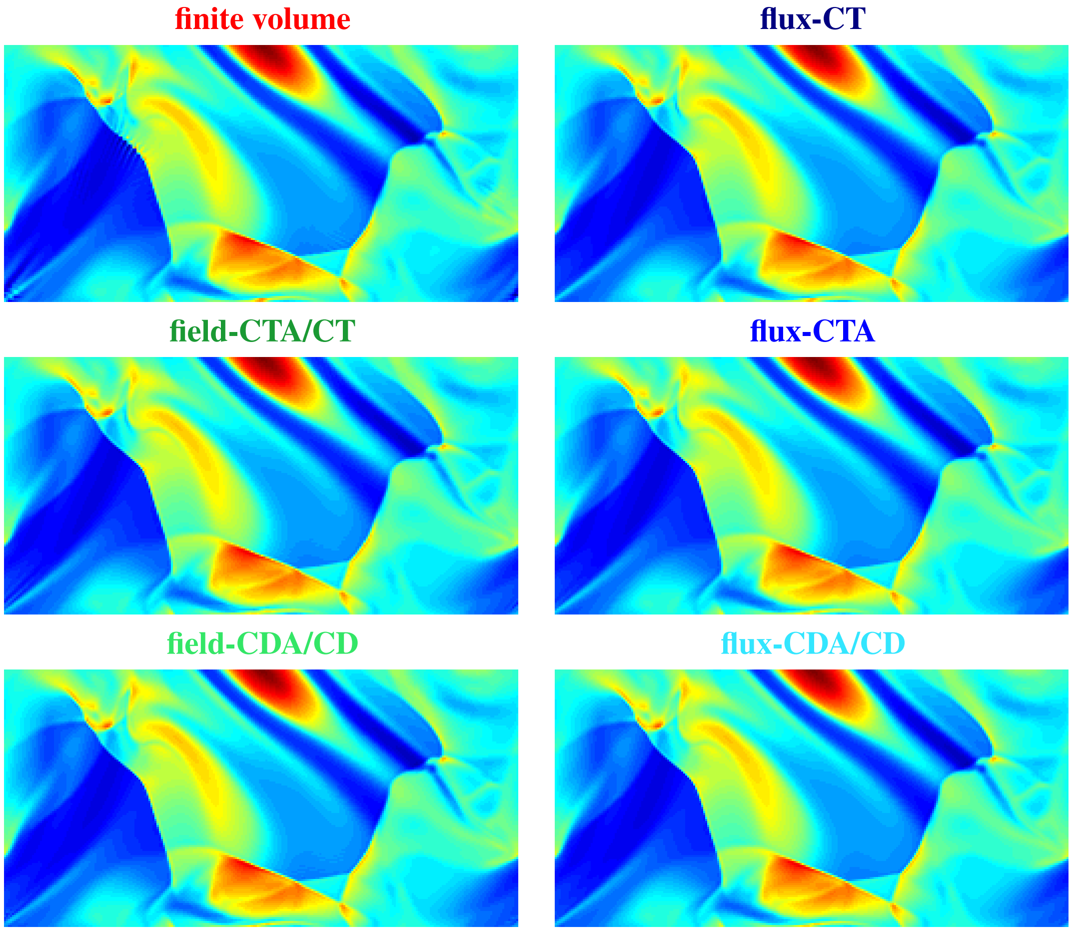

finite volume

flux-CT

field-CTA/CT

flux-CTA

field-CDA/CD

flux-CDA/CD

**Figure 2.6:** The results of the Orszag-Tang test for the various methods at $t = 0.5$. Shown is the density on the top half pf the domain (bottom half is rotationally symmetric), with a rainbow color scheme with range $[0.06, 0.5]$. All CTA/CDA/CT schemes show good behavior. The base finite volume scheme shows numerical artifacts (ringing patterns in the density structure) due to the lack of a $\nabla \cdot \mathbf{B}$ constraint.

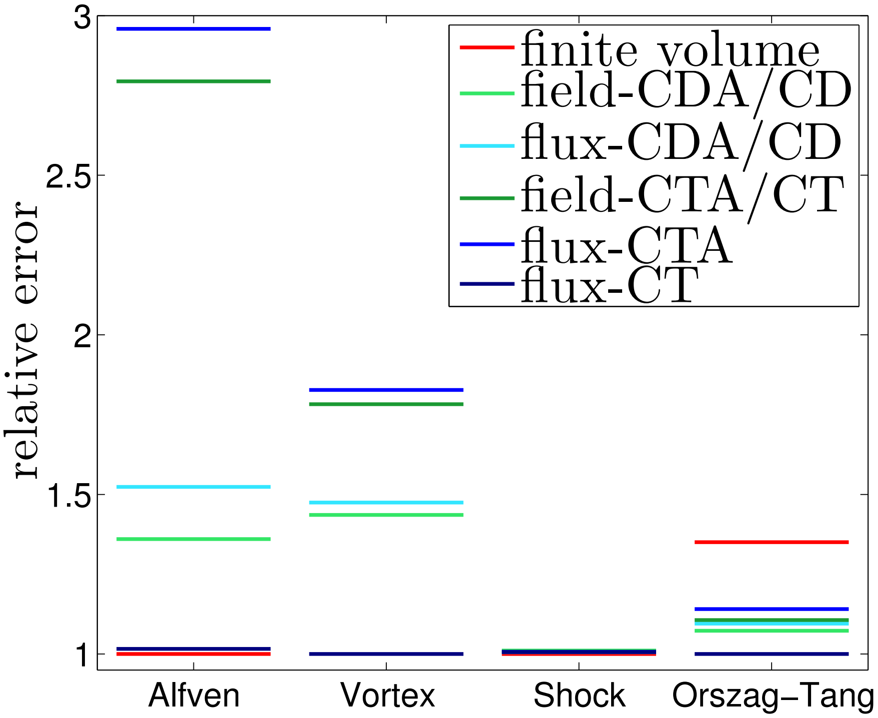

**Figure 2.7:** Comparison of the relative errors of the schemes compared to the best scheme for the rotated Alfvén wave, vortex, rotated shock, and Orszag-Tang tests. We compute the error in the magnetic field for the Alfvén wave and vortex problems, and the error in the density field for the shock and Orszag-Tang problems. For the Orszag-Tang test, the 'exact' solution is taken to be a $2\times$ resolution simulation with the flux-CT method.

## 2.5 GENERALIZATION TO UNSTRUCTURED GRIDS

We provide an overview of how to extend the CTA/CDA schemes to unstructured grids. The primary variable being updated is the magnetic vector potential $\mathbf{A}_{i,j}$ located at the center-of-mass of each irregular cell.

The field-update step (Section 2.3.1) is the simplest to generalize. Equation 2.13 which updates the electric field at the center-of-mass of the cell still applies. Nothing special needs to be done to update the vector potential.

Generalization of the flux-update step (Section 2.3.1) is more complicated. In 3D, at each face, the numerical fluxes give two components of the electric field (in the plane of the face). Various strategies may be taken to reconstruct the electric field at the center of mass of the cell. One approach could be to take a least-squares fit approach, i.e., find the centroidal electric field that, when extrapolated to the face centers, gives the minimum deviation from the flux-obtained fields.

To generalize the recovery of the centroidal magnetic fields of each cell, it is best to use the integral form of the $\mathbf{B} = \nabla \times \mathbf{A}$ definition. With the integral form, $\mathbf{A}$ need not be assumed to be differentiable. Of course, in the simple case of a Cartesian grid, we have used finite-difference operations to recover $\mathbf{B}$. But they correspond to an integral-form recovery technique. This is akin to how finite volume can be expressed as finite difference methods.

The CT recovery step (Section 2.3.2) can be obtained from the integral relation:

$$\int_V \mathbf{B}\,dV = \int_{\partial V} \hat{\mathbf{n}} \times \mathbf{A}\,dS \tag{2.19}$$

In fact, one can recover Equations 2.3 and 2.5 for the Cartesian grid from discretizing this identity. For a general grid, one may use a variety of second-order techniques to evaluate this integral. For example, one may interpolate the magnetic vector potential from cell centroids to the centers-of-masses of the faces, and carry out the integral with just one quadrature point per face, sufficient for second-order accuracy.

The CD recovery step (Section 2.3.2) can be generalized as follows. It requires a construction of a dual triangular-mesh in 2D (tetrahedral in 3D), e.g. a Delaunay triangularization/tetrahedraliztion of the centroids of the cells. The magnetic vector potentials are specified at the triangle vertices. Thus, the magnetic flux $\Phi_B$ through the each faces of the triangle can be recovered from discretizing

$$\Phi_B = \oint_{\partial S} \mathbf{A} \cdot d\ell \tag{2.20}$$

which, in 2D, just says that the outward magnetic field in a face on a triangle is:

$$b^{\mathrm{out}} = \frac{A^{\mathrm{L}} - A^{\mathrm{R}}}{\Delta\ell} \tag{2.21}$$

where $\Delta\ell$ is the length of the face and $A^{\mathrm{L}}$ is the magnetic vector potential at the left edge of the face, $A^{\mathrm{R}}$ corresponds to the right edge (notice the relationship between this equation and Equation 2.7). Once the outward magnetic fields of a triangle are known, it is easy to recover the unique triangle volume-averaged magnetic field that gives consistent outward magnetic fields on the faces. In 2D, there are the magnetic fluxes on 3 faces known, but only 2 are independent by the divergence-free condition (sum of fluxes sum to 0). There are also 2 components of $\mathbf{B}$. Hence, there exists a unique solution to the simple linear problem:

$$\begin{pmatrix} \mathcal{A}_{x,1} & \mathcal{A}_{y,1} \\ \mathcal{A}_{x,2} & \mathcal{A}_{y,2} \\ \mathcal{A}_{x,3} & \mathcal{A}_{y,3} \end{pmatrix} \begin{pmatrix} B_x \\ B_y \end{pmatrix} = \begin{pmatrix} \Phi_{B,1} \\ \Phi_{B,2} \\ \Phi_{B,3} \end{pmatrix} \tag{2.22}$$

(where the $\mathcal{A}_i$ are outward face area vectors and the $\Phi_{B,i}$ are outward magnetic fluxes) which can be solved to obtain $\mathbf{B}$. Thus one obtains volume-averaged magnetic fields for each triangle in the dual triangulation of the mesh, which, when projected along triangle faces, are continuous across faces. The recovery is analogous for the tetrahedra in 3D. In the 2D Cartesian case (see Figure 2.2), the recovery technique means magnetic fields can be recovered for each triangle that make up the tilted square enclosing a cell, as well as magnetic fields at each triangle face. By construction, the total magnetic flux across any enclosed surface sums to zero, hence the divergence is preserved on the tilted-square. In general, recovery of the cell-averaged magnetic fields can be obtained easily from averaging the surrounding triangle-averaged magnetic fields, weighting by the area of intersection between the triangle and cell. In the case of a Cartesian grid, all these steps to recover the cell-centered magnetic field reduce to Equation 2.12. We present the generalization of the field-CDA scheme on a moving unstructured Voronoi mesh in Mocz et al. (2016).

We point out that the field-CDA scheme has the simplest generalization to unstructured meshes, since no irregular mesh interpolation or least-squares fitting are required. In Tóth (2000), field-CD and flux-CT shown to have some of the best properties from among all CT/CD and divergence cleaning methods tested on a variety of test problems.

## 2.6 CONCLUSIONS

We have shown that several 2nd-order staggered CT schemes and CD schemes can be recast in terms of centroidal vector potentials as the primal variable. Using this formalism, we have also introduced a new centroidal CT scheme. We implemented and tested these vector potential schemes to demonstrate that they behave well and avoid known artifacts of the finite volume scheme which is unconcerned about preserving the divergence-free condition at the discretized level. Reformulating CT schemes in terms of the vector potential can allow for different extensions of the CT method, as well as simple generalizations to unstructured and moving grids with improved memory requirements and memory access. Centroidal methods may also simplify the implementation of CT on an adaptively-refined mesh (AMR), where standard CT faces challenges at fine and coarse level mismatch, and specific care (such as restriction, prolongation, and reflux-curl operations (Miniati & Martin 2011)) has to be taken to obtain divergence-free magnetic fields. Knowing the vector potential at cell-centers, instead of the just the magnetic field, allows for a unique, divergence-free reconstruction of the magnetic field anywhere in the domain. We have recently implemented and tested the field-CDA scheme presented in this paper on a quasi-Lagrangian 3D moving unstructured Voronoi mesh in Mocz et al. (2016).

Despite the fact that in terms of the vector potential the order of spatial derivatives in the MHD equations increases by one, the order of accuracy of the methods is not necessarily reduced by one; this is a misconception in the literature. With appropriate construction of vector potential methods, they are equivalent to CT schemes. Additionally, the assumption that $\mathbf{A}$ is differentiable needs not be made (as is often incorrectly assumed for vector potential methods), as the vector potential methods are equivalent to CT algorithms which do not make this assumption.

The vector potential methods described here are based off simple second-order CT schemes, but future work can involve incorporating some of the recent advances in face-centered CT into the centroidal vector potential schemes, including multi-dimensional Riemann solvers and higher-order extensions.

*We cannot solve our problems with the same thinking we used when we created them.*

Albert Einstein

# 3

# A 2D constrained transport scheme for MHD on unstructured meshes

– based on –

Mocz, P., Vogelsberger, M., & Hernquist, L. (2014a). A constrained transport scheme for MHD on unstructured static and moving meshes. *MNRAS*, 442, 43–55.

Magnetic fields play an important role in many astrophysical systems and a detailed understanding of their impact on the gas dynamics requires robust numerical simulations. Here we present a new method to evolve the ideal magnetohydrodynamic (MHD) equations on unstructured static and moving meshes that preserves the magnetic field divergence-free constraint to machine precision. The method overcomes the major problems of using a cleaning scheme on the magnetic fields instead, which is non-conservative, not fully Galilean invariant, does not eliminate divergence errors completely, and may produce incorrect jumps across shocks. Our new method is a generalization of the constrained transport (CT) algorithm used to enforce the $\nabla\cdot\mathbf{B}=0$ condition on fixed Cartesian grids. Preserving $\nabla\cdot\mathbf{B}=0$ at the discretized level is necessary to maintain the orthogonality between the Lorentz force and $\mathbf{B}$. The possibility of performing CT on a moving mesh provides several advantages over static mesh methods due to the quasi-Lagrangian nature of the former (i.e., the mesh generating points move with the flow), such as making the simulation automatically adaptive and significantly reducing advection errors. Our method preserves magnetic fields and fluid quantities in pure advection exactly.

## 3.1 INTRODUCTION

The equations of fluid dynamics and magnetohydrodynamics (MHD) may be evolved using a variety of numerical approaches. One can choose from a number of discretizations that are formally intended to yield a solution that is accurate to some order $n$. However, a system of partial differential equations for physical flows also gives rise to conserved quantities due to the symmetries of the problem and these quantities are not necessarily preserved with some algorithms. Such conserved quantities for the MHD equations include mass, momentum, angular momentum, energy, and the solenoidal nature of the magnetic field. It then becomes a concern to design techniques in a clever way such that the discrete representations of these conserved quantities are in fact preserved to machine precision. Failure to do this may result in instabilities and unphysical solutions; that is, the system's quantity that should be conserved may chaotically evolve away from its initial value. One well-known example of such a phenomenon occurs when evolving an $N$-body system with a non-symplectic time integrator, which does not conserve the total energy and hence may lead to energy drifts and decaying orbits.

In this work, we propose a scheme for evolving the MHD equations on a moving mesh such that conservation of mass, momentum, and energy, and, importantly, the solenoidal (divergence-free) nature of the magnetic field is preserved. On static Cartesian meshes, the constrained transport (CT) algorithm achieves this goal. It uses a finite volume formalism to evolve the density, momentum, and energy, and exploits Stokes' theorem and uses a face-averaged representation of the magnetic fields (called the 'staggered-mesh' approach) to enforce $\nabla\cdot\mathbf{B}=0$ (Evans & Hawley 1988). The CT algorithm has been described in the literature as being quite difficult (if not impossible) to extend to an unstructured mesh (Duffell & MacFadyen 2011; Pakmor et al. 2011; Pakmor & Springel 2013) and leading to the development of alternate divergence-cleaning schemes to keep $\nabla\cdot\mathbf{B}$ small but non-zero on moving meshes based on the Powell (Powell et al. 1999) and Dedner (Dedner et al. 2002) cleaning methods. Moving mesh methods for MHD with cleaning schemes have been described by Duffell & MacFadyen (2011); Pakmor et al. (2011); Gaburov et al. (2012); Pakmor & Springel (2013). Additionally, there have been recent advances in designing robust mesh-less based methods for MHD (Gaburov & Nitadori 2011; Tricco & Price 2013), which still, however, require cleaning schemes. These schemes alter the MHD equations and may add source terms in an attempt to control the divergence errors, which has the unwanted side-effect of making the schemes non-conservative. Additionally, such an approach loses the moving mesh's Galilean invariant properties (e.g. solving pure advection problems is diffusive). One approach to improve these methods has been to develop a *locally* divergence-free formulation based on the discontinuous Galerkin method in the work presented in Mocz et al. (2014b), where local divergence-free basis functions are used to represent the solution on each cell. In this paper we solve the outstanding problem of designing a *globally* divergence-free, conservative, finite volume based algorithm on an unstructured moving mesh.

Coupling a CT algorithm with a moving mesh technique is clearly highly desirable. The moving mesh algorithm for solving the inviscid Euler equations was developed recently by Springel (2010) and implemented in the code AREPO. The moving mesh algorithm largely eliminates a number of well-know weaknesses of both static Cartesian/adaptive mesh refinement (AMR) approaches and pseudo-Lagrangian smoothed-particle hydrodynamics (SPH). The mesh-generating points in the algorithm can be set to move with the fluid flow, making the scheme quasi-Lagrangian. The method has automatic adaptivity, is Galilean-invariant, and significantly reduces advection errors. Contact discontinuities resulting from shocks are preserved to significantly greater accuracy. In addition, conditions on the size of the time-step are less severe than on a static mesh in the cases of flows with high-Mach number bulk motions, since fluxes across cells are always calculated in the rest-frame of the faces. A method for solving the MHD equations on a moving mesh will automatically gain these benefits of the Lagrangian nature of the scheme and, ideally, should not suffer any significant disadvantage compared to a static mesh approach. Since methods exist to preserve the divergence-free condition on structured fixed grids, it is important to extend this to unstructured meshes so that if differences are observed in MHD simulations run on static and moving meshes, then they can be attributed to the advantages of the moving mesh approach and not as an artefact produced by divergence errors.

The CT method proposed here can also be applied to static arbitrarily unstructured grids, where CT algorithms are lacking. A number of simulations use non-Cartesian static grids, dictated by the geometry/symmetry of the problem, as a way of achieving greater accuracy and by using fewer grid cells. For example, the MHD solver in Florinski et al. (2013) was developed for a hexagonal spherical geodesic grid as a way to improve the simulation of astrophysical flows of partially ionized plasmas around a central compact object. However, such methods use cleaning schemes instead of CT to handle the magnetic field, and would benefit greatly from the CT method described in what follows.

A robust code for solving the MHD equations as accurately as possible would have many astrophysical applications because magnetic fields are ubiquitous in the Universe. For example, the magnetorotational instability in accretion discs (Balbus & Hawley 1998) generates turbulence and mediates angular momentum transfer. Discs around supermassive black holes may be levitated by magnetic pressure (Gaburov et al. 2012). Magnetic fields are key in the production of relativistic jets and outflows from compact sources (Blandford & Znajek 1977; Blandford & Payne 1982). Magnetic fields under a vertical gravitational field as in the disc of a galaxy leads to the Parker instability, which is thought to play an important role in the evolution of the interstellar medium (Parker 1966, 1967). Interstellar turbulence and star formation are linked with magnetized plasma processes (Goldreich & Sridhar 1995). Cosmic magnetic fields are likely to have a primordial origin which leads to imprints on the temperature and polarization anisotropies of the cosmic microwave background radiation (Grasso & Rubinstein 2001). These seed fields are amplified during the formation and evolution of galaxies. Radio lobes of galaxies may also play an important role in enhancing the magnetic fields in the intergalactic medium (Gopal-Krishna & Wiita 2001). Magnetic fields may be responsible for suppressing strong isotropic turbulence and conduction in clusters and make it possible for stable, 100 kpc-scale high-density arms to exist in the cluster environment (Sanders et al. 2013). The strength and topology of magnetic fields are responsible for determining the propagation of cosmic rays in galaxies (Strong & Moskalenko 1998). Magnetic fields are also present in a wide variety of stars and play a significant role in their evolution (Donati & Landstreet 2009). Many of these problems are suitable for study by a moving mesh approach and up until now a divergence-free MHD solver has been lacking. This paper lays the framework for implementing a divergence-preserving algorithm for robust evolution of the MHD equations in moving mesh codes such as AREPO (Springel 2010) and TESS (Duffell & MacFadyen 2011).

In Section 3.2 we describe the details of the numerical method. In Section 3.3 we show the results of numerical tests (with comparisons to fixed grid CT and the Powell cleaning scheme on a moving mesh) demonstrating that the method works well and has several advantages over the other two techniques. In Section 3.4 we discuss variations of our method and future directions. In Section 3.5 we provide concluding remarks.

## 3.2 NUMERICAL METHOD FOR CT ON STATIC AND MOVING UNSTRUCTURED MESH

This section is dedicated to describing the second-order numerical method in detail. Our method is implemented in 2D in MATLAB. The method can be generalized to 3D (see section 3.2.3). For reference, a flow chart of our numerical algorithm is presented in Figure 3.1.

### 3.2.1 THE MAGNETOHYDRODYNAMIC EQUATIONS

The ideal MHD equations can be written as a system of conservation laws:

$$\frac{\partial \mathbf{U}}{\partial t} + \nabla \cdot \mathbf{F} = 0 \tag{3.1}$$

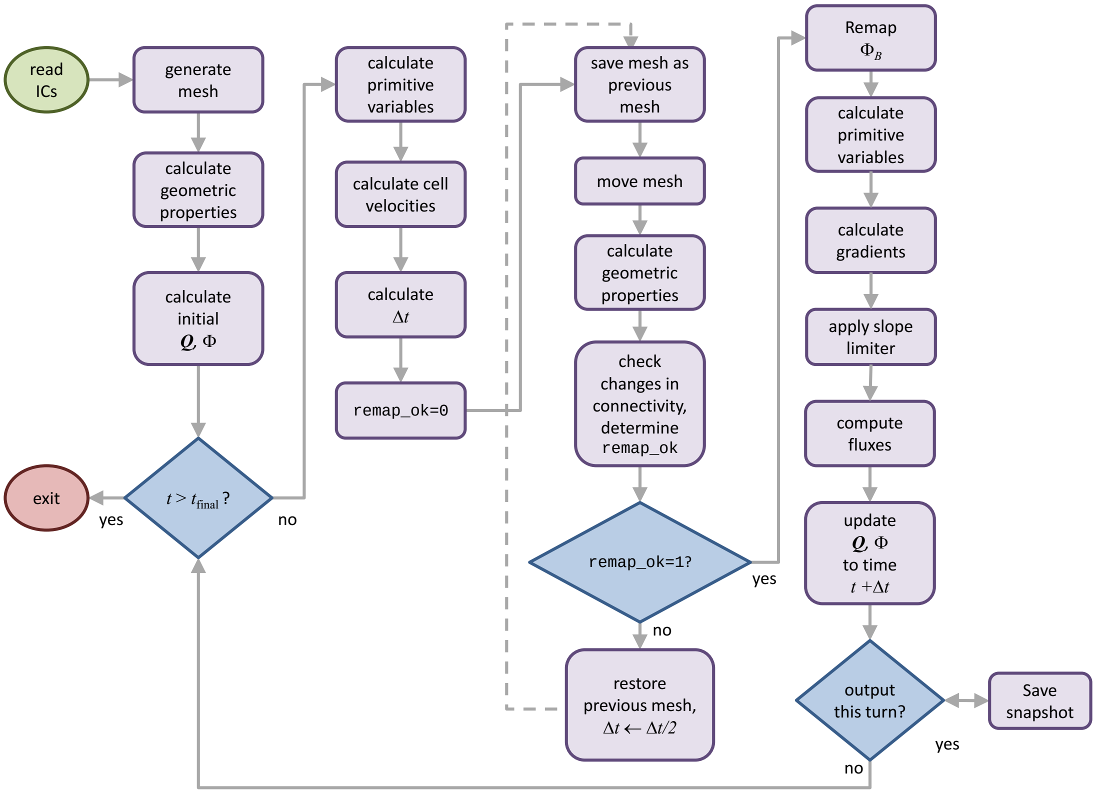

**Figure 3.1:** A flow chart of the CT algorithm for a moving mesh. After initialization, the code enters the main loop. In each iteration of the loop, the system advances by a time interval $\Delta t$ as long as the mesh connectivity does not change too drastically (in which case the flag `remap_ok` is set to 1), else the timestep $\Delta t$ is halved and the system attempts to update itself according to this new timestep.

where $\mathbf{U}$ is the vector of the conserved variables and $\mathbf{F}(\mathbf{U})$ is the flux, namely:

$$\mathbf{U} = \begin{pmatrix} \rho \\ \rho\mathbf{v} \\ \rho e \\ \mathbf{B} \end{pmatrix}, \quad \mathbf{F}(\mathbf{U}) = \begin{pmatrix} \rho\mathbf{v} \\ \rho\mathbf{v}\mathbf{v}^T + p - \mathbf{B}\mathbf{B}^T \\ \rho e\mathbf{v} + p\mathbf{v} - \mathbf{B}(\mathbf{v}\cdot\mathbf{B}) \\ \mathbf{B}\mathbf{v}^T - \mathbf{v}\mathbf{B}^T \end{pmatrix} \tag{3.2}$$

where $p = p_{\mathrm{gas}} + \frac{1}{2}\mathbf{B}^2$ is the total gas pressure, $e = u + \frac{1}{2}\mathbf{v}^2 + \frac{1}{2\rho}\mathbf{B}^2$ is the total energy per unit mass, $u$ is the thermal energy per unit mass. The equation of state for the fluid is given by $p = (\gamma - 1)\rho u$. We describe how to discretize and solve these equations on an unstructured moving mesh with CT.

### 3.2.2 FINITE VOLUME APPROACH ON A MOVING MESH

A finite volume strategy is used to update the density, momentum, and energy of the cells (but the magnetic fields require a different approach). Our method follows that of Springel (2010) closely, except for minor modifications which we point out, which are needed to link the method with our CT scheme to update the magnetic fields.

The domain is discretized into cells created by a Voronoi tessellation from mesh generating points. For each cell, we define volume averaged quantities (‘conservative variables’): the total mass $m_i$, momentum $\mathbf{p}_i$, and energy $E_i$, given by:

$$\mathbf{Q}_i = \begin{pmatrix} m_i \\ \\ \mathbf{p}_i \\ \\ E_i \end{pmatrix} = \int_{V_i} \tilde{\mathbf{U}}\, dV \tag{3.3}$$

where $V_i$ is the volume of cell $i$, and

$$\tilde{\mathbf{U}} = \begin{pmatrix} \rho \\ \\ \rho\mathbf{v} \\ \\ \rho e \end{pmatrix} \tag{3.4}$$

By Gauss' theorem, the conservation laws for a moving cell can be rewritten as:

$$\frac{d\mathbf{Q}_i}{dt} = -\int_{\partial V_i} \left(\mathbf{F}(\tilde{\mathbf{U}}) - \tilde{\mathbf{U}}\mathbf{w}^T\right)\, d\mathbf{n} = 0 \tag{3.5}$$

where $\mathbf{w}$ is the velocity of each point of the boundary of the cell and $\mathbf{n}$ is the outward normal of the cell surface.

Voronoi cells are polyhedra (polygons in 2D) with $A_{ij}$ denoting the area of the face between cells $i$ and $j$. Equation 3.5 is discretized as follows:

$$\mathbf{Q}_i^{(n+1)} = \mathbf{Q}_i^{(n)} - \Delta t \sum_j A_{ij} \hat{\mathbf{F}}_{ij}^{n+1/2} = 0 \tag{3.6}$$

where $\mathbf{Q}_i^{(n)}$ is the state of the cell at timestep $n$, $\Delta t$ is the timestep that evolves the system to the next point in time, and $\hat{\mathbf{F}}_{ij}^{n+1/2}$ is a time-averaged approximation to the flux through the cell over the duration of the timestep. $\hat{\mathbf{F}}_{ij}$ is anti-symmetric, making the method conservative. All that remains to update mass, density, and energy is to find an appropriate second-order estimate of the numerical flux $\hat{\mathbf{F}}_{ij}$, which we describe next.

The flux computation for the mass, momentum, and energy for the moving mesh algorithm is calculated in the rest-frame of each of the faces. An important difference with the approach taken in Springel (2010) is that we first move the mesh generating points over a time interval $\Delta t$ according to their velocities, reconstruct the Voronoi mesh (this is the mesh at the end of the timestep), and then extrapolate fluid quantities to the face centroid of the mesh using the geometry at the end of the timestep rather than the beginning of the timestep for the flux computations. Using the cell geometry at the end of the timestep rather than at the beginning is an equally accurate reconstruction technique, but it turns out to be easier to account for changes in mesh connectivity for the CT algorithm for divergence-free evolution of magnetic fields, described in Section 3.2.3.

In the scheme, the primitive variables of each cell are estimated from the conserved variables and used to determine the wave-speeds local to the cell and the timesteps. The Courant-Friedrichs-Levy (CFL) timestep criterion is used to set the timestep:

$$\Delta t_i = C_{\mathrm{CFL}} \frac{R_i}{c_{\mathrm{f},i} + |\mathbf{v}_i - \mathbf{w}_i|} \tag{3.7}$$

where we choose $C_{\mathrm{CFL}} \lesssim 0.4$ for stable evolution of the MHD equations on a moving mesh. Here, $c_{\mathrm{f},i}$ is the fast magnetosonic sound-speed in cell $i$.

The mesh is then evolved to the geometry of the next timestep. The mesh-generating points move closely with the fluid flow with some small regularization corrections to keep the cells 'round'. The cell velocity $\mathbf{w}_i$ of each cell $i$ is calculated at the beginning of each timestep as:

$$\mathbf{w}_i = \mathbf{v}_i + \chi \begin{cases} 0, & d_i/(\eta R_i) < 0.9 \\ c_i \frac{\mathbf{s}_i - \mathbf{r}_i}{d_i} \frac{d_i - 0.9\eta R_i}{0.2\eta R_i}, & 0.9 \leq d_i/(\eta R_i) < 1.1 \\ c_i \frac{\mathbf{s}_\mathrm{i} - \mathbf{r}_i}{d_i}, & 1.1 \leq d_i/(\eta R_i) \end{cases} \tag{3.8}$$

where $R_i$ is the effective radius of a cell (calculated from the volume), $c_i$ is the local sound-speed of the cell, and $d_i = |\mathbf{r}_i - \mathbf{s}_i|$ is the distance between the cell's mesh generating point and its centre of mass. The quantities $\eta$, and $\chi$ are free parameters defining how aggressively to apply mesh regularization. For our simulations, we use $\eta = 0.05$, $\chi = 1.0$. The full geometry of the Voronoi mesh is then calculated from the positions of the mesh generating points.

The primitive variables are re-estimated once the mesh is moved from the conserved variables. This makes the reconstruction step fully conservative.

To obtain second-order accurate estimates of the flux, we estimate gradients of the primitive fluid variables ($\rho$, $\mathbf{v}$, $p_{\mathrm{gas}}$, $\mathbf{B}$) in each cell. We use Equation 22 of Springel (2010), namely, the gradient in cell $i$ of a primitive fluid variable $\phi$ is given by:

$$\langle \phi \rangle_i = \frac{1}{V_i} \sum_{j \neq i} A_{ij} \left( [\phi_j - \phi_i] \frac{\mathbf{c}_{ij}}{r_{ij}} - \frac{\phi_i + \phi_j}{2} \frac{\mathbf{r}_{ij}}{r_{ij}} \right) \tag{3.9}$$

where $\mathbf{r}_{ij} = \mathbf{r}_i - \mathbf{r}_j$ with $\mathbf{r}_i$ being the mesh generating point of cell $i$, and $\mathbf{c}_{ij}$ is the vector from the midpoint between $i$ and $j$ to the centre-of-mass of the face between $i$ and $j$.

Now, discontinuities in the fluid variables due, for example, to the presence of shocks, may cause spurious oscillations in the solutions. To suppress these, we are required to limit the gradients of the fluid variables, using the rule that linearly reconstructed quantities on face centroids may not exceed the maxima or minima among all cell neighbours. The slope limiting rule is expressed in mathematical terms as:

$$\langle \nabla \phi \rangle_i' = \alpha_i \langle \nabla \phi \rangle_i \tag{3.10}$$

where $0 \leq \alpha_i \leq 1$ is the slope limiter computed as:

$$\alpha_i = \min(1, \psi_{ij}) \tag{3.11}$$

with the minimum being taken over all neighbouring cells $j$ of cell $i$, with $\psi_{ij}$ defined as:

$$\phi_{ij} = \begin{cases} (\phi_i^{\max} - \phi_i)/\Delta\phi_{ij}, & \Delta\phi_{ij} > 0 \\ (\phi_i^{\min} - \phi_i)/\Delta\phi_{ij}, & \Delta\phi_{ij} < 0 \\ 1, & \Delta\phi_{ij} = 0 \end{cases} \tag{3.12}$$

where $\nabla\phi_{ij} = \langle\phi\rangle_i \cdot (\mathbf{f}_{ij} - \mathbf{s}_i)$ is the estimated change between the centroid $\mathbf{f}_{ij}$ of the face and the centre-of-mass $\mathbf{s}_i$ of the cell $i$, and $\phi_i^{\max} = \max(\phi_j)$, $\phi_i^{\min} = \min(\phi_j)$ are the maximum/minimum values of $\phi$ among all neighbouring cells of cell $i$, including cell $i$.

Supposing we have neighbouring cells $i$ and $j$, the estimate of the face velocity $\mathbf{w}_{ij}$ can be computed as:

$$\mathbf{w}_{ij} = \frac{\mathbf{w}_i + \mathbf{w}_j}{2} + \frac{(\mathbf{w}_i - \mathbf{w}_j) \cdot [\mathbf{f}_{ij} - (\mathbf{r}_i + \mathbf{r}_j)/2]}{|\mathbf{r}_j - \mathbf{r}_i|} \cdot \frac{\mathbf{r}_j - \mathbf{r}_i}{|\mathbf{r}_j - \mathbf{r}_i|} \tag{3.13}$$

We then change the primitive variables $\mathbf{W}^T = (\rho, \mathbf{v}, p_{\text{gas}}, \mathbf{B})$ of cells $i$ and $j$ from the lab-frame to the rest-frame of the face:

$$\mathbf{W}'_{i,j} = \mathbf{W}_{i,j} - \begin{pmatrix} 0 \\ \mathbf{w}_{ij} \\ 0 \\ 0 \\ 0 \end{pmatrix} \tag{3.14}$$

We then linearly predict the states on both sides of the centroid of the face, also predicting them forward by half a timestep:

$$\mathbf{W}''_{i,j} = \mathbf{W}'_{i,j} + \left.\frac{\partial \mathbf{W}'}{\partial \mathbf{r}}\right|_{i,j} (\mathbf{f}_{ij} - \mathbf{s}_{i,j}) + \left.\frac{\partial \mathbf{W}'}{\partial t}\right|_{i,j} \frac{\Delta t}{2} \tag{3.15}$$

where the spatial derivatives $\frac{\partial \mathbf{W}'}{\partial \mathbf{r}}$ are the slope-limited gradients of the primitive fluid variables. Note again that we are extrapolating to the centroids of the cell faces of the mesh geometry at the end of the timestep in this step. The time derivatives $\frac{\partial \mathbf{W}'}{\partial t}$ can be obtained from the primitive form of the MHD equations:

$$\frac{\partial \mathbf{W}'}{\partial t} + \mathbf{A}(\mathbf{W}) \frac{\partial \mathbf{W}'}{\partial \mathbf{r}} = 0 \tag{3.16}$$

where

$$\mathbf{A}_x(\mathbf{W}) = \begin{pmatrix} v_x & \rho & 0 & 0 & 0 & 0 \\ 0 & v_x & 0 & 1/\rho & -B_x/\rho & B_y/\rho \\ 0 & 0 & v_x & 0 & -B_y/\rho & -B_x/\rho \\ 0 & \gamma p_{\text{gas}} & 0 & v_x & (\gamma-1)\mathbf{B}\cdot\mathbf{v} & 0 \\ 0 & 0 & 0 & 0 & 0 & 0 \\ 0 & B_y & -B_x & 0 & -v_y & v_x \end{pmatrix} \tag{3.17}$$

and

$$\mathbf{A}_y(\mathbf{W}) = \begin{pmatrix} v_y & 0 & \rho & 0 & 0 & 0 \\ 0 & v_y & 0 & 0 & -B_y/\rho & -B_x/\rho \\ 0 & 0 & v_y & 1/\rho & B_x/\rho & -B_y/\rho \\ 0 & 0 & \gamma p_{\text{gas}} & v_y & 0 & (\gamma-1)\mathbf{B}\cdot\mathbf{v} \\ 0 & -B_y & B_x & 0 & v_y & -v_x \\ 0 & 0 & 0 & 0 & 0 & 0 \end{pmatrix} \tag{3.18}$$

The state is rotated into a new coordinate frame such that the $x$-axis is parallel to the normal vector of the face, pointing from cell $i$ to cell $j$:

$$\mathbf{W}'''_{i,j} = \begin{pmatrix} 1 & 0 & 0 & 0 \\ 0 & \Lambda_{\text{2D}} & 0 & 0 \\ 0 & 0 & 1 & 0 \\ 0 & 0 & 0 & \Lambda_{\text{2D}} \end{pmatrix} \mathbf{W}''_{i,j} \tag{3.19}$$

where $\Lambda_{\text{2D}}$ rotates the velocity and magnetic field components appropriately. In this new frame, the normal components of the magnetic field are averaged to guarantee their continuity across the cell (which is required by the divergence-free condition of MHD for 1D):

$$B'''_{x,(i,j)} \leftarrow \frac{B'''_{x,i} + B'''_{x,j}}{2} \tag{3.20}$$

At the interface between the two cells, we now must approximately solve the Riemann problem to obtain the flux. The primitive variables $\mathbf{W}'''_{i,j}$ are converted to conservative variables $\mathbf{U}'''_{i,j}$, and the HLLD flux (Miyoshi & Kusano 2005) is computed:

$$\mathbf{F}'''_{ij} = \mathcal{F}_{\mathrm{HLLD}}(\mathbf{U}'''_i, \mathbf{U}'''_j) \tag{3.21}$$

The HLLD flux is a highly-accurate, widely used, Riemann solver for the MHD equations which approximates the Riemann fan by 5 waves. In some instances, the solver may result in an unphysical negative pressure, in which case the Riemann solver defaults to calculating the Rusanov flux (also called local Lax-Friedrichs flux) which is more diffusive but always stable.

De-rotation is then used to obtain the fluxes in the rest-frame of the face but the $x$ and $y$ axes restored to their directions in the lab frame:

$$\mathbf{F}''_{ij} = \begin{pmatrix} 1 & 0 & 0 & 0 \\ 0 & \Lambda_{\mathrm{2D}}^{-1} & 0 & 0 \\ 0 & 0 & 1 & 0 \\ 0 & 0 & 0 & \Lambda_{\mathrm{2D}}^{-1} \end{pmatrix} \mathbf{F}'''_{ij} \tag{3.22}$$

where we will introduce notation for the components of this flux: $\mathbf{F}''_{ij} = (F_1, F_2, F_3, F_4, F_5, F_6)^T$. We can now obtain the numerical flux required to update Equation 3.6 from the flux in the rest frame of the face with a correction term for the movement of the face which retains an upwind character, derived in Pakmor et al. (2011):

$$\hat{\mathbf{F}}_{ij}^{n+1/2} = \mathbf{F}''_{ij} + \left( \begin{array}{c} 0 \\ w_{x,ij} F_1 \\ w_{y,ij} F_1 \\ w_{x,ij} F_2 + w_{y,ij} F_3 + \frac{1}{2} F_1 \mathbf{w}_{ij}^2 \\ -w_{x,ij} B'''_{x,(i,j)} \\ -w_{y,ij} B'''_{x,(i,j)} \end{array} \right) \tag{3.23}$$

### 3.2.3 CONSTRAINED TRANSPORT ON A MOVING MESH

The CT algorithm relies on evolving the average normal component of the flux of the magnetic field through each face of each cell using Faraday's induction equation:

$$\frac{\partial \mathbf{B}}{\partial t} + \nabla \times \mathbf{E} = 0 \tag{3.24}$$

where $\mathbf{E} = -\mathbf{v} \times \mathbf{B}$ is the electric field. The normal component of the magnetic flux through some face $A$ is defined as:

$$\Phi = \int_A \mathbf{B} \cdot d\mathbf{A} \tag{3.25}$$

Suppose that the surface $A = A(t)$ moves in time. Rewriting Equation 3.24 in integral form and applying Stokes' theorem yields:

$$\frac{d\Phi}{dt} + \int_{\partial A(t)} (\mathbf{E} + \mathbf{w} \times \mathbf{B}) \cdot d\ell = 0 \tag{3.26}$$

where $\mathbf{w}$ is the velocity of the motion of the surface, which can be rewritten as:

$$\frac{d\Phi}{dt} - \int_{\partial A(t)} ((\mathbf{v} - \mathbf{w}) \times \mathbf{B}) \cdot d\ell = 0 \tag{3.27}$$

We see that $-(\mathbf{v} - \mathbf{w}) \times \mathbf{B}$ is just the electric field in the rest frame of a point on the boundary of the surface.

Let $\Phi_{ij}$ be the outward normal magnetic flux from cell $i$ through the face between cell $i$ and cell $j$. Then, the average magnetic field outward normal to the surface is $B_{ij} = \Phi_{ij}/A_{ij}$. Equation 3.27 may then be discretized as follows:

$$\Phi_{ij}^{(n+1)} = \Phi_{ij}^{(n)} - \Delta t(E_{L,ij}^{(n+1/2)} - E_{R,ij}^{(n+1/2)}) \tag{3.28}$$

where $E_{L,ij}^{(n+1/2)}$ and $E_{R,ij}^{(n+1/2)}$ are estimates for the $z$-component of the electric fields at the two edges ($e_{L,ij}$ and $e_{R,ij}$) of the face in the middle of the timestep. The points $r_i$ (the mesh generating point), $e_{R,ij}$, $e_{L,ij}$ are oriented counter-clockwise.

The divergence of $\mathbf{B}$ can be estimated using Stokes' theorem as:

$$\nabla \cdot \mathbf{B}_i = \frac{1}{V_i} \sum_j \Phi_{ij} \tag{3.29}$$

which is kept zero at the level of machine precision as long as the initial conditions have zero divergence, due to the opposite signs of $E^{(n+1/2)}_{L,ij}$ and $E^{(n+1/2)}_{R,ij}$ and the exact cancellation that is obtained in looping around the border of the cell and summing the changes to the fluxes through the faces. Note that the CT approach only keeps this one particular discretization of the divergence to zero to machine precision.

One now just needs to accurately estimate $E^{(n+1/2)}$ to be able to update the magnetic flux. We do so using a flux-interpolated approach as follows. In this Section we will assume that the mesh connectivity does not change between timesteps, and in Section 3.2.3 we describe the additional remapping technique that needs to be applied on magnetic fluxes through faces whenever the mesh connectivity changes between timesteps (which corresponds to the appearance and disappearance of faces).

We define a map from the magnetic field fluxes through the faces of a cell and the magnetic field at the centre of the cell $\mathbf{B}_i$ by solving the linear least-squares problem:

$$\begin{pmatrix} w_{ij_1} n_{x,ij} & w_{ij_1} n_{y,ij} \\ \vdots & \vdots \\ w_{ij_n} n_{x,ij} & w_{ij_n} n_{y,ij} \end{pmatrix} \begin{pmatrix} B_{x,i} \\ B_{y,i} \end{pmatrix} = \begin{pmatrix} w_{ij_1} B_{ij_1} \\ \vdots \\ w_{ij_n} B_{ij_n} \end{pmatrix} \tag{3.30}$$

where the $j_1, \ldots, j_n$ are the neighbours of cell $i$, $\mathbf{n}_{ij}$ is the outward normal at the face, and $w_{ij}$ is a weight, where we use the reciprocal of the distance from the centre of mass of the cell to the centroid of the face between cell $i$ and cell $j$. This map is used to obtain the conservative variable$\int B\, dV_i$ of each cell at the beginning of the timestep. The choice of $w_{ij}$ is not unique. We adopt a form for $w_{ij}$ that minimizes the difference of the magnetic field on the face centroids compared to the volume average magnetic field, weighting closer faces as the inverse of the displacement (i.e., the error obtained by extending the cell-average value to the edges is assumed to be dominated by a first order term). One may choose to additionally multiply the weight by the area of faces, or the area of the triangle determined by the centre of mass and the face. We explored these alternate options and found that they made no significant difference for regularized meshes.

The mesh is moved its location at the end of the timestep, and gradient information for $\mathbf{B}$ is calculated, as in Section 3.2.2 for the other primitive variables. The normal component of the magnetic field across each face is obtained by averaging the two predictions obtained by extrapolating to the face from the cell centre of mass at either side of the face (Equation 3.20). The Riemann solver requires a constant magnetic field across the shock (which is a consequence of $\nabla \cdot \mathbf{B} = 0$ in 1D). Note that in the CT method the divergence of the magnetic field in a cell is not necessarily $0$ when we extrapolate to estimate the flux at the middle of the timestep, but at the end of the timestep it will always evolve to a state with the discretized divergence (equation 3.29) kept at zero to machine-precision.

The next step is to estimate the electric fields in the rest-frames of each edge. This is done by using the fluxes for the magnetic fields obtained from the Riemann solver and applying a correction to change the frame into the rest frame of the edge. There are multiple estimates for the electric field at each edge, obtained from using the flux of any of the faces that include that edge (3 faces in the case of a non-degenerate 2D Voronoi mesh). These estimates are averaged with barycentric weights of a triangle determined by the centroids of the faces. This choice of interpolation gives the best-possible accuracy for the case of smooth fields. One may design variants of this scheme in which the weights are adjusted in the vicinity of magnetosonic shocks to account for the upwind direction, as described in Balsara & Spicer (1999), although these modifications were not found to be necessary for our simulations (see discussions in Balsara & Spicer (1999) and Tóth (2000) for cases where this variant may be useful). The electric field estimate at an edge $e_{L,ij}$ obtained from the flux across cell $i$ and $j$ is calculated as:

$$\begin{aligned} E''_{L,ij} &= -(F_{6,ij}\hat{n}_{\perp,x,ij} - F_{5,ij}\hat{n}_{\perp,y,ij}) \\ &\quad +(v_{x,L,ij} - w_{x,ij})B_{y,ij} \\ &\quad -(v_{y,L,ij} - w_{y,ij})B_{x,ij} \end{aligned} \tag{3.31}$$

where $F_{5,ij}$ and $F_{6,ij}$ are the magnetic field fluxes of the Riemann solver in the rest-frame of the faces, $\hat{\mathbf{n}}_{\perp,ij}$ is the outward normal of the face between cells $i$ and $j$, pointing towards $j$, $\mathbf{v}_{L,ij}$ is the edge velocity, calculated exactly from the mesh geometry, and $\mathbf{B}_{ij}$ is the magnetic field (in the lab frame) returned by the 1D Riemann solver sampled at $x = 0$.

An alternate approach to the above is to use a field-interpolated approach; i.e., to extrapolate the magnetic and velocity fields to each edge of each face in the rest-frame of the edge.

However, flux-interpolated approaches have slightly better performance and desirable properties due to the consistency of coupling the electric field estimate to the Riemann solver (Tóth 2000). Equation 3.31, without the last two terms that account for the change of frame, is the familiar way to estimate the electric field in flux-interpolated CT schemes on fixed grids (see, e.g. Balsara & Spicer (1999)).

The above describes the basics of a CT algorithm for moving unstructured meshes, which preserves $\nabla \cdot \mathbf{B} = 0$. It is important that the initial conditions must be set so that $\nabla \cdot \mathbf{B} = 0$ at the beginning. This is accomplished using the vector potential $\mathbf{A}$, evaluating it on the face edges, and using $\mathbf{B} = \nabla \times \mathbf{A}$ to obtain the face-centred magnetic fields, which is the usual strategy taken by CT algorithms on fixed grids. In particular, in our 2D simulations we set the magnetic flux on each of the faces to be:

$$\Phi_{ij} = A_z(e_{L,ij}) - A_z(e_{R,ij}) \tag{3.32}$$

If the divergence error is not set to zero in the initial conditions, the scheme will preserve any glitch in the initial conditions (effectively conserving a magnetic monopole).

### REMAPPING

During one timestep to the next, the moving Voronoi tessellation may change connectivity, resulting in faces appearing and disappearing. A face that appears at the end of a timestep poses no large issue for preserving $\nabla \cdot \mathbf{B} = 0$ because it can be treated as coming from a degenerate face of area and magnetic flux $0$ during the previous step. The nice cancellation property of the update terms for the magnetic fluxes of the faces of a cell in the calculation of the divergence still holds. A bigger concern is the disappearance of a face. In the continuous limit, the flux through the face should go to $0$ as the face disappears, since its area goes to zero. But in our discretization, a vanishing face would have some small amount of residual flux that would not be properly accounted after the face disappears in the next timestep, and this would result in a breakdown of the CT method. However, this issue can be redressed by using a remapping technique, described here.

The approach taken in this work is to remap the geometry slightly at the beginning of each timestep in the cases where mesh connectivity changes. A face that is identified to disappear is mapped to a degenerate point at the centroid of the face (i.e., one can think of shrinking the face to a degenerate point at the centroid and remapping the magnetic fluxes through the faces). The remapping is illustrated in Figure 3.2. The vanishing face touches two cells. For each touching cell, the flux through the vanishing face is equally distributed to the two faces that touch this face. This technique preserves $\nabla \cdot \mathbf{B} = 0$ exactly to machine-precision. The method does require that the connectivity between time-steps does not change drastically; that is, if a face disappears then its surrounding neighbouring faces are not allowed to change connectivity. This is always possible in the limit of small timesteps since the Voronoi mesh evolves continuously. After each timestep, we are required to check that the connectivity has not changed too drastically, and if it did, then the current timestep is halved until the mesh evolves in a satisfactory way. This is typically a rare occurrence in our test problems

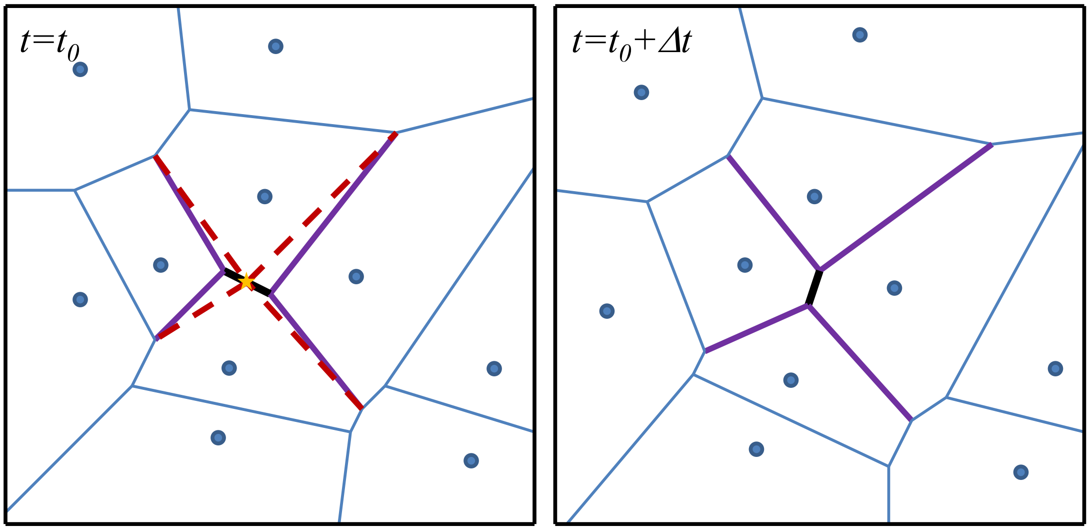

**Figure 3.2:** During one timestep (left) and the next (right), the connectivity between cells in the moving Voronoi mesh may change. In such a case, a face disappears (thick black line). The geometry at the beginning of the timestep is remapped by adding a degenerate vertex (yellow star) at the midpoint of the face that is to disappear and connecting the surrounding faces (red-dashed lines) to it. The magnetic flux through the vanishing face is redistributed to the faces shown in red-dashed lines. The connectivity of the mesh is not permitted to change too drastically from one time-step to the next: if a face disappears, there must be remaining neighbouring faces that do not change connectivity to which the flux is redistributed. Voronoi diagrams change continuously, so drastic changes can always be avoided by taking the timestep small enough.

because the CFL condition does limit the size of the timestep and typically $0$ or $1$ faces appear/disappear in a cell. But more sophisticated techniques can be employed to improve the efficiency of the algorithm and avoid this halving of timesteps (see Section 3.4.2).

### EXTENSION TO 3D

The method described here is generalizable to three dimensions. In the 3D case, the boundaries of a face are a polygon rather than two points. Thus when updating the magnetic fluxes one needs to perform a loop integral over the boundary, just as in the regular CT method. The key difference is to estimate the electric fields in the rest frames of the centroid of each linear segment of the loop. An edge at the end of the timestep may not have been present at the beginning of the timestep, in which case in order to estimate its velocity it can be considered as a ‘degenerate face’ (a single point) in the previous Voronoi tessellation. In the remapping step, the magnetic flux through a face that disappears may be equally redistributed to all the faces that touch the vanishing face, and the face that disappears is shrunk down to its centroid.

In short, the key ideas necessary for extending CT to an arbitrary moving mesh are to always calculate electric fields in the moving frame of the edge and to remap the magnetic fluxes of faces that disappear to the neighbouring faces.

## 3.3 NUMERICAL TESTS

### 3.3.1 ORSZAG-TANG VORTEX

We demonstrate that our numerical method works successfully by solving the Orszag-Tang vortex problem (Orszag & Tang 1979), which is an excellent test of supersonic MHD turbulence and generally one of the more difficult tests for MHD solvers to handle. We use the initial conditions as described by Picone & Dahlburg (1991):

$$\rho = \frac{\gamma^2}{4\pi}, \tag{3.33}$$

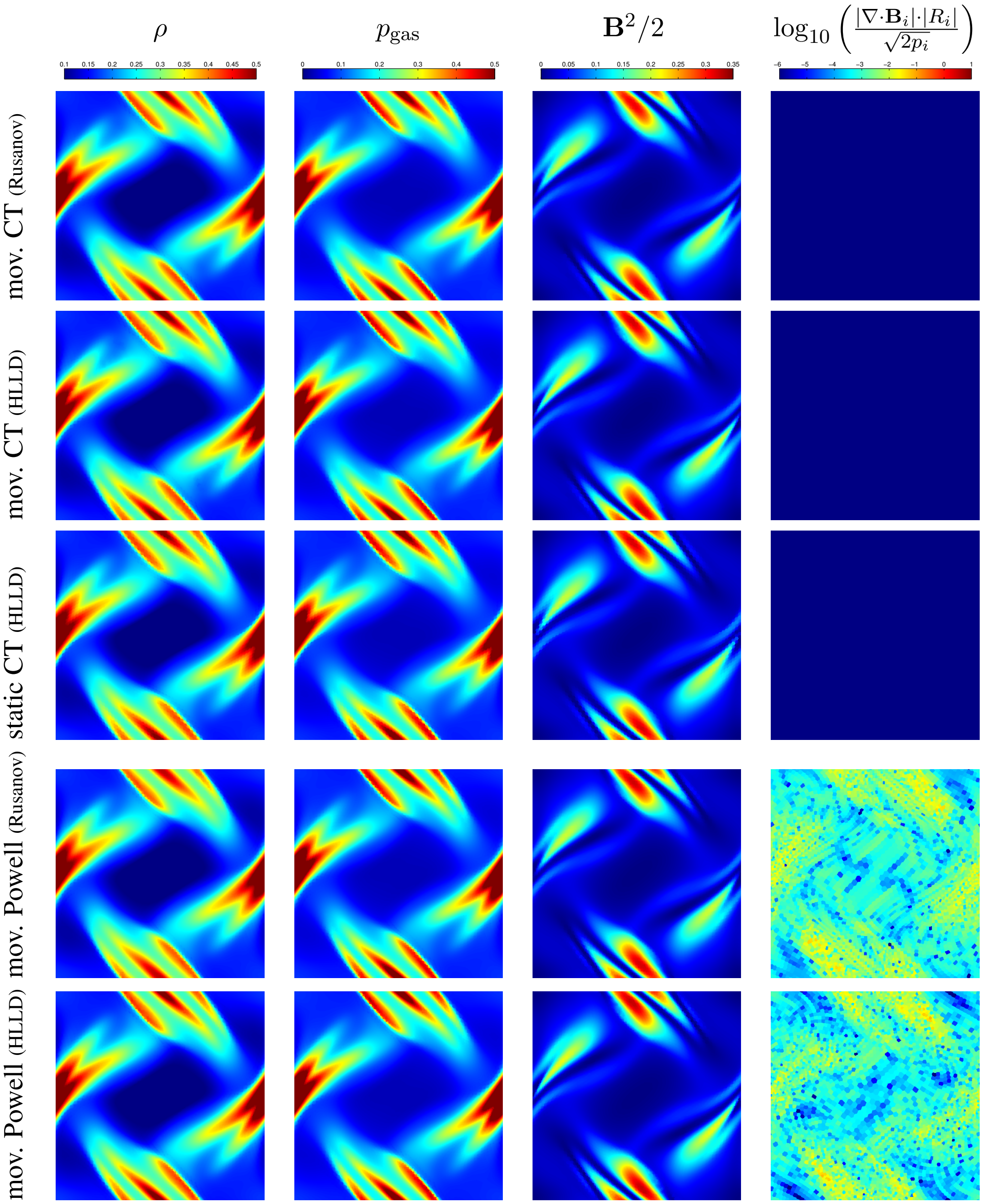

**Figure 3.3:** A comparison of various numerical methods used to evolve the Orszag-Tang test at $t = 0.2$. Shown are the moving CT method (with Rusanov and HLLD flux solvers), the static CT method (on a hexagonal grid with an HLLD solver), and the moving Powell method (with Rusanov and HLLD flux solvers). Plotted are the density, pressure, magnetic energy density, and relative divergence error of the magnetic fields (compared to fluid pressure). For the CT schemes, the divergence errors are of the order of machine precision $\sim 10^{-15}$, so they are much smaller than the minimum colour value indicated ($10^{-6}$) by the colour bar.

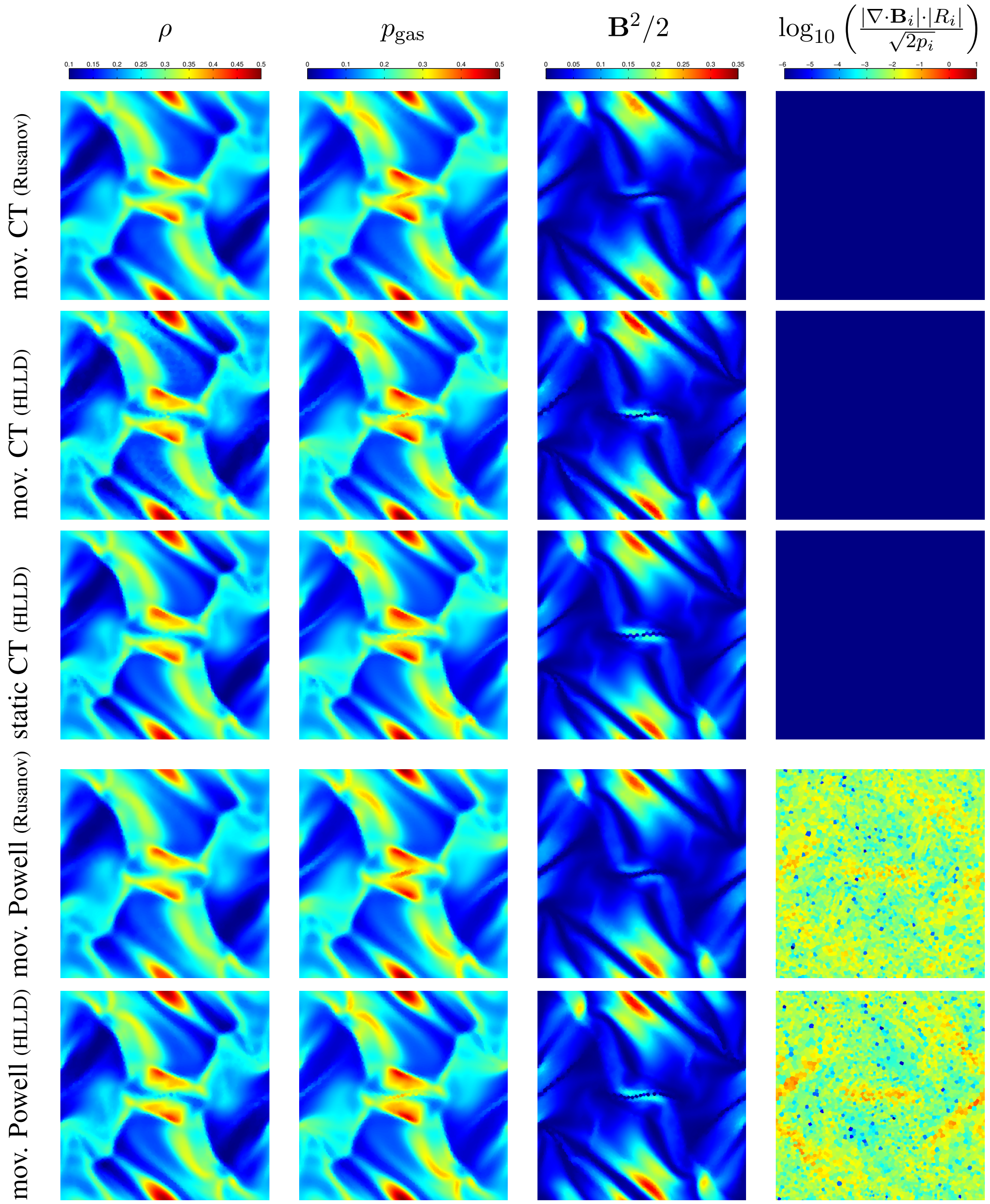

**Figure 3.4:** Same as Figure 3.3, except at $t = 0.5$.

$$p = \frac{\gamma}{4\pi}, \tag{3.34}$$

$$\mathbf{v} = (-\sin(2\pi y), \sin(2\pi x)), \tag{3.35}$$

$$\mathbf{B} = (-\sin(2\pi y), \sin(4\pi x)). \tag{3.36}$$

The domain is a box of side length $1$ with periodic boundaries. The gas has adiabatic index $\gamma = 5/3$.

We show the results of the moving CT method at resolution $64^2$, and compare it with a static CT approach on a hexagonal grid, and the moving Powell cleaning scheme. Plots of the density and magnetic energy density are shown in Figures 3.3 and 3.4[*]. All the methods produce qualitatively similar results. Figure 3.5 shows that the moving CT method converges to the solution of a high resolution ($512^2$) static CT technique at the same rate as the static CT method (first order convergence is observed due to the presence of shocks, which results in gradients that are slope-limited). The errors in the moving CT method are slightly less than the static CT approach, which can be attributed to the moving method's better control of advection.

We quantify the strength of the magnetic field divergence error in two ways. First, is the

---

[*] animations of the simulations are available at https://www.cfa.harvard.edu/~pmocz/research.html

relative divergence error compared to the magnetic field of the cell, used in Duffell & MacFadyen (2011); Pakmor et al. (2011); Gaburov et al. (2012); Pakmor & Springel (2013). This is calculated for each cell $i$ as:

$$\frac{|\nabla \cdot \mathbf{B}_i| \cdot |R_i|}{|\mathbf{B}_i|} \tag{3.37}$$

However, an alternate measure is to normalize by an "effective" magnetic field quantity, namely, the square root of twice the total pressure, as follows:

$$\frac{|\nabla \cdot \mathbf{B}_i| \cdot |R_i|}{\sqrt{2p_i}} \tag{3.38}$$

This arguably provides a better indication of when the divergence error becomes dynamically important, since by the first measure the error can be large in the case when the magnetic fields are small but it is likely that the largest errors in the dynamics are incurred at those points. The second diagnostic also includes the importance of gas pressure in the normalization. We plot this second measure of divergence in Figures 3.3 and 3.4 for the Orszag-Tang test. As expected, the CT algorithms show no error.

It is worth pointing out that the moving CT scheme that uses the HLLD solver produces less smooth solutions at late times once strong shocks break out in the simulation ($t = 0.5$, see Figure 3.4) in the density field (but not any of the other fluid variable fields) compared to the other methods. This is attributable to the moving mesh nature of the code and using an approximate Riemann solver: small errors in the density field advect with the flow and do not diffuse. More diffusive approaches, such as using a Rusanov flux solver, or a Powell cleaning scheme with HLLD, or a static CT HLLD solver, produce a smoother density field.

We verify that the average relative magnetic field divergence errors of a cell are zero to the level of machine precision in Figure 3.6. The average relative divergence errors of a moving mesh approach with the Powell cleaning scheme is on the order of $10^{-3}$, and a few individual cells can have errors greater than order unity.

### GALILEAN INVARIANCE

We demonstrate that our method is less susceptible to being dominated by truncation errors under a Galilean boost than static mesh approaches. Our technique also requires less strict timestep criteria, due to the Lagrangian nature of our method (fluxes are always solved in the rest frames of faces/edges). We boost the $x$-direction velocities in the initial conditions of the Orszag-Tang test by a velocity of $10$ (corresponding to a Mach number of $10$), and compare the moving and static CT approaches at $t = 0.5$. The results are shown in Figure 3.7. The moving mesh approach maintains symmetry to a greater degree and has less diffusion (in the static CT approach, the overdense regions near at $x = 0.5$, $y = 0.1, 0.9$ are diffused when the Galilean boost is applied). Such unwanted numerical artefacts could lead to potential inaccuracies in, for example, the study of density distribution functions to understand supersonic turbulence and the collapse of high density material in the formation of stars. We note that the errors in the fixed grid CT approach can be reduced with sufficiently high resolution, however, this may not always be attainable with limitations on computational performance. We also

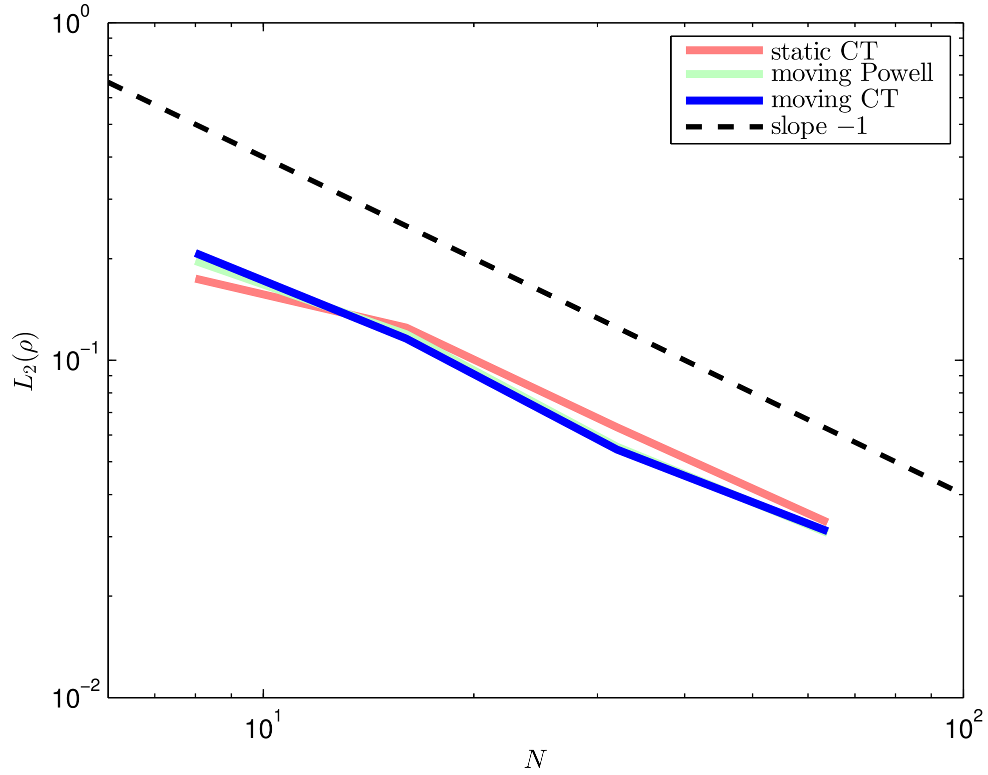

**Figure 3.5:** The convergence rate of the moving and static mesh CT methods and the moving Powell method for the Orszag-Tang test at $t = 0.2$. Both show first order convergence, as expected due to the presence of shocks which limits some of the slopes and reduces the second order method to first order. The moving mesh approach shows slightly smaller errors.

show the results of the moving Powell scheme, whose solution is also largely unaffected by the velocity boost, due to its Lagrangian nature (although, as we show in § 3.3.2, the Powell scheme loses some of its Galilean-invariant properties due to its source terms).

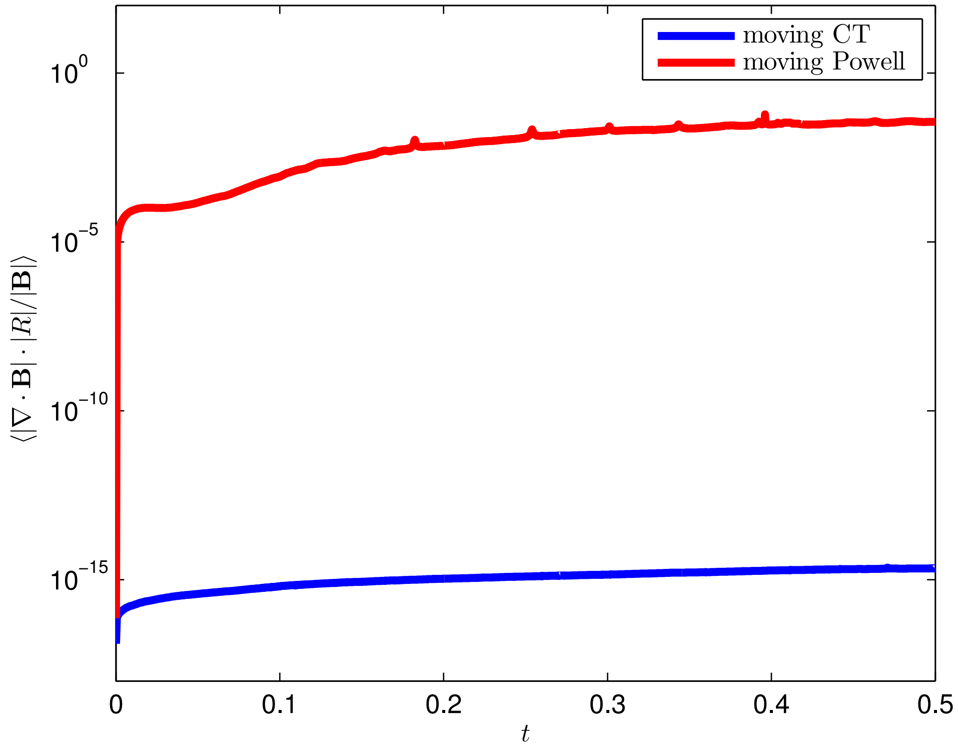

**Figure 3.6:** The average relative magnetic field divergence errors in the moving CT approach are kept to $0$ at the level of machine precision, while the Powell cleaning scheme shows an average error of $10^{-3}$ for the Orszag-Tang test. The Powell cleaning scheme may even demonstrate relative errors of the order of unity in a few individual cells at a given time (Figure 3.4).

### 3.3.2 ADVECTION OF A MAGNETIC LOOP

The advection of a magnetic field loop is a common and important test of an MHD solver's ability to maintain the divergence of $\mathbf{B}$ and also demonstrates the scheme's diffusivity. It is often used as one of a series of tests to validate a numerical technique (Stone et al. 2008; Duffell & MacFadyen 2011), and many MHD solving techniques face difficulty when evolving this simple setup. In this test problem, a magnetic field loop with dynamically unimportant magnetic fields is advected by a constant velocity field. We simulate the advection in a periodic box of size $1$, adiabatic index $\gamma = 5/3$, and initial conditions given by:

$$\rho = 1 \tag{3.39}$$

$$p = 1 \tag{3.40}$$

$$\mathbf{v} = (\sin(\pi/3), \cos(\pi/3), 0) \tag{3.41}$$

$$\mathbf{A} = (0, \max(0.001 \cdot (0.3 - r), 0)) \tag{3.42}$$

where $r$ is the radial distance to the centre of the loop and $\mathbf{A}$ is the vector potential of the magnetic field.

We compare the moving CT method to a fixed grid flux-interpolated CT method and the moving Powell method. For the moving mesh, we use a hexagonal grid of resolution $64^2$ and for the fixed grid we use a Cartesian grid with resolution of $64^2$. A plot of the evolution of the average magnetic energy density $\frac{1}{2}\mathbf{B}^2$ is shown in Figure 3.8, along with the magnetic energy density at time $t = 2.2$. The moving mesh CT approach does incredibly well. It preserves the advection of the solution to machine precision, due to its Lagrangian properties. The magnetic energy density does not decay at all with time but rather stays constant. This is independent of the resolution used to simulate the advecting loop. In comparison, the fixed grid approach shows diffusivity and unphysical structures and asymmetries develop in the energy density. The magnetic energy density decays with time. These errors can be lessened by increasing the resolution of the run, but never fully eliminated in the fixed grid approach. The moving Powell cleaning scheme also shows diffusivity since it is not fully Galilean-invariant due to the addition of source terms. It does, however, maintain symmetry since the problem is solved in the rest frame of the motion of the loop.

### 3.3.3 STRONG SHOCK

We simulate a 1D strong MHD shock on a 2D domain. The initial left state is $(\rho, v_{||}, v_{\perp}, p, B_{||}, B_{\perp}) = (1, 10, 0, 20, 5/\sqrt{4\pi}, 5/\sqrt{4\pi})$ and the initial right state is $(\rho, v_{||}, v_{\perp}, p, B_{||}, B_{\perp}) = (1, -10, 0, 1, 5/\sqrt{4\pi}, 5/\sqrt{4\pi})$ for this Riemann problem, with adiabatic index $\gamma = 5/3$, and is found in Tóth (2000). The shock is set up to travel at an angle 30° with respect to a line of symmetry of the mesh. This Riemann problem has the exact solution where $B_{||}$ stays constant throughout the different

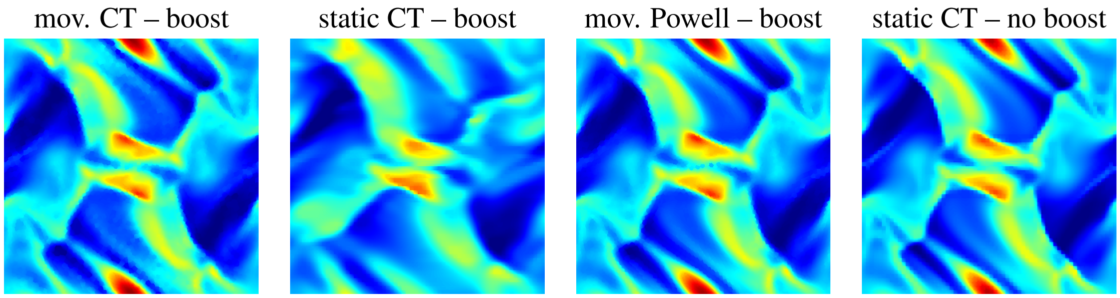

**Figure 3.7:** The density field of the Orszag-Tang test at $t = 0.5$ with initial conditions boosted by a Mach number of $10$ solved using the moving CT approach (left), the fixed grid CT approach (second from left), and the moving Powell cleaning scheme (third from left), compared to the solution obtained with a fixed grid CT solver and no boost in the initial conditions (right). The moving mesh approach shows less diffusion and more symmetry with the boost applied than the fixed grid approach, due to its Lagrangian nature.

shock regions during the evolution of the shock.

The shock is simulated with the moving CT, static CT, and moving Powell approaches, and the results of the evolved parallel component of the magnetic field are shown in Figure 3.9, for resolutions of $64$ and $256$ cells along the direction of the shock in a domain of length $1$. The results show that the non-conservative Powell approach performs the worst, producing incorrect jump conditions across discontinuities due to the cleaning source-terms. The depth of the deviations from the exact solution does not disappear with increased resolution. The CT schemes do much better. They also have errors across discontinuities, but they are smaller and oscillate around the exact solution, and therefore can be more reliably used to simulate strong shocks.

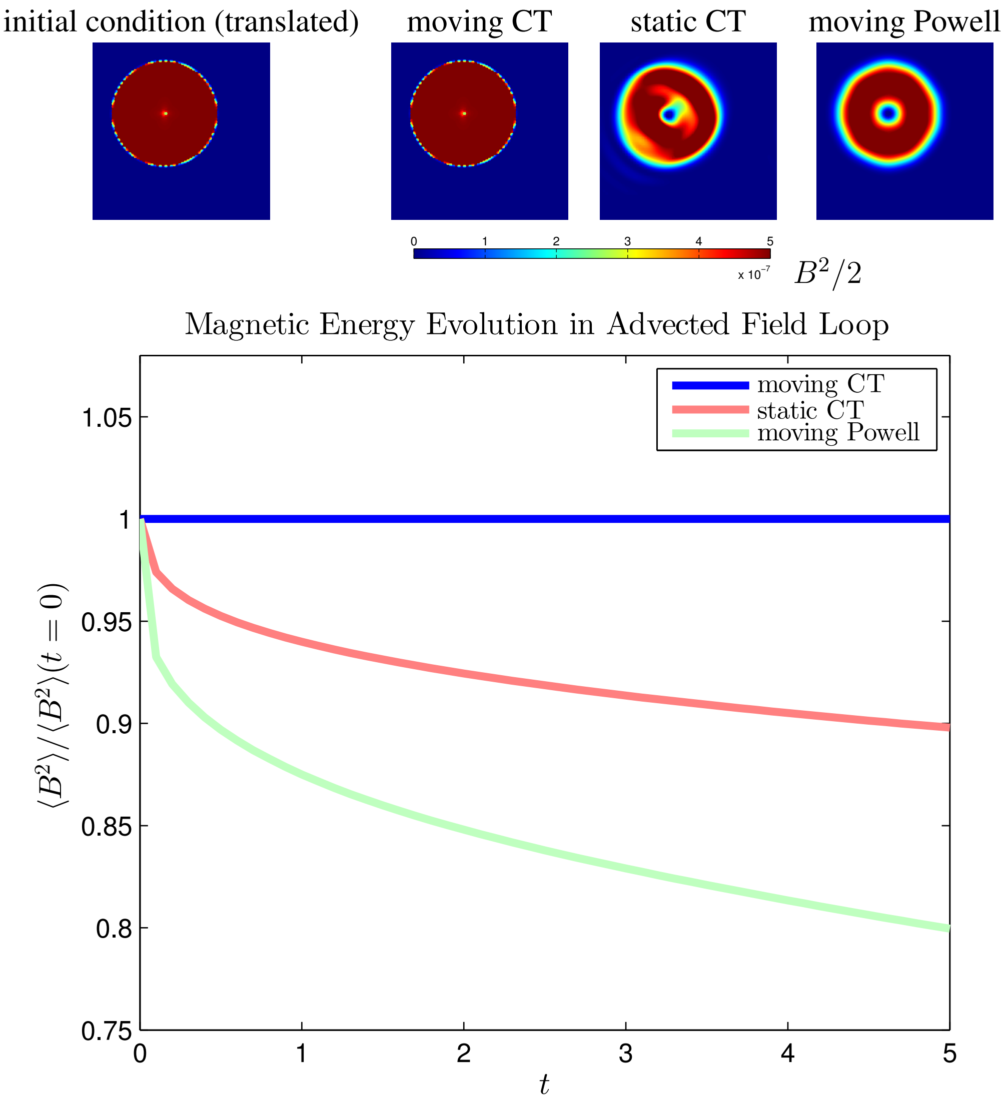

**Figure 3.8:** Plots of the magnetic energy density in the advection of a field loop test at the initial condition $t = 0$ (top left) and the advected solution at $t = 2.2$ for a moving CT approach (top right), a static CT approach (bottom left) and a moving Powell approach (bottom right). The moving CT approach advects the initial conditions to machine precision. The fixed grid CT approach on the other hand shows diffusion and develops asymmetries and unphysical structures. The moving Powell scheme also shows diffusivity due to the presence of source terms. The average magnetic energy density stays constant in the moving CT approach (agreeing with the exact solution) while it decays with the static CT and moving Powell approaches (bottom).

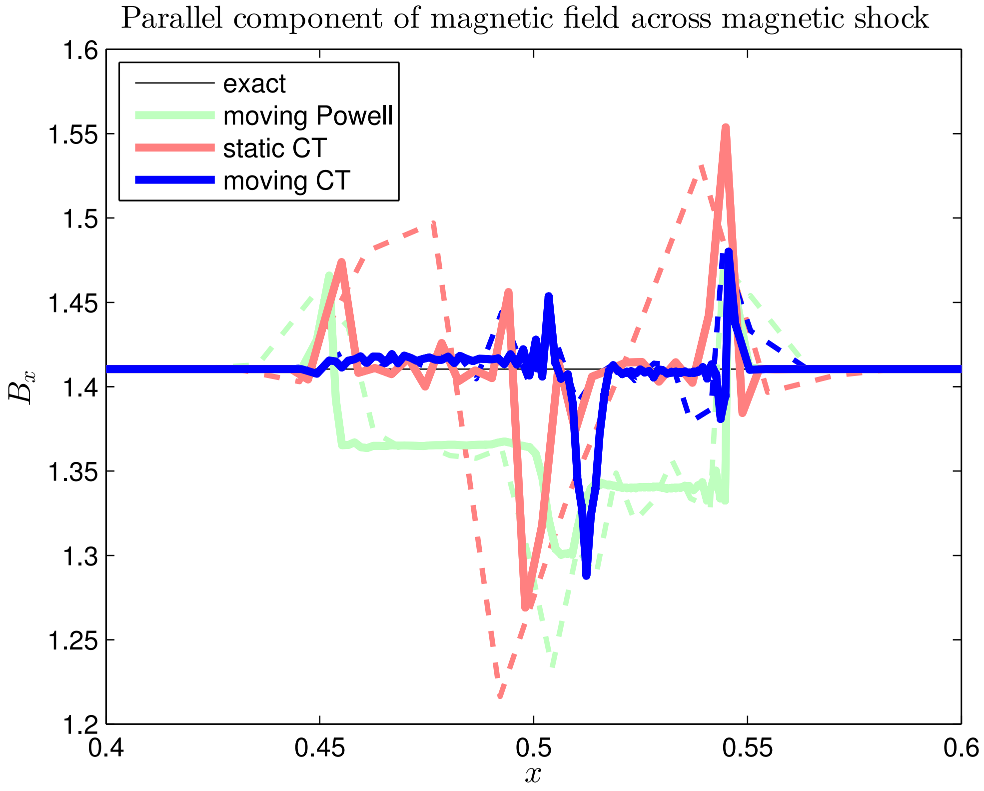

**Figure 3.9:** The parallel component of the magnetic field across the shock for our moving CT, static CT, and moving Powell schemes at $t = 0.01$. Thick solid and thin dashed lines correspond to resolutions of $256$ and $64$ respectively. Both CT approaches recover the exact solution with some spiked error at the discontinuity, as well as some oscillating errors in the rest of the domain which can be reduced with increased resolution. The moving Powell approach, however, produces incorrect jump conditions due to its non-conservative formulation, which expand with the shock and do not disappear with increased resolution.

## 3.4 DISCUSSION

### 3.4.1 IMPORTANCE OF $\nabla \cdot \mathbf{B} = 0$

A divergence-free (solenoidal) magnetic field means that there are no field lines that meet at monopolar singularities. By Stokes' theorem, there is no net magnetic flux out of any enclosed surface. The use of Stokes' theorem to rewrite the $\nabla \cdot \mathbf{B} = 0$ condition is the key to CT. Numerical methods which do not ensure the divergence of $B$ is kept small violate these properties which can lead to errors in the flow or even severe numerical instabilities in the solution. A plain finite volume scheme for the MHD equation can be unstable. Cleaning schemes do keep the divergence small enough so that the methods remain stable (at the cost of conserving the fluid variables, which may lead to convergence to the wrong answer). CT schemes offer a better discretization than finite volume approaches that maintains $\nabla \cdot \mathbf{B} = 0$ without any modification to the MHD equations or loss of conservation.

If $\nabla \cdot \mathbf{B} = 0$ is not preserved, one effectively litters the computational domain with magnetic monopole numerical artefacts. The Lorentz force no longer remains orthogonal to the magnetic field. To see this, consider the terms in the momentum equation in conservative form which arise from the magnetic field, which can be rewritten as:

$$\nabla \cdot \left( \frac{1}{2}\mathbf{B}^2 - \mathbf{B}\mathbf{B}^T \right) = -\left(\nabla \times \mathbf{B}\right) \times \mathbf{B} - \mathbf{B}\left(\nabla \cdot \mathbf{B}\right) \tag{3.43}$$

which reduces to the Lorentz force acting per unit volume only in the case that $\nabla \cdot \mathbf{B} = 0$. Any finite divergence in the discretized representation of the magnetic fields will bias the Lorentz force.

Large divergences in the magnetic fields make a simple MHD solver unstable, which is why CT or cleaning schemes need to be applied. Tóth (2000) carries out an extensive comparison of CT and divergence cleaning schemes on fixed grids. The largest problem identified with the Powell cleaning scheme is that the method is non-conservative, which may cause incorrect jump-conditions occasionally. CT schemes on the other hand are conservative, divergence-free, robust, and more accurate.

### 3.4.2 VARIATIONS AND EXTENSIONS OF THE METHOD

There are several ways to modify the CT scheme described above, which we sketch here. For example, the halving of the timestep in the cases where two or more neighbouring faces disappear in the same timestep may be avoided if one remaps all the edges of the connected disappearing faces to a single degenerate point and redistributes the fluxes of the vanishing faces to the neighbouring faces that do not disappear (this requires implementing a more involved remapping scheme). Alternatively, one could also invent a scheme where only faces that maintain connectivity throughout a timestep and share no edge with a face that disappears are updated at the end of the timestep, and a reconstruction scheme is used at the end of the timestep to create second-order estimates of the magnetic flux through faces that have appeared.

There are different ways one could obtain the estimate of the electric field at the edges of the cells. One could easily use a field-interpolated approach instead of the flux interpolated approach taken here.

The estimation of the cell-average magnetic fields from the face average fluxes is also free to be modified, and perhaps more accurate ones can be developed (our choice of mapping works well for regularized meshes). The gradient estimation of the magnetic fields in the reconstruction step may also be improved. For example, one may use some sort of local projection scheme on to a divergence-free basis.

Additionally, one could use a second-order accurate estimate for the velocity of the edges in the mesh that appear at the end of the timestep rather than calculating it exactly, which would mean that the geometrical information of the mesh at the beginning and end of the timestep would not have to be kept in memory at the same time.

We have highlighted some of the various modifications possible to the basic framework which can be explored in future work to optimize the moving mesh CT strategy. The goal of our current paper is to lay out the basic theoretical framework for the method. The basic strategy for maintaining $\nabla \cdot \mathbf{B} = 0$ is straightforward: update magnetic fluxes across face cells using any second order accurate of the electric field in the rest frames of the edges, and remap faces that disappear across a timestep by shrinking them to a degenerate point.

### ADAPTIVE TIMESTEPPING

Extending the moving CT method presented above to have adaptive timestepping through an efficient, local method is a goal for future research. We have not yet implemented such a scheme, but describe here general approaches and also additional challenges not found in the case of static meshes. An effective adaptive timestepping method for a moving mesh would likely use a power-of-two hierarchical time-binning procedure (Springel 2010), which accounts for Voronoi cells changing their volume throughout the simulation and maintains the stability and conservation-laws of the fluid solver. The basic idea is simple: place the cells in a nested hierarchy of cells with partial synchronization. Active cells in a timestep use their current fluid quantities in the interpolation step and inactive ones are simply advected and use their most recently calculated fluid quantities in the interpolation step so that the Riemann problem may be solved across the cells. The flux is always added to both cells to maintain the conserved quantities. So an inactive cell $i$ has flux added to it across faces shared with neighbouring cells in smaller timestep bins. Advecting inactive cells maintains self-consistency of the connectivity of the Voronoi diagram as it is reconstructed at various timestep hierarchy levels.

The idea can be extended to the moving CT approach. The electric fields at an edge need to be estimated at the smallest timestep that any of the faces that join the edge fall into. The change in magnetic flux: $\Delta t\, E$ (with the appropriate sign due to orientation) then needs to be applied to all the faces (including inactive ones) that join the electric field in order to maintain the divergence free condition. This idea works straightforwardly in the cases that no changes in mesh connectivity take place across timesteps, and even in the cases where all the cells which experience a change in connectivity fall into in the same timestep bin. However, special care has to be taken to resolve a change in connectivity that occurs between cells that fall into different timestep bins, since faces that are surrounded by inactive cells may appear and their magnetic flux through the face has to be accurately calculated and stored with the inactive cells, and additionally inactive cells may lose a face and thus a remap involving inactive cells is required. Thus each timestep bin would have to be adaptive to accommodate inactive cells that change the number of faces. Our current choice of using rare time-step halving in cases where the connectivity changes too much also complicates the issue, and thus a more involved remapper (Section 3.4.2) is preferred. The development of the details of an adaptive timestepping scheme is left for future work.

## 3.5 CONCLUDING REMARKS

We have presented a new, stable, accurate, and robust CT scheme for solving the MHD equations on a moving unstructured mesh which is conservative and preserves the divergence of the magnetic field to zero at the level of machine precision. Such a CT scheme for a moving mesh has been claimed to be difficult to construct, maybe even impossible, by other authors (Duffell & MacFadyen 2011; Pakmor et al. 2011; Pakmor & Springel 2013), but we have demonstrated that the scheme can be achieved. The CT method significantly improves the other current methods used to evolve the MHD equations on unstructured meshes and moving meshes, which are not necessarily conservative and can show large divergence errors and incorrect shock jump conditions. The new numerical method also has significant advantages over CT approaches on a fixed grid. Namely, our method is a quasi-Lagrangian scheme and greatly reduces advection errors. In pure advection flows, it preserves the solution at the level of machine-precision, which is a uniquely powerful feature of the method. Due to the moving mesh formulation, the method is also automatically adaptive in its resolution. Additionally, Galilean boosts/large velocities in the flow affect the truncation errors to a significantly smaller extent than in fixed grid codes due to the Galilean invariant properties of the moving mesh code. It is vital to construct a moving mesh code that preserves $\nabla \cdot \mathbf{B} = 0$ to machine precision, otherwise if differences between moving and fixed grid MHD codes are observed it becomes difficult to tell whether it is due to the advantages of moving mesh codes (such as better treatment of advection) or to the non-zero divergence errors that exist in the solution.

The new method offers new exciting possibilities of simulating MHD flows more accurately than before. One particular application it is well-suited for is the study of supersonic MHD turbulence. Here the flow has high Mach number velocities so fixed grid codes experience very restrictive timestep criteria, which can be lessened on a moving mesh. Additionally, advection errors would be reduced to a significant degree in moving mesh CT simulations. An analytic theory for supersonic MHD turbulence is virtually non-existent and numerical simulations are considered the best framework for studying this problem, necessitating numerical methods that minimize any unphysical effects of numerical errors on the solution. The moving mesh CT approach is a very viable candidate for this task.

The moving mesh CT method is also well-suited for studying astrophysical problems where advection is important. Most simulations, from accretion disc simulations to cosmological simulations, have regions that are only marginally resolved due to limitations in computational resources. As we see from our low-resolution simulations of advection, the solution in static CT methods and moving mesh methods with divergence cleaning schemes can have large diffusion errors which can be reduced only with higher resolution simulations. The moving CT approach, however, is able to accurately advect the solution to machine precision, which is one of the main benefits of the method.

> *Do not go where the path may lead, go instead where there is no path and leave a trail.*
>
> Ralph Waldo Emerson

# 4

# A 3D vector potential constrained transport scheme for MHD in AREPO

– based on –

Mocz, P., Pakmor, R., Springel, V., Vogelsberger, M., Marinacci, F., & Hernquist, L. (2016). A moving mesh unstaggered constrained transport scheme for MHD. *MNRAS*, 463, 477–488.

We present a constrained transport (CT) algorithm for solving the 3D ideal magnetohydrodynamic (MHD) equations on a moving mesh, which maintains the divergence-free condition on the magnetic field to machine-precision. Our CT scheme uses an unstructured representation of the magnetic vector potential, making the numerical method simple and computationally efficient. The scheme is implemented in the moving mesh code AREPO. We demonstrate the performance of the approach with simulations of driven MHD turbulence, a magnetized disc galaxy, and a cosmological volume with primordial magnetic field. We compare the outcomes of these experiments to those obtained with a previously implemented Powell divergence-cleaning scheme. While CT and the Powell technique yield similar results in idealized test problems, some differences are seen in situations more representative of astrophysical flows. In the turbulence simulations, the Powell cleaning scheme artificially grows the mean magnetic field, while CT maintains this conserved quantity of ideal MHD. In the disc simulation, CT gives slower magnetic field growth rate and saturates to equipartition between the turbulent kinetic energy and magnetic energy, whereas Powell cleaning produces a dynamically dominant magnetic field. Such difference has been observed in adaptive-mesh refinement codes with CT and smoothed-particle hydrodynamics codes with divergence-cleaning. In the cosmological simulation, both approaches give similar magnetic amplification, but Powell exhibits more cell-level noise. CT methods in general are more accurate than divergence-cleaning techniques, and, when coupled to a moving mesh can exploit the advantages of automatic spatial/temporal adaptivity and reduced advection errors, allowing for improved astrophysical MHD simulations.

## 4.1 INTRODUCTION

The need for performing accurate, spatially- and temporally-adaptive magnetohydrodynamic (MHD) simulations in astrophysics is evident. Magnetic fields are prevalent in a range of astrophysical systems from cosmological (Marinacci et al. 2015), cluster (McCourt et al. 2012), and galaxy (Wang & Abel 2009; Dubois & Teyssier 2010; Beck et al. 2012; Pakmor et al. 2014; Rieder & Teyssier 2016) scales, to the turbulent interstellar medium (Collins et al. 2012; Federrath & Klessen 2012; Myers et al. 2013; Federrath 2015), accretion around black holes (McKinney et al. 2014; Sądowski et al. 2014), mergers of compact objects (Zhu et al. 2015), tidal disruption events (Kelley et al. 2014), and others. Often, these systems exhibit a large dynamic range in physical and temporal scales. For example, a simulation box may contain significant regions of low density gas combined with concentrated volumes where most of the material is present and dynamical time-scales are the shortest. Adaptive, minimally-diffusive schemes are necessary for simulating such configurations precisely, given the limitations in memory and computation speed of modern supercomputing technology.

Solving the ideal MHD equations is more challenging numerically than evolving the inviscid, magnetic-free Euler equations, due to the divergence free nature of the magnetic field ($\nabla \cdot \mathbf{B} = 0$) from Maxwell's equations. This condition needs to be maintained in the discrete representation of the fluid in order for a numerical solver to be both stable and accurate. The finite-volume method is a standard approach for solving the Euler equations on a mesh. However, this technique fails for the MHD equations because divergence errors can cause the magnetic fields to blow up. On static, regular, Cartesian meshes, the state-of-the art solution to this problem is to use the constrained transport (CT) scheme (Evans & Hawley 1988), which maintains the discretized divergence of $\mathbf{B}$ to zero exactly at machine precision. This method originally comes from the staggered-mesh method of Yee (1966) for electromagnetism in a vacuum. Conceptually, the $\nabla \cdot \mathbf{B} = 0$ constraint is exactly maintained with CT by representing the magnetic field as cell face-averaged quantities (as opposed to the usual choice of volume-averages), and making use of Stokes' Theorem.

The CT method does not generalize easily, however, to moving meshes (e.g. Springel 2010, Duffell & MacFadyen 2011, Gaburov et al. 2012), and may not be at all applicable to meshless Lagrangian approaches (e.g. smoothed particle hydrodynamics (SPH) Tricco 2015, or the volume 'overlap' method of Hopkins 2015; Hopkins & Raives 2016). Consequently, numerical solvers in a Lagrangian setting have resorted to magnetic field cleaning schemes, such of those of Dedner et al. (2002) and Powell et al. (1999), which, while stable, may have unwanted numerical side-effects. This has been an unfortunate situation for these Lagrangian approaches, because otherwise they offer many advantages over static mesh codes, including automatic spatial adaptability, significantly larger CFL-limited timesteps for high Mach number flows, and reduced advection errors.

In this paper, we overcome this limitation by developing and presenting an unstaggered CT method for solving the 3D ideal MHD equations on moving meshes. Seminal ideas for our new technique come from our recent paper Mocz et al. (2014a), where we generalized the staggered CT approach to a 2D moving mesh. However, we have now modified and refined the ideas further to improve the efficiency and simplicity of the algorithm. The new scheme employs an unstructured (cell-centred) formulation, using the magnetic vector potential, which makes it straightforward to adapt to moving mesh codes. We have implemented this new unstaggered CT method into AREPO (Springel 2010), which is a state-of-the-art moving mesh code for astrophysical flows.

We provide a brief history of the development of moving mesh MHD solvers for astrophysics, to place our work in context. The finite-volume moving mesh formulation for the Euler equations was developed for astrophysical simulations by Springel (2010). The MHD equations were first solved on a moving mesh with some success in Duffell & MacFadyen (2011); Pakmor et al. (2011); Gaburov et al. (2012), using the Dedner hyperbolic divergence-cleaning scheme. However, numerical limitations of these approaches have been reported. Pakmor & Springel (2013) implemented a Powell cleaning technique for a moving mesh, which showed improved stability (even in very dynamic environments) but larger divergence errors (but still small enough in many cases to not affect dynamics). The Powell scheme has been used for science applications, including the study of magnetic fields in disc galaxies (Pakmor et al. 2014), Carbon-Oxygen white dwarf mergers (Zhu et al. 2015), and the large-scale properties of simulated cosmic magnetic fields and effects on the galaxy population (Marinacci et al. 2015; Marinacci & Vogelsberger 2016). Mocz et al. (2014a) extended the standard CT algorithm to a 2D moving Voronoi mesh, keeping track of face-averaged magnetic fields and remapping onto new faces that appear as the mesh changes connectivity. We have simplified this idea in the present paper to easily and efficiently extend it to a 3D moving mesh code.

The paper is organized as follows. We present the unstaggered moving mesh CT scheme in Section 4.2. In Section 4.3 we show the results of test problems (Orszag-Tang, circularly polarized Alfvén wave, turbulent box, magnetic disc, cosmological volume) and compare with Powell cleaning. We discuss the advantages of the new algorithm and offer concluding remarks in Section 4.4.

## 4.2 NUMERICAL METHOD FOR UNSTRUCTURED VECTOR POTENTIAL CT

In this section we describe our numerical method for an unstructured CT solver on a moving Voronoi mesh. The ideal MHD equation and some notation are presented in Section 4.2.1. The CT algorithm is detailed in Section 4.2.2. A procedure for implementing the approach in a periodic domain are discussed in Section 4.2.3.

### 4.2.1 THE MAGNETOHYDRODYNAMIC EQUATIONS

The ideal MHD equations are represented in conservation law form by:

$$\frac{\partial \mathbf{U}}{\partial t} + \nabla \cdot \mathbf{F} = 0 \tag{4.1}$$

where $\mathbf{U}$ is the vector of the conserved variables and $\mathbf{F}(\mathbf{U})$ is the flux:

$$\mathbf{U} = \begin{pmatrix} \rho \\ \rho\mathbf{v} \\ \rho e \\ \mathbf{B} \end{pmatrix}, \quad \mathbf{F}(\mathbf{U}) = \begin{pmatrix} \rho\mathbf{v} \\ \rho\mathbf{v}\mathbf{v}^T + p - \mathbf{B}\mathbf{B}^T \\ \rho e\mathbf{v} + p\mathbf{v} - \mathbf{B}(\mathbf{v}\cdot\mathbf{B}) \\ \mathbf{B}\mathbf{v}^T - \mathbf{v}\mathbf{B}^T \end{pmatrix} \tag{4.2}$$

and $p = p_{\mathrm{gas}} + \frac{1}{2}\mathbf{B}^2$ is the total gas pressure, $e = u + \frac{1}{2}\mathbf{v}^2 + \frac{1}{2\rho}\mathbf{B}^2$ is the total energy per unit mass, and $u$ is the thermal energy per unit mass. The equation of state for the fluid is given by the ideal gas law $p = (\gamma - 1)\rho u$.

The mass density ($\rho$), momentum density ($\rho\mathbf{v}$), and energy density ($\rho e$) are evolved according to the second-order, Runge-Kutta time integrator, finite volume approach presented in Pakmor et al. (2016b). However, the magnetic field is a special quantity because of the divergence-free constraint $\nabla \cdot \mathbf{B} = 0$. We now describe how to evolve this quantity, maintaining the divergence-free condition to machine precision.

### 4.2.2 UNSTAGGERED CONSTRAINED TRANSPORT ON A MOVING MESH

In the original staggered CT approach, magnetic fields are represented as fluxes normal to a cell-face, and are updated according to the induction equation by calculating the contribution from the electromotive force (EMF) in a loop around the edges of a face. In this formulation, the net change in the outward normal fluxes through any closed surface in the domain is zero, which is to say that the field is maintained divergence-free by Stokes' Theorem. The face-averaged representation of the magnetic field has been employed in Mocz et al. (2014a) for a 2D moving mesh. Here, however, we reformulate the method in an unstaggered manner to improve simplicity and efficiency. In a sense, the two methods are still very similar: the same information encoded in a staggered CT method can be encoded in an unstaggered CT scheme. Namely, the same EMF update terms added to the magnetic flux through a face can instead be added to the magnetic vector potential component projected along the sides of the face.

Consider the magnetic field $\mathbf{B}$ written in terms of the vector potential $\mathbf{A}$ under the Weyl gauge*:

$$\mathbf{B} = \nabla \times \mathbf{A}. \tag{4.3}$$

The vector potential evolves according to the induction equation

$$\frac{\partial \mathbf{A}}{\partial t} = -\mathbf{E} \tag{4.4}$$

where $\mathbf{E} = -\mathbf{v} \times \mathbf{B}$ is the electric field for an ideal MHD fluid.

In our representation, each cell $i$ maintains and evolves the volume integral of the vector potential $\mathbf{Q}_i \equiv \int_{V_i} \mathbf{A}\, dV$. The cell-averaged value $\mathbf{A}_i$ for the vector potential is thus $\mathbf{A}_i \equiv \mathbf{Q}_i / V_i$, where $V_i$ is the cell volume. On a moving mesh, $\mathbf{Q}$ evolves as

$$\frac{d\mathbf{Q}_i}{dt} = -\int_{V_i} \mathbf{E}\, dV - \int_{\partial V_i} -\mathbf{A}\mathbf{w}^T\, d\mathbf{n} \tag{4.5}$$

---

*we discuss the possibility of using other gauge choices in the supplementaty Section 4.5

where $\mathbf{n}$ is the outward normal vector of the cell surface, and $\mathbf{w}$ is the velocity at which each point in the boundary of the cell moves. The second integral term is just the advection due to the mesh motion. That is, the evolution for $\mathbf{Q}_i$ has a source term due to the electric field, and a flux term due to mesh motion. The source term is treated in a Strang-split fashion by applying two half-timesteps before and after evolving the homogeneous system by one step, similar to the treatment of the gravitational source terms in AREPO. The flux term due to mesh motion is treated by taking the upwind value of the magnetic vector potential to calculate the flux.

In discretized terms, $\mathbf{Q}_i$ is updated in a second-order approach from time step $n$ to $n+1$ with a Huen's method Runge-Kutta integrator (Pakmor et al. 2016b) as

$$\begin{aligned} \mathbf{Q}_i^{(n+1)} = \quad & \mathbf{Q}_i^{(n)} - \tfrac{\Delta t}{2}\left(\mathbf{E}_i^{(n)} V_i^{(n)} + \mathbf{E}_i' V_i'\right) && (4.6) \\ & -\tfrac{\Delta t}{2}\left(\textstyle\sum_j A_{ij}^{(n)} \mathbf{F}_{ij}^{n}(\mathbf{A}^n) + \sum_j A_{ij}^{(n+1)} \mathbf{F}_{ij}'(\mathbf{A}')\right) && (4.7) \end{aligned}$$

where $\Delta t$ is the time step, the sum is taken over all neighbours $j$, $A_{ij}$ is the area of the shared face between cells $i$ and $j$, $\mathbf{F}_{ij}$ is the upwind flux of $\mathbf{A}$ due to the mesh motion, and the primed superscript represents the variables time-extrapolated from time level $(n)$ forward by $\Delta t$. The flux is evaluated by extrapolating the cell-averaged quantities out to the faces and taking the upwind value in the Riemann problem. This update step is symmetric in the sense that it uses the mesh geometry at both the beginning and end of the timestep to evolve the fluid quantities. Note that using the electric fields predicted at cell-centers obtained from evolving the electric field with properly upwinded, shock-capturing Riemann fluxes ($\mathbf{E}_i'$) is reminiscent of the field-interpolated central difference version of constrained transport of Tóth (2000).

The key, next, is to have a CT mapping that transforms the vector potentials, $\mathbf{A}_i$, to magnetic fields $\mathbf{B}_i$, while maintaining a particular discretization of $\nabla \cdot \mathbf{B} = 0$. This value of $\mathbf{B}_i$, which we denote as $\mathbf{B}_{\rm CT,i}$, overwrites the value that would have been obtained from the Riemann solver in a finite-volume scheme, $\mathbf{B}_{\rm FV,i}$. This 'corrector' step is the standard CT approach. Sometimes, optionally, an energy correction step is applied to each cell as well to maintain consistency of the magnetic field in the total energy evolution of the fluid at the cost of machine-precision total energy conservation (Balsara & Spicer 1999),

$$\mathbf{E}_i \leftarrow \mathbf{E}_i + \frac{1}{2}B^2_{\rm CT,i} - \frac{1}{2}B^2_{\rm FV,i} \tag{4.8}$$

although we do not find this necessary for our simulations.

The CT mapping is as follows. Define the modified Delaunay tetrahedralization, by which we mean the tetrahedralization obtained from the Delaunay connections, but with the nodes, originally located at the mesh generating points, shifted slightly to the centres-of-mass of the cells. We will refer to the tetrahedra in this tetrahedralization as Delaunay tetrahedra but note that their nodes are slightly offset from the standard definition. Using the centres-of-mass instead of the mesh generating points is formally more accurate for our scheme, but the method may be implemented using the mesh generating points instead, with little effect on the results on a well-regularized mesh.

[1] First, the components $\mathbf{A}_i$ are projected onto each of the connections in a modified

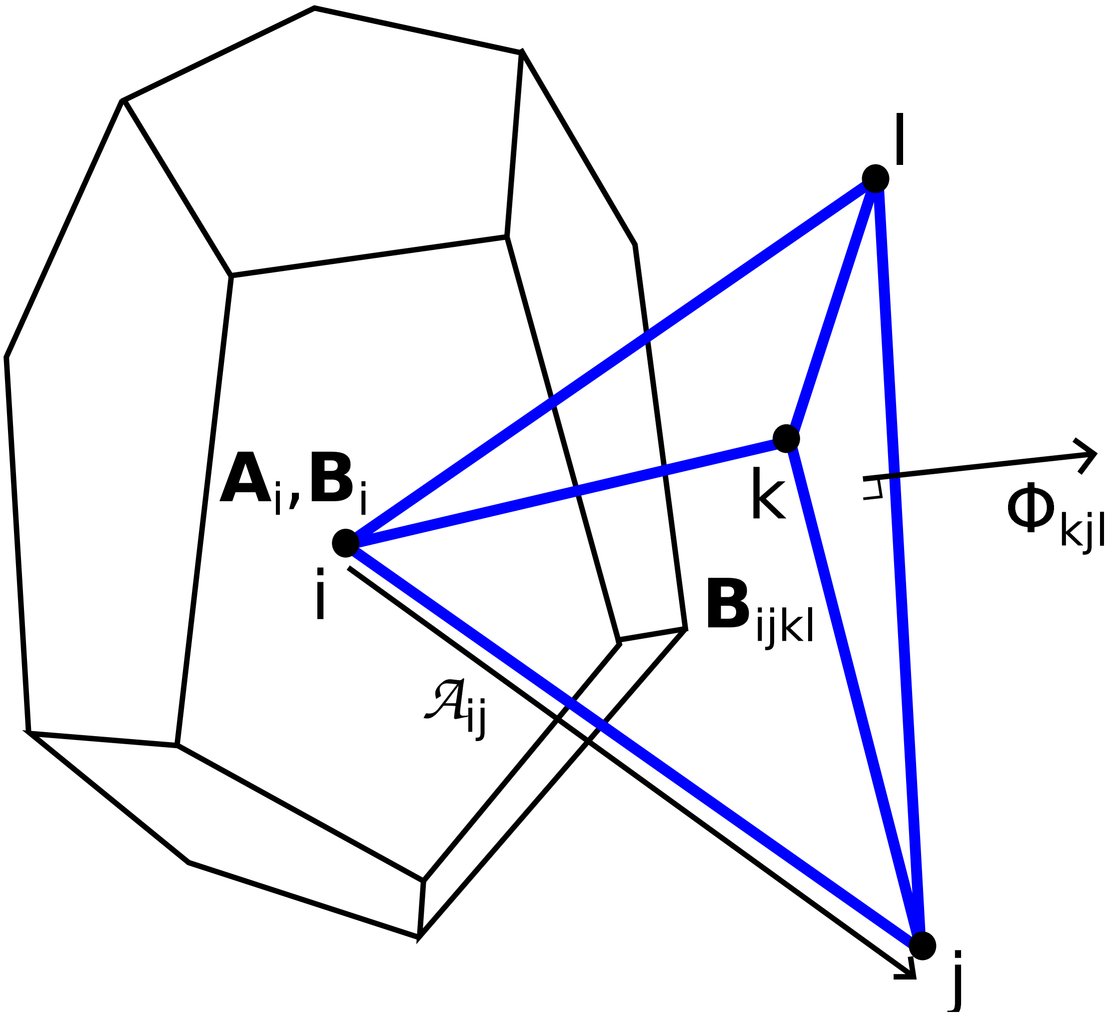

$$\mathbf{A}_i^{(n)} \rightarrow \mathcal{A}_{ij} \rightarrow \Phi_{ijk} \rightarrow \mathbf{B}_{ijkl} \rightarrow \mathbf{B}_i^{(n)} \rightarrow \mathbf{A}_i^{(n+1)}$$

**Figure 4.1:** A geometric representation of the magnetic field quantities used for the unstaggered CT representation on an unstructured mesh. The Voronoi cell $i$ is represented by the polyhedron, and one of the touching Delaunay tetrahedra is shown in blue. Points $i$, $j$, $k$, and $l$ are mesh generating points. Our method evolves the volume-averaged magnetic vector potential, which is projected along Delaunay edges, and used to recover the Delaunay face-averaged magnetic fluxes, Delaunay volume-averaged magnetic fields, and consequently cell-centred magnetic fields. The arrowed diagram shows the order of steps taken to recover the magnetic fields and evolve the system to the next time step.

Delaunay tetrahedralization of the mesh. That is, we obtain

$$\mathcal{A}_{ij} = \mathbf{A}_i \cdot d\mathbf{r}_{ij} \tag{4.9}$$

where $\mathbf{r}_{ij}$ is the connection pointing from the center-of-mass of cell $i$ to the center-of-mass of cell $j$.

[2] Next, the outward normal component of the magnetic flux $\Phi_{ijk}$ is computed on each of the Delaunay tetrahedral faces (with vertices labelled by mesh generating point $i$, $j$, and $k$). We note that in an unstaggered CT approach, such as that of Mocz et al. (2014a), the quantities $\Phi_{ijk}$ would be evolved directly. However, evolving the vector potential instead and mapping down to face fluxes is more efficient and easier to implement. The $\Phi_{ijk}$ pointing along the direction given by the right-hand rule with nodes $i$, $j$, and $k$ counter-clockwise, is:

$$\Phi_{ijk} = \frac{1}{2}\left(\mathcal{A}_{ij} - \mathcal{A}_{ji} + \mathcal{A}_{jk} - \mathcal{A}_{kj} + \mathcal{A}_{ki} - \mathcal{A}_{ik}\right) \tag{4.10}$$

as it comes from the equation for the magnetic flux through a surface

$$\Phi_S = \oint_{\partial S} \mathbf{A} \cdot d\ell \tag{4.11}$$

where the line integral is computed with a counter-clockwise orientation around the boundary of the surface $S$.

[3] Next, the full magnetic field $\mathbf{B}_{ijkl}$ in each Delaunay tetrahedron is reconstructed from

the magnetic fluxes $\Phi_{ijk}$, $\Phi_{ijl}$, $\Phi_{jkl}$, $\Phi_{kil}$. Note that the divergence free condition implies $\Phi_{ijk} + \Phi_{ijl} + \Phi_{jkl} + \Phi_{kil} = 0$ (it is exactly this value that is preserved to machine precision by our CT approach). So there are 3 degrees of freedom represented in both $\mathbf{B}_{ijkl}$ and the face magnetic fluxes. Hence, there is a unique magnetic field vector that projects onto the faces to give the four desired (divergence-free) fluxes. We find the value of the magnetic field by inverting the linear system

$$\begin{pmatrix} \mathscr{A}_{x,ijk} & \mathscr{A}_{y,ijk} & \mathscr{A}_{z,ijk} \\ \mathscr{A}_{x,ijl} & \mathscr{A}_{y,ijl} & \mathscr{A}_{z,ijl} \\ \mathscr{A}_{x,jkl} & \mathscr{A}_{y,jkl} & \mathscr{A}_{z,jkl} \end{pmatrix} \begin{pmatrix} B_{x,ijkl} \\ B_{y,ijkl} \\ B_{z,ijkl} \end{pmatrix} = \begin{pmatrix} \Phi_{ijk} \\ \Phi_{ijl} \\ \Phi_{jkl} \end{pmatrix} \tag{4.12}$$

where the $\mathscr{A}_{ijk}$ are the outward vector areas of the faces. Note that we are using an integral condition to recover $\mathbf{B} = \nabla \times \mathbf{A}$, so we are not assuming that $\mathbf{A}$ is differentiable, which can be a pitfall for some vector potential numerical schemes for solving the MHD equations.

[4] Finally, the Delaunay tetrahedral magnetic fields are converted to Voronoi cell magnetic fields $\mathbf{B}_i$ by volume averaging all the magnetic fields of the tetrahedra that touch cell $i$.

Figure 4.1 illustrates the geometrically-averaged quantities we have defined, and shows a diagram illustrating the steps required to recover the cell-centred magnetic fields.

We also note that a magnetic field needs to be supplied to the Riemann solver for the update of the other fluid variables using the finite volume approach. We found it sufficient to take the extrapolated cell-centred magnetic fields out to the faces, with the normal component through the face averaged across the two sides, as done in Pakmor et al. (2011).

### 4.2.3 MAGNETIC VECTOR POTENTIAL IN PERIODIC BOUNDARY CONDITIONS

Here we describe the implementation of the magnetic vector potential approach in a periodic domain. Note that while $\mathbf{B}$ is periodic, $\mathbf{A} = \nabla \times \mathbf{B}$ need not be. However, in general, the magnetic vector potential may be decomposed into a periodic part and a non-periodic part which corresponds to the mean magnetic field, which is an invariant of ideal MHD. Thus:

$$\mathbf{A}_i(\mathbf{x}, t) = \mathbf{A}_{i,\text{mean-field}}(\mathbf{x}) + \mathbf{A}_{i,\text{periodic}}(\mathbf{x}, t) \tag{4.13}$$

So, to implement periodic boundary conditions, one may keep track of and update $\mathbf{A}_{i,\text{periodic}}(\mathbf{x}, t)$ and always add to it $\mathbf{A}_{i,\text{mean-field}}(\mathbf{x})$, which is static in time and determined by the mean-field.

## 4.3 NUMERICAL TESTS

We test our numerical method on five problems: the classic Orszag-Tang vortex, the propagation of a circularly polarized Alfvén wave, driven MHD turbulence, the formation of an idealized magnetized disc, and a cosmological volume with stellar and black hole feedback.

### 4.3.1 ORSZAG-TANG

First, we compare our moving mesh CT method to CT on a static mesh and moving-mesh Powell cleaning by simulating the classic Orszag & Tang (1979) vortex, a well-known 2D

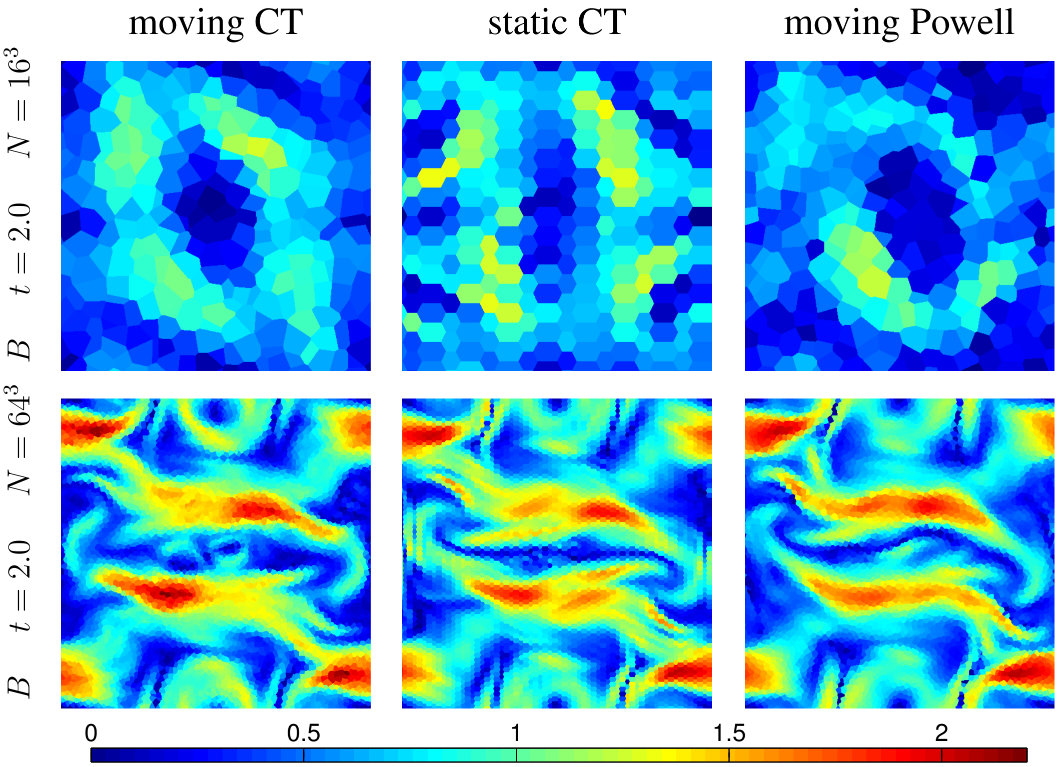

**Figure 4.2:** A comparison of moving CT, static CT, and moving Powell schemes for the Orszag-Tang test, as labeled at the top. The magnetic field strength is shown at $t = 2.0$, simulated at low (upper panels) and high (lower panels) resolutions. All approaches give results consistent and accurate results.

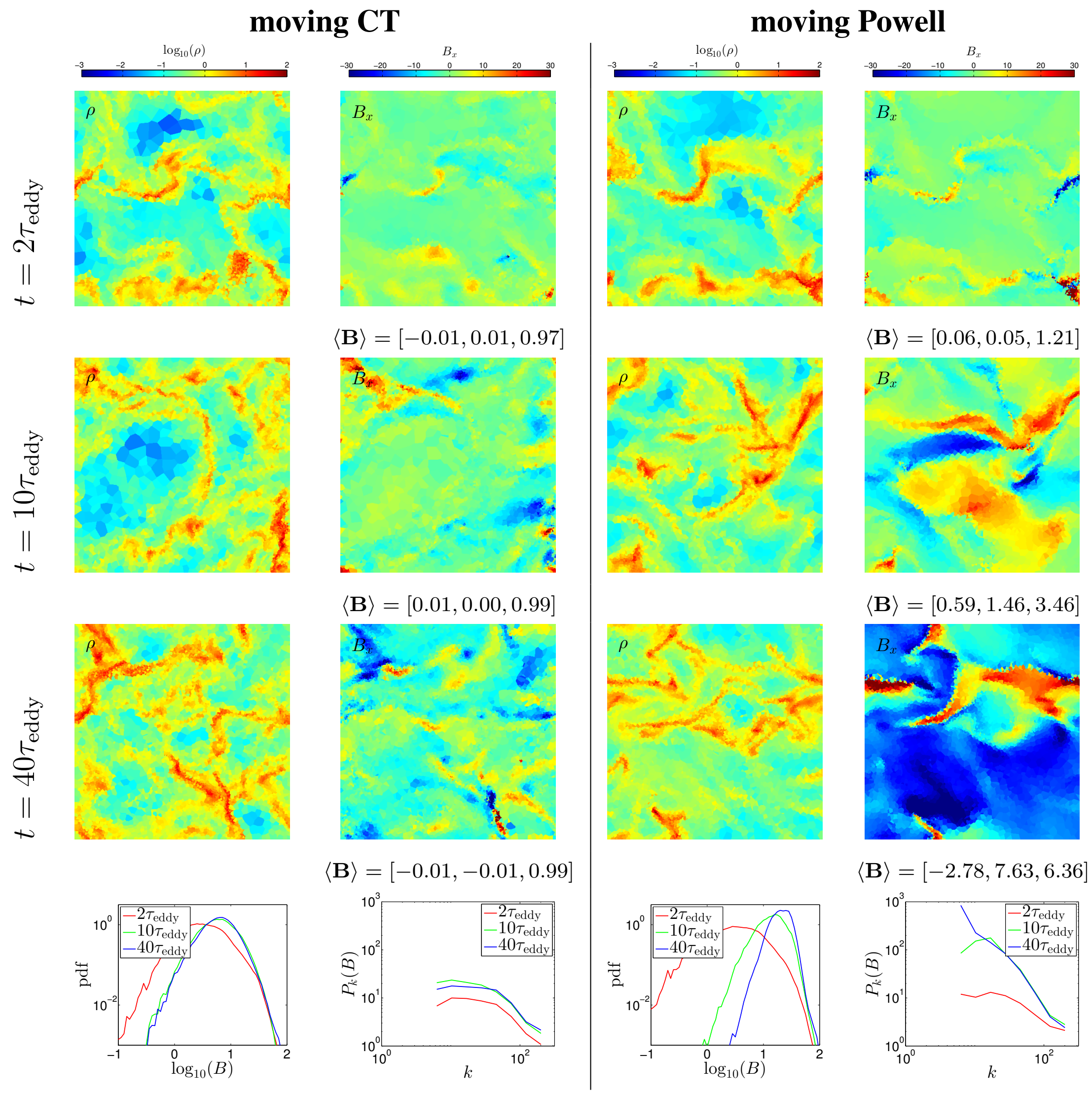

**Figure 4.3:** Comparison of the moving mesh CT and Powell schemes used to simulate $\mathcal{M}_{\rm s} \sim 10$, $\mathcal{M}_{\rm A} \sim 3$ turbulence. Plotted are slices of the density field, $x$ component of the magnetic field, and the the PDF and power spectra of the magnetic field at $t = 2, 10, 40$ eddy turnover times. In the plots of $B_x$ we also list the volume-averaged mean magnetic field in the domain, which is an ideal MHD invariant (its initial value was set to $\mathbf{B} = (0, 0, 1)$). At $2$ eddy turnover times, when the turbulence is transitioning into the non-linear saturated regime, the two schemes show similar features in the density and magnetic field. However, after more eddy turnovers, the Powell scheme artificially makes the mean magnetic field grow significantly due to its non-conservative formulation and shifts the entire magnetic field PDF of the magnetic field to the right, as well as transfers most of the magnetic energy to the largest scale ($k = 2 \cdot \pi$). The CT scheme offers good control over the mean magnetic field and shows a stable PDF and power spectrum of the magnetic field.

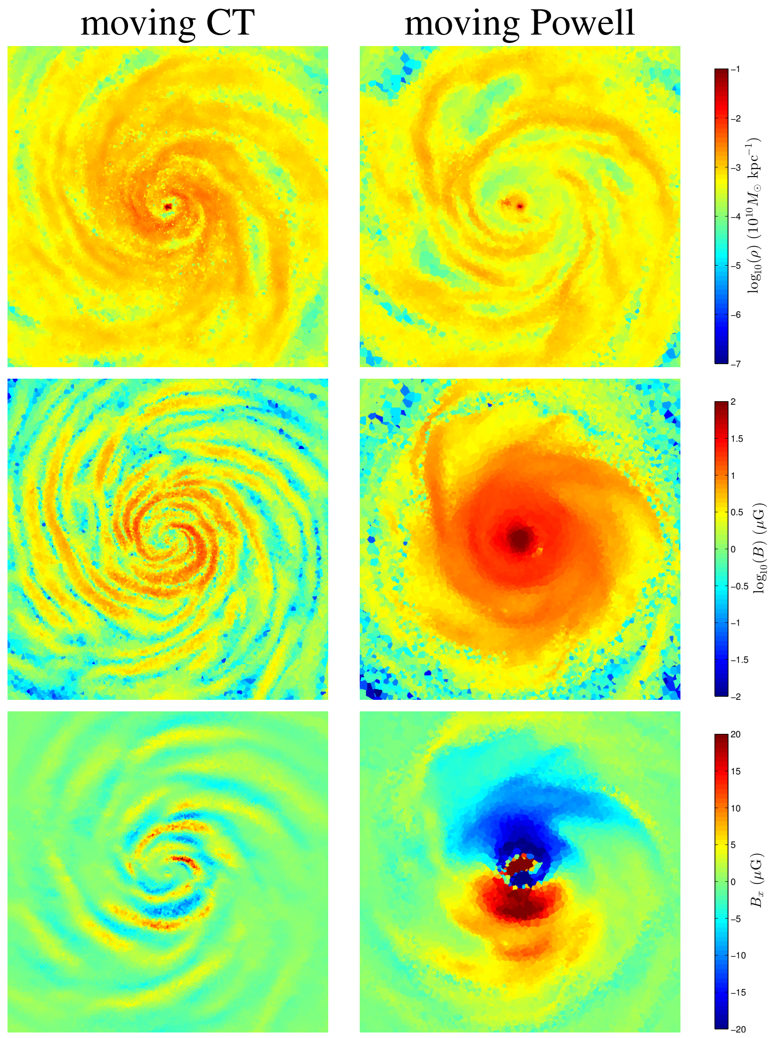

**Figure 4.4:** Comparison of magnetic field saturation in the formation of a disc simulated with the CT and Powell schemes. Shown are the density, magnetic field strength, and magnetic field $x$ component, of the disc at $t = 2.5$ Gyr. Each panel displays a physical region of side length $40\ \mathrm{kpc}$. With the Powell scheme, unlike the CT method, the magnetic field has grown dynamically dominant and disrupts the disc.

test problem for MHD codes that initiates decaying supersonic turbulence. Our set-up of the problem is described in Mocz et al. (2014a). Here, we simulate this 2D system inside a 3D box, with all fluid variables being repeated along the $z$-direction. The initial mesh generating points are staggered, to yield a non-degenerate Delaunay tetrahedralization of the mesh (which is not necessary for our method, but speeds up initial mesh construction). We simulate the system using resolutions of $N = 16^3$ and $N = 64^3$ to evaluate the pre-converged and resolved behaviours of the methods.

Figure 4.2 shows the results of the tests. All the methods give robust, accurate answers with sufficient resolution. We used an initially staggered mesh that is not exactly aligned with the symmetries of the initial conditions, hence giving rise to small asymmetries in all the simulations. At low/marginally-resolved resolution, the Powell scheme can be sensitive to the divergence-cleaning source term, since divergence errors can be the largest at low resolution, which breaks the symmetry of the problem to a greater extent.

### 4.3.2 CIRCULARLY-POLARIZED ALFVÉN WAVE

We simulate the circularly-polarized Alfvén wave of Tóth (2000) in 3D. The solution has a known analytic expression, and therefore we can use this test to verify the convergence properties of our scheme. The non-linear Alfvén wave is chosen to propagate along the diagonal of a $2 \times 1 \times 1$ periodic box of size $3 \times 1.5 \times 1.5$, as described in Stone et al. (2008). We use a staggered mesh with resolution $2 \times (2N \times N \times N)$. The problem is initialized with $\rho = 1$, $p_{\rm gas} = 0.1$, $\Gamma = 5/3$. In a coordinate frame defined along the diagonal, the wave has velocity

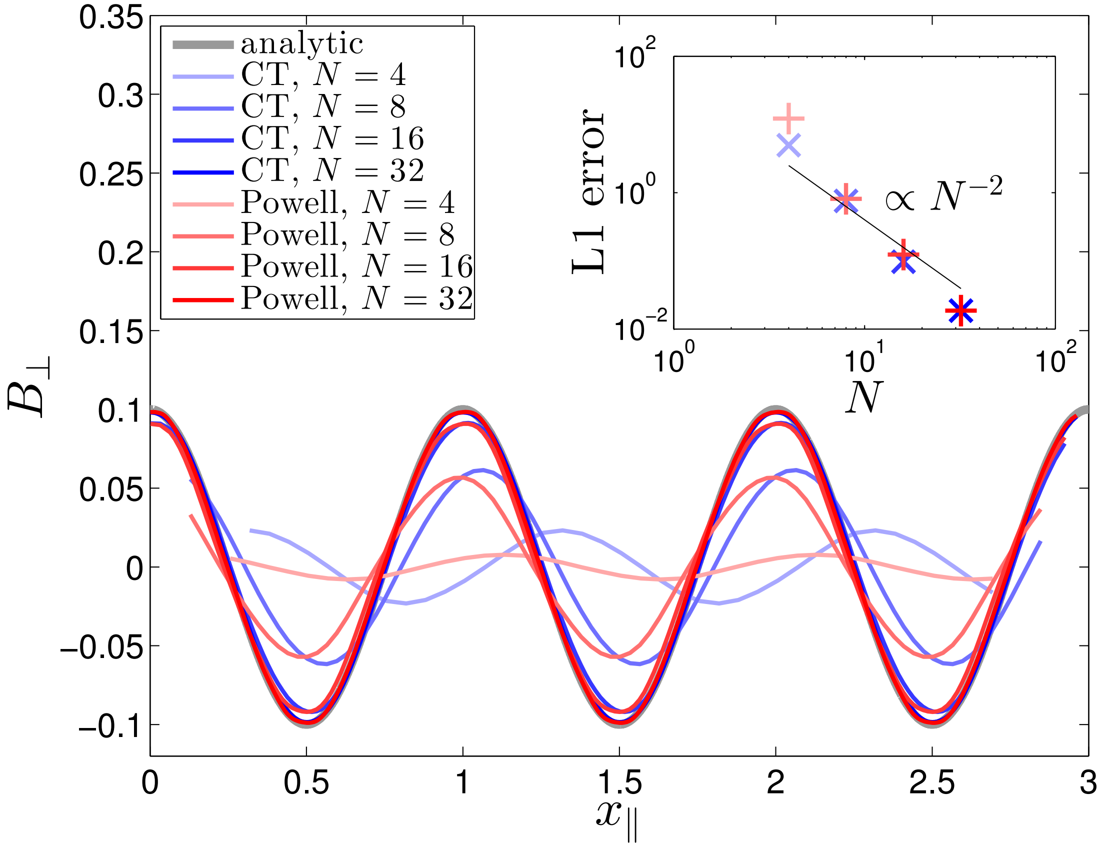

**Figure 4.5:** Convergence of the non-linear circularly-polarized Alfvén wave (3D simulation) with the moving Powell and CT schemes.

and magnetic field $v_\perp = B_\perp = 0.1\sin(2\pi x_\parallel)$, $v_\parallel = 0$, $B_\parallel = 1$, $v_z = B_z = 0.1\cos(2\pi x_\parallel)$. The solution returns to it's original state at time $t = 1$.

Figure 4.5 shows the convergence of the magnetic field of the Alfvén wave at $t = 1$ as a function of the resolution $N$. The analysis shows second order behaviour as expected for both the Powell and CT schemes.

### 4.3.3 TURBULENT BOX

We next simulate isothermal supersonic MHD turbulence using the driving routine of Federrath et al. (2010); Price & Federrath (2010), adapted for the AREPO code in Bauer & Springel (2012). The initial conditions are set up in dimensionless units: boxsize $L = 1$, sound speed $c_s = 1$, initial density $\rho_0 = 1$, initial magnetic field $\mathbf{B} = (0, 0, 1)$, and we use $64^3$ resolution elements. We drive the velocity field solenoidally in Fourier-space on large spatial injection scales to establish a turbulent box characterized by a sonic Mach number of $\mathcal{M}_{\rm s} \sim 10$ and Alfvénic Mach number of $\mathcal{M}_{\rm s} \sim 3$. Saturated turbulence (i.e., with steady time-averaged statistical properties modulo the effects of intermittency) is expected to be established after a few eddy turnover times.

The results of our simulation are shown in Figure 4.3. We plot a slice of the density field, $x$-direction magnetic field, probability density function (PDF) of the magnetic field strength, and the radially averaged $1D$ power spectrum of the magnetic field at 2, 10, and 40 eddy turnover times. At 2 eddy turnover times, when the turbulence is transitioning into the non-linear saturated regime, both the CT and Powell scheme show similar features in the density and magnetic field, and the power spectrum (we have used the same random number seed for the turbulent driving). Hence, we know that both codes perform reasonably well in the linear regime of this simulation. The magnetic field power-spectrum is flat on the injection scales and falls over the inertial range. This shape is in good agreement with the magnetic power spectra calculated in Tricco et al. (2016), which compares turbulent box simulations using a

Cartesian mesh constrained transport scheme (implemented in FLASH) and an SPH method for MHD.

At later times, the CT and Powell schemes differ. The CT scheme shows approximately time-steady behaviour of the magnetic field PDF and power spectrum, as expected. Additionally, the volume averaged mean magnetic field ($\langle \mathbf{B} \rangle = (0, 0, 1)$), a conserved quantity in ideal MHD, is well-preserved. Figure 4.3 lists the mean field values, which are generally preserved to within $1$ per cent (in fact, they are conserved to machine precision under our scheme on a static mesh, as is the case for the original CT scheme). The Powell scheme, on the other hand, shows poor behaviour in the non-linear regime. The mean magnetic field continues to grow, the magnetic field PDF keeps shifting to the right to higher field strengths, and power is transferred to the largest spatial scale ($k = 2 \cdot \pi$). The magnetic field have grown by over an order-of-magnitude from its expected value. This is problematic for the simulation: the magnetic field becomes dominant and changes the nature of the turbulence as it transitions from a super-Alfvénic to sub-Alfvénic regime.

### 4.3.4 MAGNETIC DISC

We simulate the formation of an isolated Milky-Way sized disc galaxy under idealized conditions, as done previously in Pakmor & Springel (2013), which used the moving Powell method to evolve the magnetic fields. Here, we compare results from the moving CT and moving Powell methods. Our simulation set-up uses $2 \cdot 10^5$ particles (effective mass resolution of $\sim 3 \times 10^5\ M_\odot$), and has an initial $3 \cdot 10^{-10}$ G magnetic field along the $x$-axis. The total angular

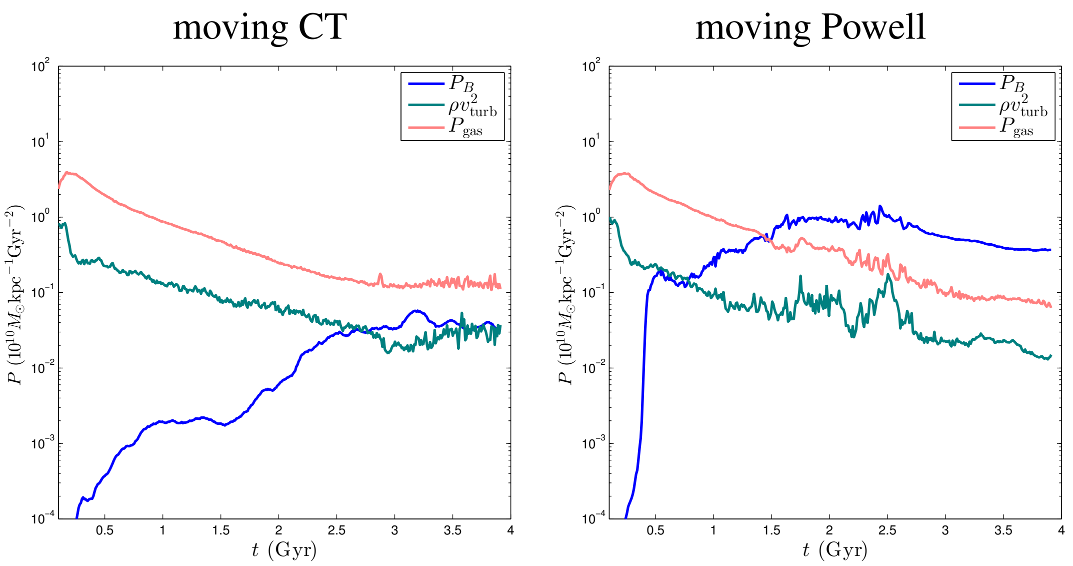

**Figure 4.6:** Comparison of magnetic field saturation in the formation of a disc simulated with the CT and Powell schemes. The CT method shows equipartition between magnetic energy density and turbulent kinetic energy density, whereas the Powell technique saturates the field at higher values, exceeding the thermal pressure by about a factor of five.

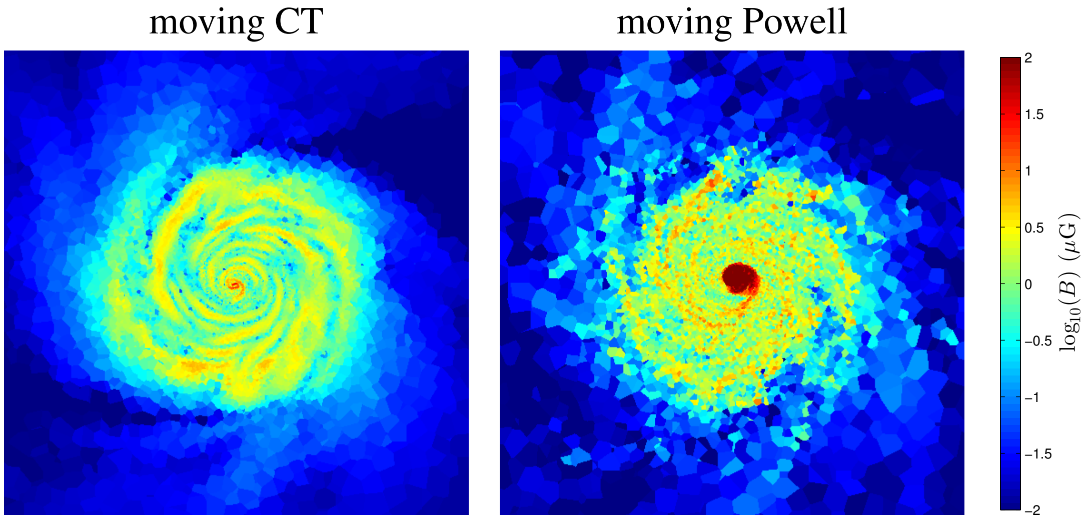

**Figure 4.7:** Comparison of the magnetic field strength of the same disc in Figure 4.4 at time $t = 0.5\ \mathrm{Gyr}$ in the formation process, simulated using the CT and Powell schemes. The figure displays a physical size of $40\ \mathrm{kpc}$. The CT approach exhibits much better preservation of the topological winding of the magnetic field. The Powell scheme shows substantial divergence error noise seen on the cell level while this is absent to machine precision in CT.

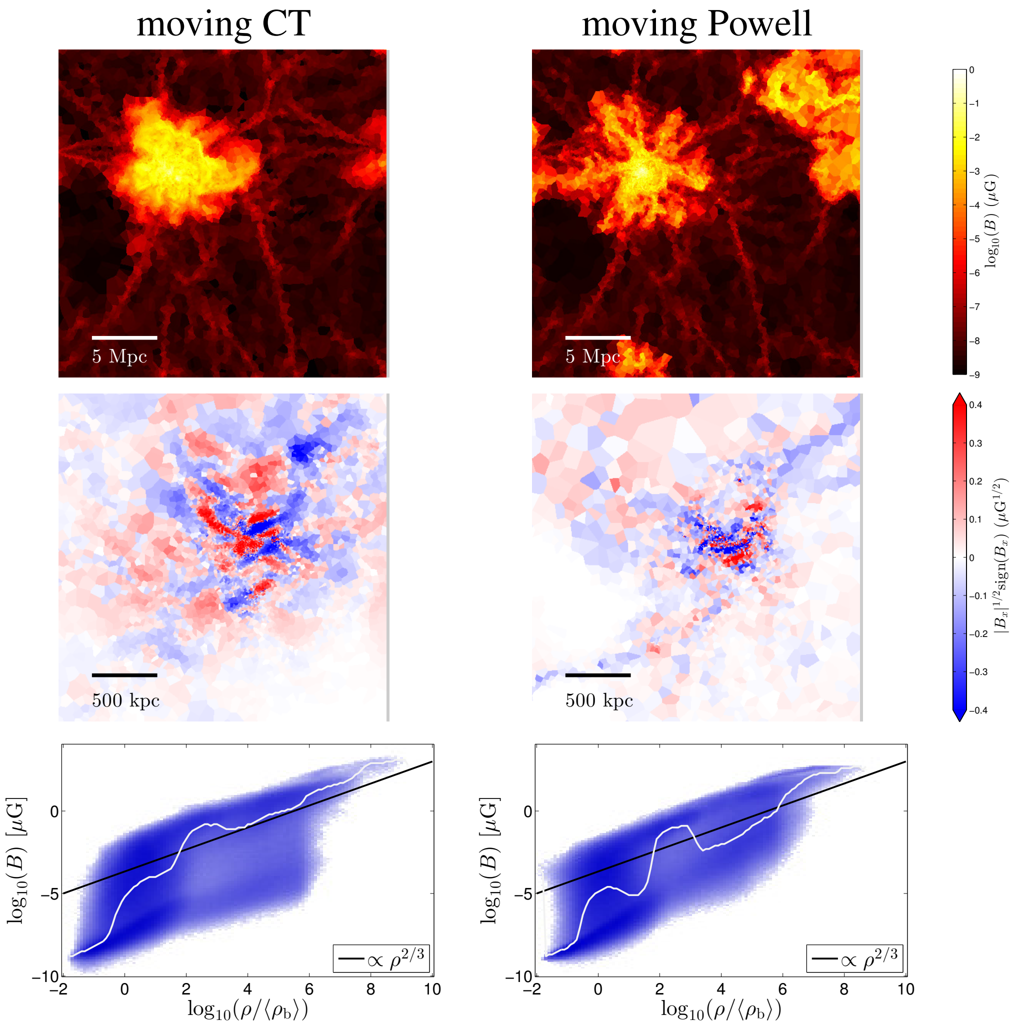

**Figure 4.8:** Magnetic fields (strength and $x$-component, top and middle panels respectively) and their phase-space distribution (bottom panels) at $z = 0$, in a $h^{-1}25$ Mpc cosmological box with full feedback physics as obtained with the CT and Powell schemes. The magnetic strengths and the phase space diagram are similar. In the phase-space diagram, the white line shows the median magnetic field strength at a given density. Under pure adiabatic compression, $B \propto \rho^{2/3}$ is expected due to flux-freezing. There is a difference in the magnetic field topology in the two simulations. The zoom-in on the $B_x$ profile shows that the CT scheme exhibits larger structure and less individual cell-scale noise.

momentum vector is initially along the $z$-axis.

The results comparing our CT method with the Powell cleaning are given in Figures 4.4 and 4.6. We show the density field, magnetic field strength, and $x$ component of the magnetic field in the disc at $2.5$ Gyr in Figure 4.4. We show the time evolution of the magnetic pressure, thermal pressure, and turbulent kinetic energy density in Figure 4.6. These quantities are calculated as volume averaged values inside a cylinder of radius $15\ \mathrm{kpc}$ and height $1\ \mathrm{kpc}$ centred on the disc. The turbulent velocity for the calculation of the turbulent kinetic energy density is calculated by subtracting the mean rotational velocity (the formed disc has a flat $\sim 200\ \mathrm{km\ s}^{-1}$ rotation curve) from the gas velocities and computing the root-mean-square.

Using the Powell scheme, Pakmor & Springel (2013) found that the magnetic field strength in the disc is quickly amplified, due to small-scale dynamo action, shearing motions and the central starburst, and eventually saturates. In this equilibrium state, the magnetic field pressure equals a few times the thermal pressure.

Our results with the CT scheme provide a modified picture. The saturation proceeds more slowly and reaches a lower value. This asymptotic level is in equipartition with the turbulent kinetic energy density, in agreement with the theoretical and numerical understanding of the galactic dynamo and turbulence as well as observations of our Galaxy (Kraichnan 1965; Zweibel & McKee 1995; Beck et al. 1996; Hawley et al. 1996). The topology of the magnetic field is also quite different. The winding structure of the magnetic field is preserved to a greater degree with CT. The magnetic field in the CT method is not dynamically large enough to disrupt the central parts of the disc and cause strong outflows for our particular set-up. The winding of the magnetic field is expected, as the divergence-free condition enforces a topological constraint on the magnetic field. The ability of a CT code as opposed to Powell cleaning to maintain topological constraints is shown in Figure 4.7, where we plot the magnetic field structure in the disc at a time of $0.5$ $\mathrm{Gyr}$ before much of the magnetic field amplification due to shear and small-scale dynamo action has taken place (thus we would expect a smooth profile showing twisting of the field lines that follows the rotation of the fluid). We see clearly that the CT algorithm exhibits a winding-structure of the magnetic field whereas the Powell scheme has considerable noise at the level of individual mesh cells due to divergence errors. We have quantified the divergence errors relative to the total gas pressure, which describes the dynamical effects of the error. With the CT scheme, the divergence errors are zero to the level of machine precision, while in the Powell scheme, we have found that the errors are of order $10$ percent in the central parts of the disc.

### 4.3.5 COSMOLOGICAL BOX

We simulate a $25h^{-1}$ $\mathrm{Mpc}$ box cosmological box at $256^3$ resolution with a weak initial seed magnetic field of strength $10^{-14}$ G, using the set-up described in Marinacci et al. (2015). The simulation includes the full physics (stellar and active-galactic nuclei (AGN) feedback and radiative cooling) of the ILLUSTRIS simulation (Vogelsberger et al. 2013, 2014a,b; Nelson et al. 2015). Figure 4.8 shows the $z = 0$ magnetic field strength in a slice of the box, the magnetic field $B_x$ component zoomed in on a halo, and $\rho$–$B$ phase-space distribution of the gas. The phase-space distribution of the magnetic field strengths and the densities (normalized by mean baryon density) are fairly similar for the CT and Powell methods. The phase-space distribution is expected to follow a $B \propto \rho^{2/3}$ under pure adiabatic compression due to the flux-freezing condition (solid black line). The magnetic field exceeds this value due to amplification by shearing and dynamo action. Federrath et al. (2011b) isolate the dynamo action and separating it from the compressional amplification of B, and provide general properties of the dynamo in a compressible gas in Federrath et al. (2011a). Only in halo centres does the magnetic field become strong enough to slightly influence the gas dynamics. While magnetic fields are amplified to similar strengths using the two numerical methods, their topologies differ. The Powell scheme shows more noise at the level of individual cells due to divergence errors. Some of the differences in the structure is attributed to the stochasticity of the feedback model.

### INDUCTION EQUATION IN COMOVING COORDINATES

We offer remarks on how we chose to implement the induction equation in cosmological comoving coordinates. The global expansion of the universe is characterized by the time-dependent scale factor $a(t)$. The simulation is evolved on a mesh in comoving variables $\mathbf{x}$, and the standard physical fluid variables are also converted to 'comoving' variables, which are the quantities being evolved. We use the quantities defined in section 2.2 of Pakmor & Springel (2013). The 'comoving' magnetic field $\mathbf{B}_{\rm c}$ that our base scheme solves is related to the physical magnetic field $\mathbf{B}$ by $\mathbf{B} = \mathbf{B}_{\rm c} a^{-2}$. As Pakmor & Springel (2013) point out, this choice has the advantage of eliminating source terms in the induction equation. For our vector potential CT scheme, we define the 'comoving' vector potential $\mathbf{A}_{\rm c}$ by $\mathbf{B}_{\rm c} = \nabla_{\mathbf{x}} \times \mathbf{A}_{\rm c}$. The induction equation is then given by:

$$\frac{\partial \mathbf{A}_{\rm c}}{\partial t} = -\frac{1}{a}\left(-\mathbf{u} \times \mathbf{B}_{\rm c}\right) \tag{4.14}$$

where $\mathbf{u}$ is the peculiar velocity.

## 4.4 DISCUSSION

While the Powell and CT schemes both yield accurate results in idealized test problems (such as the Orszag-Tang vortex and the propagation of a circularly polarized Alfvén wave), we find that the two approaches can lead to different outcomes for astrophysical flows with magnetic field amplification and turbulence in the non-linear regime. Divergence cleaning techniques have been shown to produce spurious structures and magnetic energy fluctuations on small spatial scales due to the non-locality of the cleaning step (Tóth 2000; Balsara & Kim 2004), whereas CT schemes produce robust results.

In moving mesh simulations of turbulent and astrophysical flows, the Powell and CT schemes give a similar general picture, but exhibit some quantitative differences. Zhu et al. (2015) discusses that Powell cleaning gives faster field growth and larger saturation at lower resolutions in general, where the divergence errors are larger. This is consistent with our results for the magnetized disc. The CT method reaches the natural equipartition between the magnetic energy density and the turbulent kinetic energy density in the disc, whereas the Powell scheme overshoots this value and the magnetic pressure dominates the gas pressure by a factor of five. In the original Powell magnetic disc simulations of Pakmor & Springel (2013), the authors find even larger ($> 10\times$) overshoots of the magnetic pressure over gas pressure in their lowest resolution simulation (12500 particles; see their Figure 7). The CT scheme can be considered particularly more robust at low/marginally-resolved resolutions, which will always be the situation in practice for some structures in large-scale cosmological simulations.

This difference between CT and Powell in the growth rate and saturation of the magnetic field in magnetized disc galaxies is observed across different codes in the literature as well. Adaptive mesh refinement (AMR) with the divergence-preserving CT scheme (Wang & Abel 2009; Dubois & Teyssier 2010; Rieder & Teyssier 2016) find slow growth rates compared to the fast growth rates (e-folding time $\sim 10$ Myr) of divergence cleaning schemes implemented in SPH (Beck et al. 2012) or moving mesh (Pakmor & Springel 2013). The difference we observe between our CT and Powell simulations suggests that divergence cleaning, and not the Eulerian vs Lagrangian natures of the codes, is the culprit. Rieder & Teyssier (2016) point out that in simulations without strong stellar feedback (such as ours), the flows are relatively smooth and two-dimensional, a regime in which strong dynamo amplification is difficult.

In the case of the cosmological box simulations, the two schemes give similar statistics for the overall magnetic field strengths in the density - magnetic field phase space. However, the CT algorithm produces a smoother magnetic field, without the magnetic field unphysically flipping at the single-cell level. This property will improve Faraday rotation measure estimates and cosmic ray propagation (Pfrommer et al. 2016; Pakmor et al. 2016a) in the AREPO code.

The difference between the moving mesh CT and Powell schemes can perhaps be best understood with the idealized turbulence test, where the behaviour of the true solution is known theoretically. The Powell scheme, with its non-conservative formulation (divergence correcting source-terms), artificially makes the magnetic field grow in this particular test problem and quickly transfers magnetic energy to the largest scales. The mean magnetic field (which should be a conserved quantity in ideal MHD as the equations for the evolution of the magnetic field can be recast into standard conservative hyperbolic form) grows by over an order of magnitude and information about the initial mean field direction is also lost. Interestingly, the disc simulation shows similar difference between the CT and Powell schemes as these turbulence tests; namely the Powell scheme grows the magnetic field beyond the turbulent kinetic energy and most of the magnetic power is on the largest scales (size of the disc).

Finally, we also note that our unstructured (cell-centred) CT formalism may find useful application in static mesh codes, and may potentially be used to simplify some of the technical details of implementing CT in a code with AMR (Balsara 2001; Fromang et al. 2006; Mignone et al. 2012) as well.

A moving mesh unstaggered CT approach has some practical advantages over an AMR code with staggered CT. The unstaggered representation allows for straightforward coupling with refinement and power of two hierarchical time stepping on a moving Voronoi mesh. There is no difficulty introduced as in the fine and coarse level mismatch in AMR codes, where specific care (such as restriction, prolongation, and reflux-curl operations Miniati & Martin 2011) has to be taken to prevent a loss of order of accuracy and breaking of the divergence-free condition at interface regions. In addition, the moving mesh approach provides the usual advantages of automatic adaptivity and reduced advection errors.

Summarizing, we have developed an efficient, accurate, unstructured CT scheme for solving the MHD equations in 3D on a moving mesh. The CT formulation allows for the maintenance of the divergence-free condition on the magnetic field to machine precision, which leads to numerical stability, more accurate numerical solutions, and good preservation of the topological properties of the magnetic field. The numerical experiments we considered demonstrate the advantages of CT schemes over cleaning schemes, namely preventing artificial magnetic field growth due to the source terms in cleaning schemes. The new CT method, implemented in the moving mesh code AREPO, will allow for powerful MHD simulations in the upcoming future, making use of the advantages of an adaptive, quasi-Lagrangian treatment of the fluid equations.

## 4.5 OTHER GAUGE CHOICES

In this supplementary section, we discuss the gauge choice in the numerical method.

The evolution of the magnetic field is invariant under a choice of gauge $\psi$ for the vector potential:

$$\frac{\partial \mathbf{A}}{\partial t} = -\mathbf{E} - \nabla\psi \tag{4.15}$$

In the present work, we chose to evolve the vector potential under the *Weyl* gauge ($\psi = 0$), as it offers a nice correspondence between CT and vector potential methods because one is adding just the same EMF terms to update the solution in both cases. However, it may be of some interest to explore other gauge choices in future work, as they can be more suitable to the treatment of particular problems/physical processes. We briefly discuss alternate choices here.

One may choose the *Coulomb* gauge, $\nabla \cdot \mathbf{A} = 0$. This gauge choice would require using either projection methods or cleaning methods on $\mathbf{A}$ to keep it divergence free. This choice of gauge would simplify the extension of the ideal MHD code to resistive MHD, as the induction equation for resistive MHD is given by:

$$\frac{\partial \mathbf{A}}{\partial t} = \mathbf{v} \times \mathbf{B} - \eta \nabla \times (\nabla \times \mathbf{A}) \tag{4.16}$$

where the resistive term expands as: $\eta \nabla (\nabla \cdot \mathbf{A}) - \eta \nabla^2 \mathbf{A}$, which is just a diffusion term if $\nabla \cdot \mathbf{A} = 0$.

Another choice would be to choose a *helicity-like* gauge: $\psi = \mathbf{v} \cdot \mathbf{A}$. This choice of gauge makes the magnetic vector potential induction equation Galilean-invariant:

$$\frac{d\mathbf{A}}{dt} = -\mathbf{A} \times \nabla \times \mathbf{v} - (\mathbf{A} \cdot \nabla)\mathbf{v} = -\boldsymbol{J}_{\mathbf{v}}^{\mathrm{T}} \mathbf{A} \tag{4.17}$$

where $\boldsymbol{J}_{\mathbf{v}}$ denotes the Jacobian of $\mathbf{v}$. The downside of this gauge is that the velocity field may not be differentiable, so special care would have to be taken for the treatment of the Jacobian term in the presence of shocks.

A final interesting choice would be to modify the above helicity-like gauge to use the mesh motion velocity $\mathbf{w}$ instead: $\psi = \mathbf{w} \cdot \mathbf{A}$, in which case the induction equation becomes

$$\frac{d\mathbf{A}}{dt} = (\mathbf{v} - \mathbf{w}) \times \mathbf{B} - \boldsymbol{J}_{\mathbf{w}}^{\mathrm{T}} \mathbf{A} \tag{4.18}$$

The first term $(\mathbf{v} - \mathbf{w}) \times \mathbf{B}$ is just the electric field in the frame of the moving mesh, which is $0$ if the mesh cell moves exactly with the fluid. This choice of gauge reduces to the Weyl gauge in the case of a static mesh. Such a gauge would require smoothed mesh motion (e.g. Duffell & MacFadyen 2015) to treat the Jacobian term accurately and avoid mesh noise.

*Look deep into nature, and then you will understand*

*everything better.*

Albert Einstein

# 5

# Moving mesh simulations of star forming cores in magneto-gravo-turbulence

– based on –

Mocz, P., Burkhart, B., Hernquist, L., McKee, C. F., & Springel, V. (2017). Moving-mesh Simulations of Star-forming Cores in Magneto-gravo-turbulence. *ApJ*, 838, 40.

Star formation in our Galaxy occurs in molecular clouds that are self-gravitating, highly turbulent, and magnetized. We study the conditions under which cloud cores inherit large-scale magnetic field morphologies and how the field is governed by cloud turbulence. We present four moving-mesh simulations of supersonic, turbulent, isothermal, self-gravitating gas with a range of magnetic mean-field strengths characterized by the Alfvénic Mach number $\mathcal{M}_{\rm A,0}$, resolving pre-stellar core formation from parsec to a few AU scales. In our simulations with the turbulent kinetic energy density dominating over magnetic pressure ($\mathcal{M}_{\rm A,0} > 1$), we find that the collapse is approximately isotropic with $B \propto \rho^{2/3}$, core properties are similar regardless of initial mean-field strength, and the field direction on 100 AU scales is uncorrelated with the mean field. However, in the case of a dominant large-scale magnetic field ($\mathcal{M}_{\rm A,0} = 0.35$), the collapse is anisotropic with $B \propto \rho^{1/2}$. This transition at $\mathcal{M}_{\rm A,0} \sim 1$ is not expected to be sharp, but clearly signifies two different paths for magnetic field evolution in star formation. Based on observations of different star forming regions, we conclude that star formation in the interstellar medium may occur in both regimes. Magnetic field correlation with the mean-field extends to smaller scales as $\mathcal{M}_{\rm A,0}$ decreases, making future ALMA observations useful for constraining $\mathcal{M}_{\rm A,0}$ of the interstellar medium.

## 5.1 INTRODUCTION

Magnetic fields and turbulence are known to play key roles in star formation (Larson 1981; Shu et al. 1987; McKee et al. 1993; Crutcher et al. 2010; Crutcher 2012), and both compete against the self-gravity of the gas and strongly affect the dynamics of collapse. The relative importance of one over the other may have significant consequences for how pre-stellar cores collapse, including whether the collapse: (1) is isotropic, (2) is self-similar, and (3) has magnetic field lines that shape filamentary structure or turbulence that shape the field lines.

Turbulent motions in the interstellar medium are known to be highly supersonic (Larson 1981; Burkhart et al. 2015), with giant molecular clouds (GMCs) having sonic Mach numbers $\mathcal{M}_{\rm s} \sim 10$, meaning that turbulent pressure greatly exceeds thermal pressure. The magnetic field is also known to be important. Often a coherent mean-field can be measured on large (parsec) scales and density structures in the ISM are filamentary, and diffuse clouds are thought to be assembled by flows along magnetic field lines (Crutcher et al. 2010). The relative importance between the turbulent kinetic energy density $E_{\rm k,turb}$ and the magnetic pressure $P_B$ can be characterized by the Alfvénic Mach number $\mathcal{M}_{\rm A} = (E_{\rm k,turb}/P_B)^{1/2}$, where super-Alfvénic ($\mathcal{M}_{\rm A} > 1$) signifies turbulence dominance and sub-Alfvénic ($\mathcal{M}_{\rm A} < 1$) signifies magnetic pressure dominance.

How gravitational collapse occurs in molecular clouds in our Galaxy is debated both observationally and theoretically. Observationally, Zeeman measurements of interstellar magnetic field strengths give the mass-averaged line-of-sight field, $\langle B_z \rangle_M$, in the telescope beam. Crutcher et al. (2010) collected Zeeman observations of both atomic and molecular gas and used Bayesian analysis to infer that the mass-weighted total field satisfied $\langle B \rangle_M \propto \langle \rho \rangle^{0.65}$, where $\langle \rho \rangle$ is the mean density of the gas in the observed region, in gas denser than $n_{\rm H} = 300\,{\rm cm}^{-3}$, almost all of which is molecular. Li et al. (2015b) confirmed this result by showing that the Crutcher et al. (2010) data on molecular gas implies $\langle B\rangle_M \propto \langle\rho\rangle^\alpha$ with $\alpha = 0.64 \pm 0.13$. A non-turbulent pre-stellar core undergoing homologous contraction with a frozen-in field has $B \propto \rho^{2/3}$ (Mestel 1965; the core must be pre-stellar since non-ideal MHD effects become important in the vicinity of a protostar). The observations are also consistent with the model of fast turbulent reconnection diffusion of the magnetic field relative to the free fall time of collapse (Lazarian et al. 2012). In their ideal MHD simulations of a turbulent, self-gravitating gas, Li et al. (2015b) compute the scaling relation taking density-averaged magnetic fields, as observers would from Zeeman measurements, and apply observational effects such as convolution with the beam, for the 100 most massive clumps in their simulation: they found a result for $\langle B\rangle_M$ consistent with the observations of Crutcher et al. (2010). They considered Alfvénic ($\mathcal{M}_{\mathrm{A},0} = 1$) and super-Alfvénic ($\mathcal{M}_{\mathrm{A},0} = 10$) turbulence only, where $\mathcal{M}_{\mathrm{A},0}$ is based on the mean magnetic field.

Alternatively, Tritsis et al. (2015) suggest that the Crutcher et al. (2010) observations better support a $B \propto \rho^{1/2}$ scaling based on re-estimating observational uncertainties in the determination of cloud and core densities, signaling anisotropic collapse with dynamically important magnetic fields. Previous theoretical work (Mestel 1966; Mouschovias 1976b,a) on the problem of the equilibrium of self-gravitating, isothermal, strongly magnetized clouds in the ISM finds that the ratio of magnetic and gas pressure should remain close to unity near the center of the cloud, $B_{\mathrm{c}} \propto \rho^{1/2}$. Axisymmetric calculations of gravitational collapse in a strong magnetic field under the influence of ambipolar diffusion give $B_{\mathrm{c}} \propto \rho_{\mathrm{c}}^{\kappa}$ with $\kappa < 1/2$ (Ciolek & Mouschovias 1994). It should be borne in mind, however, that $\kappa$ in the relation between

$B_\mathrm{c}$ and $\rho_\mathrm{c}$ may be independent of the power-law index in the observed $\langle B\rangle_M(\langle\rho\rangle)$ relation. Ideal MHD simulations of star forming cores in turbulent environments with weak mean-field ($\mathcal{M}_{\mathrm{A},0} \gg 1$) by Collins et al. (2011, 2012) find a scaling close to $B_\mathrm{c} \propto \rho_\mathrm{c}^{0.4-0.5}$ when examining the distribution magnetic fields and densities of the gas cells in their simulation. The scaling relation, simply deduced from a cell-by-cell determination, is different to the $B \propto \rho^{2/3}$ scaling of Li et al. (2015b) using density-averaged line-of-sight fields. Recent observations of the massive star forming region NGC 6334 (Li et al. 2015a) on 100–0.01 pc scales shows self-similar hourglass-like magnetic field structure with $B \propto \rho^{0.41}$. We note, however, that the magnetic field values in Li et al. (2015a) are inferred using various approximate methods, as opposed to being directly measured by Zeeman splitting as in Crutcher et al. (2010), so the errors associated with the slope of the relation are much larger. Hourglass morphologies, suggesting dynamically important magnetic fields, have been observed in a number of other cores as well (Girart et al. 2006; Stephens et al. 2013; Rao et al. 2009; Tang et al. 2009; Qiu et al. 2014); however, such morphologies also occur in the simulations of Li et al. (2015b), which have $\mathcal{M}_{\mathrm{A},0} = 1$.

These observations and theoretical predictions have important implications for the influence and transport of the magnetic field during collapse. However, only in recent years have numerical simulations advanced to the point where theoretical predictions can be tested and observational parameters/physics reproduced. This is, in part, due to the extreme numerical expense of simulating many orders of magnitude in spatial scale and density range to study the collapse of a parsec scale cloud down to the AU scale disk where a star is born.

In this paper, we present novel moving mesh AREPO simulations of the collapse of pre-stellar cores in supersonic, turbulent, isothermal, magnetized environments, exploring the effect of the mean magnetic field-strength (an invariant of ideal MHD). These numerical simulations self-consistently resolve star formation in a large-scale turbulent environment (5pc) down to a few AU scale and are well-situated to help improve our theoretical understanding of the star formation process, interpret observations, and constrain the regimes in which star formation occurs. The moving mesh numerical framework allows us to efficiently explore a range of initial field strengths and resolve the core collapse down to AU scales, relevant for upcoming sub-arcsecond spatial resolution observations by the Atacama Large Millimeter Array (ALMA; ALMA Partnership et al. 2015). We are able to resolve the cores by a factor of $> 8$ improvement in spatial resolution compared to similar studies that use adaptive mesh refinement (AMR) (Collins et al. 2011, 2012; Li et al. 2015b), until the approximate isothermal condition breaks down and the core is expected to continue adiabatic collapse on smaller scales. These simulations are particularly relevant to understanding the morphologies of Class 0 protostars.

The paper is organized as follows. In § 5.2 we describe our numerical methods and simulation setup. We present projected morphologies in § 5.3. We investigate the density dependence of the magnetic field in the pre-stellar cores in § 5.4 and compute their radially averaged profiles in § 5.5. We discuss our findings in § 5.6 and our main conclusions in § 5.7.

**Table 5.1:** Simulation initial conditions

| sim. | $\beta_0$ | $\mathcal{M}_{\rm A,0}$ | $\mathcal{M}_{\rm s}$ | $\mu_{\Phi,0}$ | comment |
|---|---|---|---|---|---|
| 1 | 25 | 35 | 10 | 80 | very weak field |
| 2 | 0.25 | 3.5 | 10 | 8 | weak field |
| 3 | 0.028 | 1.2 | 10 | 2.7 | moderate field |
| 4 | 0.0025 | 0.35 | 10 | 0.8 | strong field |

**Table 5.2:** Simulation final configurations

| sim. | first core $t_{\rm collapse}$ $(t_{\rm ff})$ | $\alpha$ $(B \propto \rho^{\alpha})$ | $\mu_\Phi$ | mean-field aligned within 30° $10^6$ AU to $(\cdot)$ AU | fraction of gas at $10^4$ AU scale with field aligned within 30° |
|---|---|---|---|---|---|
| 1 | 0.12 | $0.64 \pm 0.02$ | 12.7 | $10^{2.0}$ | 0.00 |
| 2 | 0.16 | $0.66 \pm .02$ | 16.5 | $10^{3.7}$ | 0.23 |
| 3 | 0.17 | $0.67 \pm .01$ | 12.1 | $10^{4.0}$ | 0.35 |
| 4 | 0.37 | $0.55 \pm .02$ | 5.8 | $10^{5.5}$ | 0.86 |

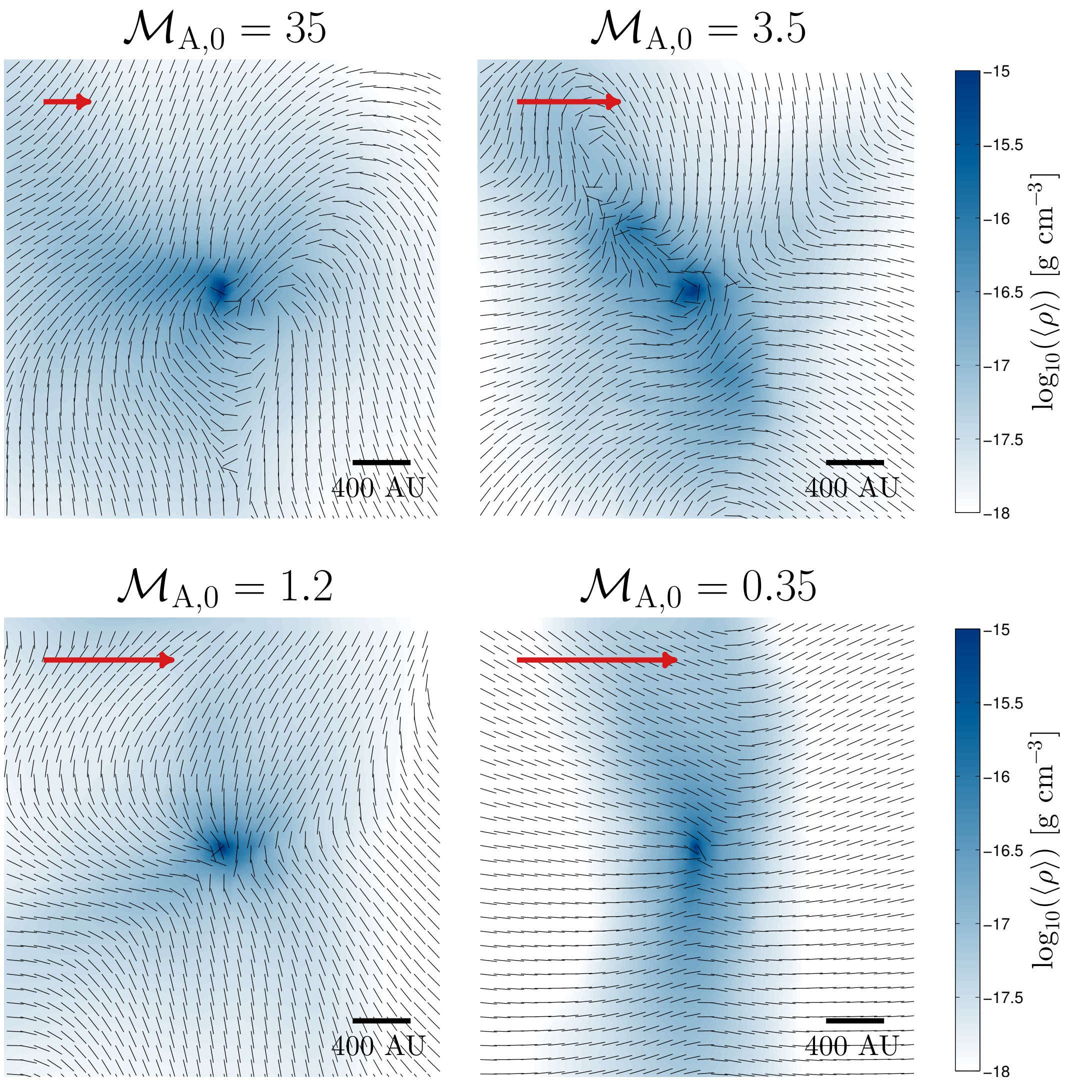

**Figure 5.1:** Density-averaged line-of-sight magnetic field and projected gas densities zoomed in on a core in each of the simulations. The arrow in the top left represents the initial magnetic field.

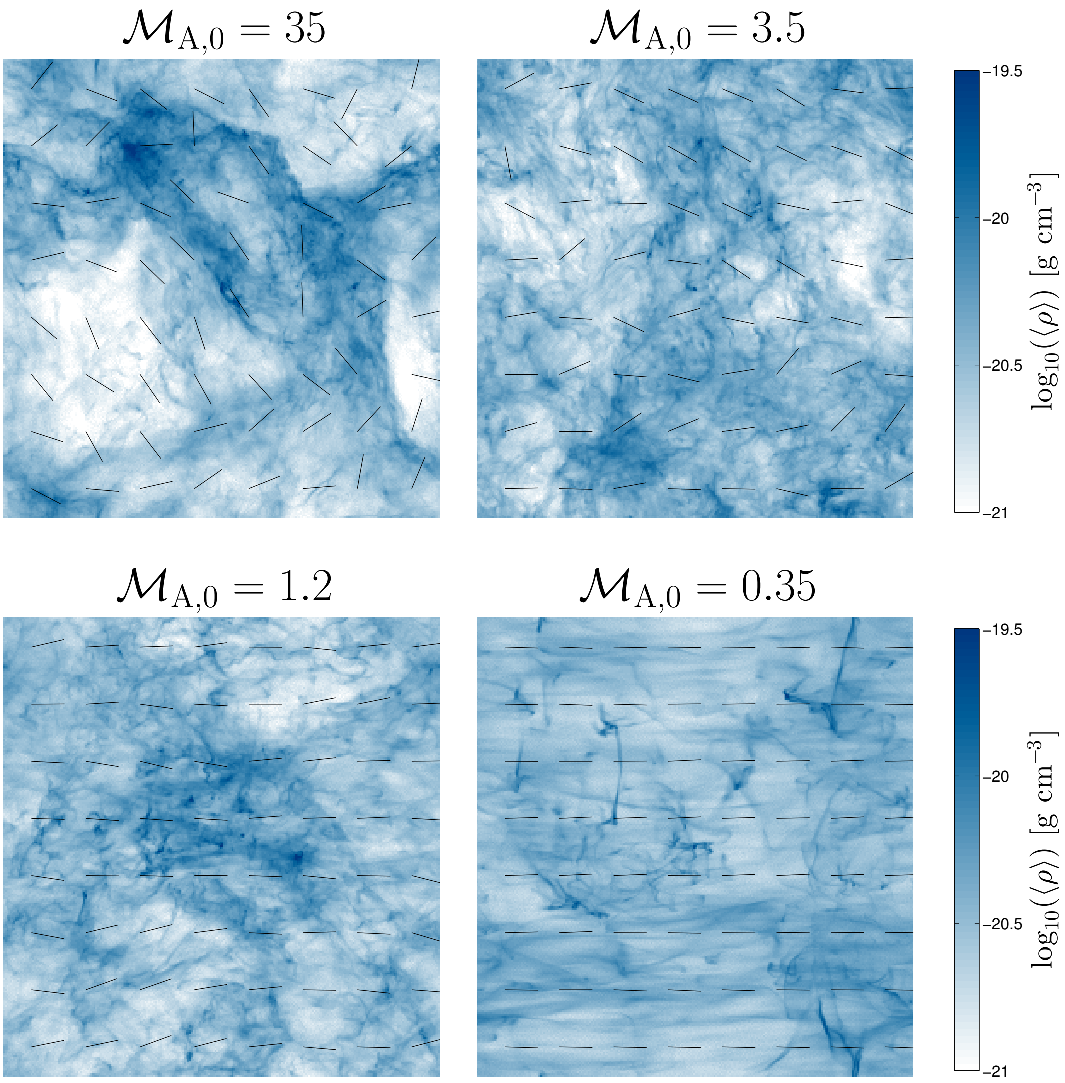

**Figure 5.2:** Density-averaged line-of-sight magnetic field and projected gas densities of the entire simulation domain ($5.2$ pc) for the 4 simulations. Each box is centered on the corresponding pre-stellar cores shown in Figure 5.1.

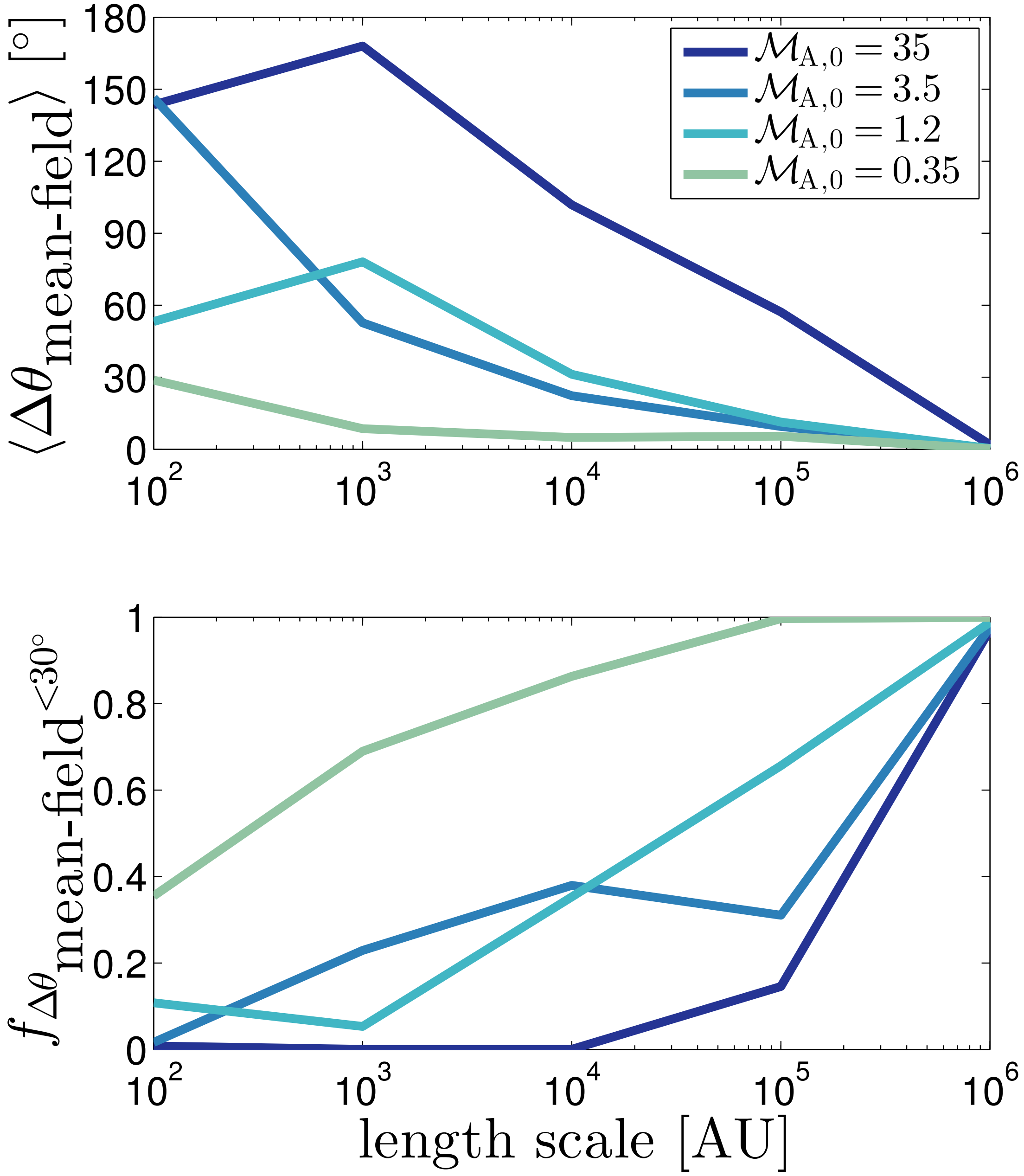

**Figure 5.3:** (*Top*) Deviation of the mean-magnetic field averaged over some length-scale around the core from the large (pc) scale field. (*Bottom*) Fraction of gas inside a sphere of radius the length scale with the magnetic field aligned within $30$ degrees of the large-scale mean-field value.

## 5.2 SIMULATIONS

We simulate the collapse of star forming cores under self-gravity in a turbulently-driven interstellar medium environment. Our simulations are performed using the moving-mesh quasi-Lagrangian AREPO code (Springel 2010). The moving mesh automatically adapts to the geometry of the physical system, and keeps the mass-resolution of each cell approximately constant. The code solves the ideal MHD equations, for which we have recently implemented (Mocz et al. 2016) an unstructured vector potential constrained transport (Yee 1966; Evans & Hawley 1988) solver to maintain the divergence-free property of the magnetic field. We accurately capture shocks via an HLLD (Miyoshi & Kusano 2005) Riemann solver. Self-gravity is calculated using a Tree-Particle-Mesh scheme (Xu 1995). Turbulence is driven solenoidally in Fourier space on the largest spatial scales using an Ornstein-Uhlenbeck process (Federrath et al. 2010; Bauer & Springel 2012; Federrath 2015).

We run four isothermal simulations, representing part of a GMC, with different initial mean-field strengths, $B_0$. Turbulence is characterized by the sonic Mach number $\mathcal{M}_{\rm s} = v_{\rm rms}/c_{\rm s} = 10$. The cloud has Virial parameter: $\alpha_{\rm vir} = 5v_{\rm rms}^2(L/2)/(3GM_0) = 1/2$. The physical parameters of the simulations (assuming a mass per hydrogen of $1.4$ amu) can be scaled as:

$$\begin{aligned}
L_0 &= 5.2\left(\tfrac{c_s}{0.2\text{ km s}^{-1}}\right)\left(\tfrac{n_H}{1000\ cm^{-3}}\right)^{-1/2}\left(\tfrac{\mathcal{M}_{\rm s}}{10}\right)\ \text{pc}\\
B_0 &= 1.2, 12, 36, 120\left(\tfrac{c_s}{0.2\text{ km s}^{-1}}\right)\left(\tfrac{n_H}{1000\ cm^{-3}}\right)^{1/2}\ \mu\text{G}\\
M &= 4860\left(\tfrac{c_s}{0.2\text{ km s}^{-1}}\right)^3\left(\tfrac{n_H}{1000\text{ cm}^{-3}}\right)^{-1/2}\left(\tfrac{\mathcal{M}_{\rm s}}{10}\right)^3 M_\odot
\end{aligned} \tag{5.1}$$

where $L_0$ is the size of the periodic box with total mass of $M$. We scale the simulations to physical units using sound speed $c_\mathrm{s} = 0.2\ \mathrm{km\ s^{-1}}$ and hydrogen density $n_\mathrm{H} = 1000\ \mathrm{cm^{-3}}$.*

The simulation initial conditions, ranging from very weak seed fields to strong fields that surpass the turbulent kinetic energy density, are summarized in Table 5.1. The plasma beta parameter ($\beta = P_\mathrm{gas}/P_B = 8\pi P_\mathrm{gas}/B^2$) describes whether gas pressure ($\beta > 1$) or magnetic pressure ($\beta < 1$) dominates. Similarly, the Alfvénic Mach number $\mathcal{M}_\mathrm{A}$ describes whether the turbulent kinetic energy density ($\mathcal{M}_\mathrm{A} > 1$) or magnetic pressure ($\mathcal{M}_\mathrm{A} < 1$) dominates. Note $\beta = 2\mathcal{M}_\mathrm{A}^2/\mathcal{M}_\mathrm{s}^2$. Each simulation uses $256^3$ cells, corresponding to a mass resolution of $8 \cdot 10^{-5}\ M_\odot$.

In the simulations, we first drive turbulence until quasi-steady state is established after a couple of eddy-turnover times. Then, we turn on self-gravity (continuing to drive turbulence) which eventuates in the collapse of cores on the order of the free-fall time. We follow the collapse for a fraction of the free-fall time, until we form cores that are resolved at the level of a few AU at their centers. We stop the simulations at this point because the time-stepping becomes prohibitively expensive and we lack mass-resolution to further resolve the collapse. Furthermore the isothermal assumption is expected to break down beyond these scales, because opacity increases and is able to trap heat and hence the collapse continues adiabatically. Our simulation strategy is to accurately resolve the first core that forms to small (AU) scales. The core centers are identified by determining local minima in the gravitational potentials.

---

* We note our choice of physical scaling makes the cloud fall on the observed line width-size scaling relation for molecular clouds in our Galaxy: $\sigma_\mathrm{nt} = \sigma_\mathrm{pc} R_\mathrm{pc}^{1/2}$, with $\sigma_\mathrm{pc} \simeq 0.72\ \mathrm{km\ s^{-1}}$ (McKee & Ostriker 2007). Here $R_\mathrm{pc} = (L_0/2)/(1\ \mathrm{pc})$ and $\sigma_\mathrm{nt} = \mathcal{M}_\mathrm{s} c_\mathrm{s}/\sqrt{3}$ (as in McKee et al. 2010).

Table 5.2 lists the times at which these pre-stellar cores form which we analyze. A discussion on the other (less-collapsed) cores that result from turbulent fragmentation are discussed in the supplementary Section 5.8.

The mass-to-flux ratio is parametrized in dimensionless form as $\mu_{\Phi,0} \equiv M_0/M_\Phi$ ($M_\Phi$ is the magnetic critical mass that can undergo gravitational collapse) assesses the relative strength of the magnetic field and gravity. For the box in its initial uniform, static state, it can be defined as $\mu_{\Phi,0} \sim \sqrt{5\pi/3}\mathcal{M}_{\mathrm{A},0}$ (Equation 27 of McKee et al. 2010). Thus our four simulation initial conditions are characterized by $\mu_{\Phi,0} = 80, 8, 2.7, 0.8$. The strong-field box is estimated to be slightly sub-critical, but we find collapse if turbulence is switched on (the core in this case forms later, at $\sim 0.4t_{\mathrm{ff}}$, as opposed to $\sim 0.2t_{\mathrm{ff}}$ in the weaker-field simulations). Being able to form a core in the sub-critical case is consistent with the picture of reconnection diffusion, which acts to reduce the mass-to-flux ratio in the core (Lazarian et al. 2012).

Our simulations are similar to the setup of Collins et al. (2011, 2012) and Li et al. (2015b). However, Collins et al. (2011, 2012) assume a very weak magnetic field. Li et al. (2015b) has one weak-field and one moderate ($\mathcal{M}_{\mathrm{A},0} = 1$) setup. Furthermore, these previous AMR simulations do not resolve the collapse down to a few AU scales: the effective resolutions of Collins et al. (2012) and Li et al. (2015b) are 120 AU and 500 AU respectively. Our smallest cells have an effective diameter of $d = 2\left(3V/(4\pi)\right)^{1/3} \simeq 4$ AU (where $V$ is the volume of the cell), corresponding to adding $\geq 3$ extra refinement levels to these AMR simulations.

AREPO uses a refinement/derefinement strategy to ensure all cells maintain their initial mass to within a factor of 2. Additionally, further refinement is used to ensure the Truelove criterion is met to accurately resolve the local Jeans length $\lambda_{\rm J} = \left(c_{\rm s}^2\pi/(G\rho)\right)^{1/2}$ (Truelove et al. 1997) and prevent artificial fragmentation, whose implementation is described in Becerra et al. (2015).

## 5.3 PROJECTIONS

Figure 5.1 shows density-averaged line-of-sight magnetic field and column densities, zooming in on a 3000 AU × 3000 AU region of the densest collapsed core in each simulation (projections for the entire simulation domain are shown in Figure 5.2). The mean-field points in the horizontal ($x$) direction. The strong-field case ($\mathcal{M}_{\rm A,0} = 0.35$) shows highly-elongated structure (perpendicular to the mean-field direction) and a classical hourglass magnetic field morphology aligned with the mean-field direction. The weak-field simulations ($\mathcal{M}_{\rm A,0} > 1$) show more chaotic magnetic field morphology dictated by turbulence, with pinches and clumps. Figure 5.3 shows the deviation in the mean magnetic field ($\langle\Delta\theta_{\text{mean-field}}\rangle$) from its large (pc) scale direction as a function of scale: alignment becomes poorer with weaker mean-field strengths. The degree of alignment can remain tight to the smallest scales in the strong mean-field regime. Figure 5.3 also shows a related quantity: the (volume) fraction of gas within a sphere of radius $r$ (the length scale) that has a magnetic field aligned within 30 degrees of the large-scale mean-field value ($f_{\Delta\theta_{\text{mean-field}}<30^\circ}$).

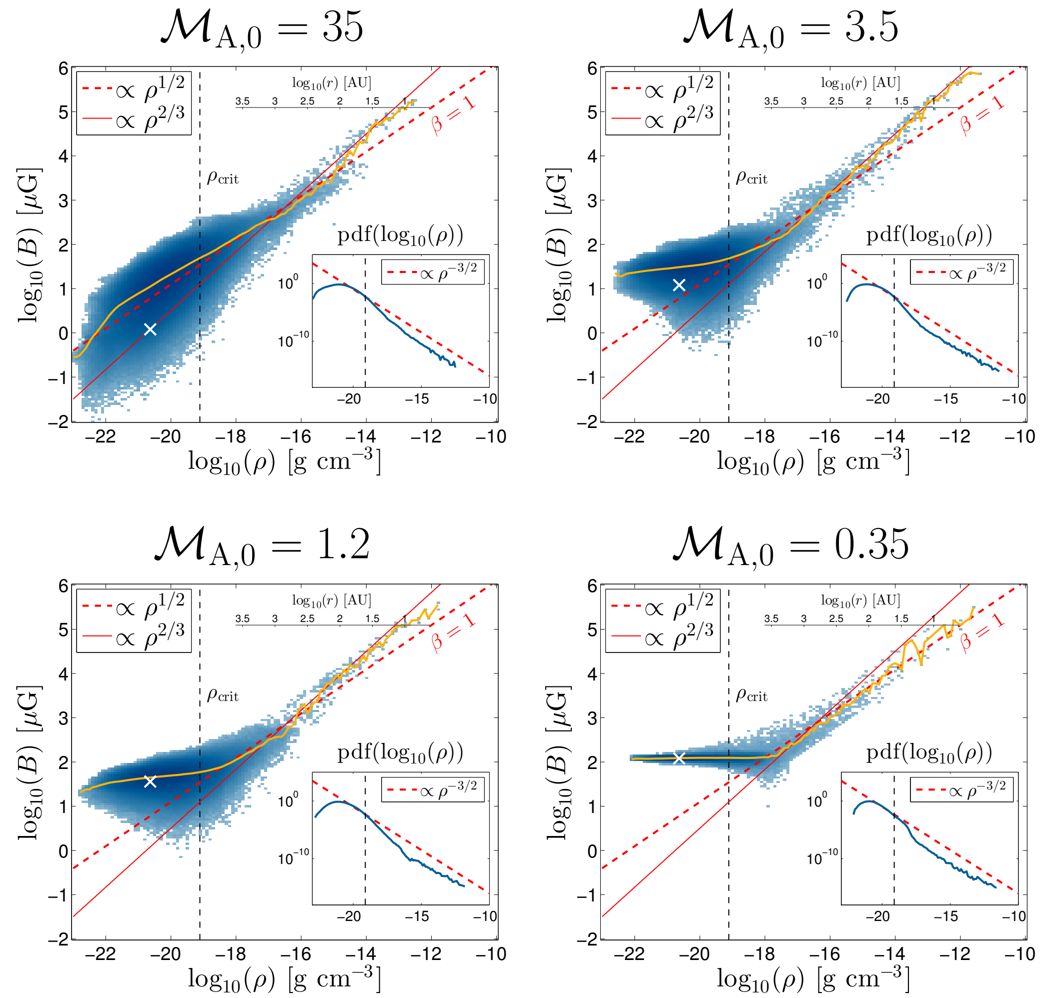

**Figure 5.4:** Magnetic field/density phase diagram for the four simulations. The yellow line shows the average field for each logarithmic density bin. The color-scale shows the mass of gas in each bin of the phase diagram. The red dashed line shows a $\rho^{1/2}$ scaling (with normalization such that $\beta = 1$) while the red solid line shows a $\rho^{2/3}$ scaling of isotropic collapse. The white ‘x’ marks the value of the initial magnetic field strength and density in the box. Also marked is the critical density threshold $\rho_{\rm crit}$ where the gas pressure equals the background turbulent pressure. Finally, an approximate conversion from density to a length scale is shown in the collapsed region, based on a $\rho(r) = c_{\rm s}^2 G^{-1} r^{-2}$ profile. The inset shows the PDF of the collapsed gas density.

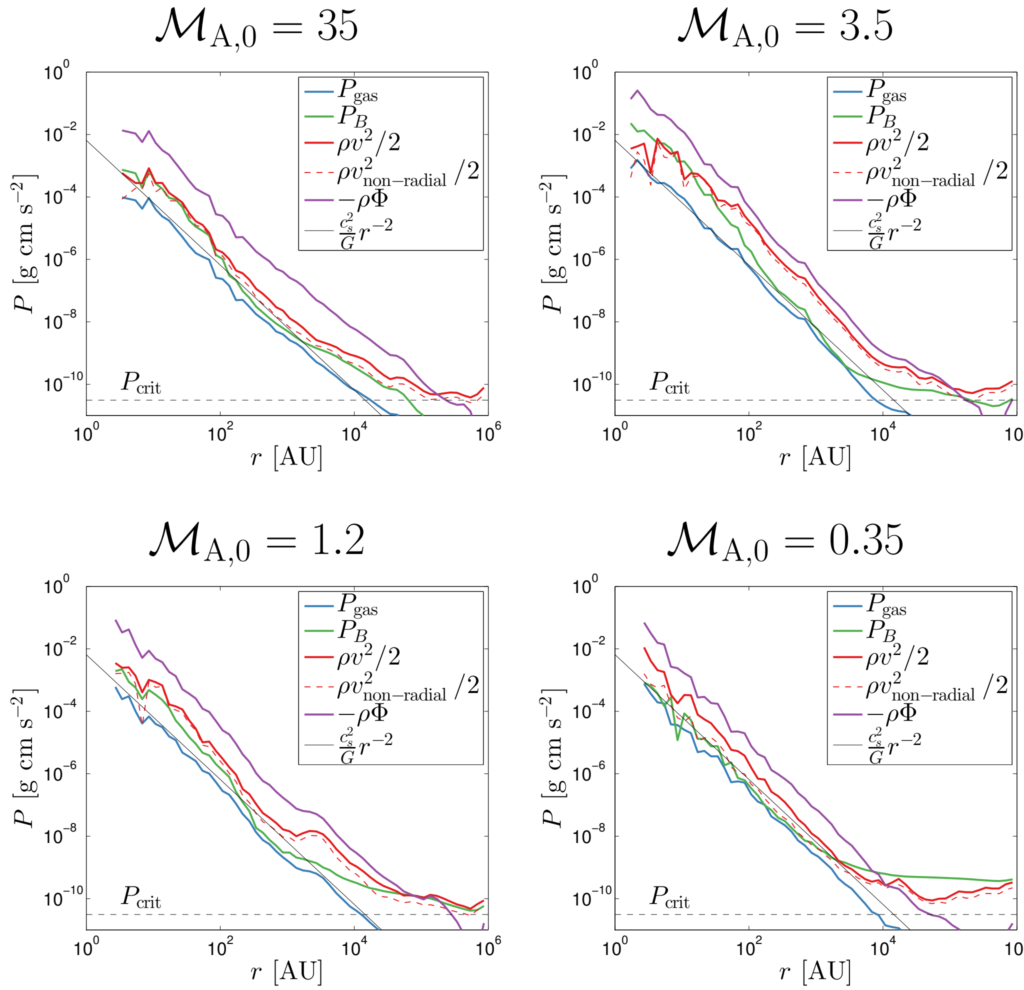

**Figure 5.5:** Radial profiles of the gas pressure, magnetic pressure, kinetic energy density (also its non-radial component), and gravitational potential energy density for the four simulations. These profiles have been calculated using volume-weighted averages of gas cells contributing to radial bins. Also shown is the $\rho(r) = c_{\mathrm{s}}^2 G^{-1} r^{-2}$ scaling, and the critical pressure $P_{\mathrm{crit}} = \rho_{\mathrm{crit}} c_{\mathrm{s}}^2$.

## 5.4 DENSITY-SCALING OF THE MAGNETIC FIELD

The relationship between density and magnetic field is important for theoretical models and observations. $B \propto \rho^{2/3}$ is predicted for collapsing clouds with weak magnetic fields (i.e., gravitational energy dominating magnetic energy). The same scaling is also predicted for flux-frozen, isotropic collapse in general. Lazarian et al. (2012) interpreted the observed $B \propto \rho^{2/3}$ from Zeeman measurements as a signature of reconnection diffusion being most efficient at lower densities (i.e. before collapse proceeds) in the weak field limit. In contrast, theoretical predictions for anisotropic contraction models, often expected in the strong field limit, predict a weaker scaling: $B \propto \rho^{1/2}$ (Tritsis et al. 2015).

We test the density magnetic field scaling relationship using our high dynamic range AREPO simulations. We plot the occupation of the gas in the density/magnetic field phase diagram for our simulations in Figure 5.4. The collapse occurs where the gas is compressed by turbulence above the critical density $\rho_{\rm crit} = \langle\rho\rangle\mathcal{M}_{\rm s}^2/3$ which is defined as the density at which the background level of turbulent pressure is sub-dominant to the gas pressure (Krumholz & McKee 2005; Li et al. 2015b). That is, the critical pressure is obtained by equating $P_{\rm turb} = \frac{1}{3}\langle\rho\rangle v_{\rm rms}^2$ with $P_{\rm gas} = \rho c_{\rm s}^2$. Note this is not a strict condition for collapse, but is a necessary requirement. Figure 5.4 shows a moving-average of the $B$-$\rho$ correlation (yellow). The best-fit slope with 95 per cent confidence intervals to relation at $\rho > 500\rho_{\rm crit}$ are listed in Table 5.2. We find that when the mean-field is subdominant ($\mathcal{M}_{\rm A,0} > 1$), the collapse follows an approximately isotropic collapse, which is characterized by $B \propto \rho^{2/3}$. But in the strong-field case ($\mathcal{M}_{\rm A,0} = 0.35$) the collapse is anisotropic with $B \propto \rho^{1/2}$ and $\beta \approx 1$.

In Figure 5.4 we also show inset-plots of the probability distribution function (PDF) of the gas density, which exhibits a log-normal distribution (indicative of turbulence, see Vazquez-Semadeni et al. 1997; Burkhart et al. 2009; Federrath et al. 2008) and a $\rho^{-3/2}$ powerlaw tail (indicative of gravitational collapse see, Kritsuk et al. (2007); Collins et al. (2012)). We find the critical density corresponds to the transition point between lognormal (diffuse turbulent gas) and power-law (self-gravitating) PDFs in these AREPO simulations, as observed also in Li et al. (2015b). Krumholz & McKee (2005) showed that the critical density was the condition for a clump to be self-gravitating. Recently Burkhart et al. (2016) worked out an analytic theory for the transition point between lognormal to powerlaw (which is termed the 'post-shock density' in that work).

## 5.5 COLLAPSE PROFILES

Figure 5.5 shows the volume-weighted core profiles from our simulations. The gas pressure, and hence density (since $P = \rho c_{\rm s}^2$, $c_{\rm s}$ a constant), follow a $r^{-2}$ power-law, as predicted by the simple analytic theory of isothermal spherical collapse which does not consider turbulence or the magnetic field (Larson 1969; Shu 1977). This scaling is seen even in our strong magnetic field simulation. This allows us to define a relation between the density in the core and physical scale as: $\rho(r) = c_{\rm s}^2 G^{-1} r^{-2}$. Note that the normalization (multiplicative prefactor) of this relation in our simulations is very close to unity, which is different from the non-magnetic, non-turbulent singular isothermal sphere, which has normalization $1/(2\pi) \simeq 0.16$. Fits to the normalizations for our four (strong→weak) simulations are: $0.46$, $0.60$, $0.83$, $0.58$ (95 per cent errors to the fits are $\pm 0.1$). The normalization is somewhat close to the similarity solutions of spherically symmetric collapse solved numerically by Penston (1969); Larson (1969), which have normalization $8.86/(4\pi) \simeq 0.71$. The core profiles extend all the way out to the critical pressure value $P_{\text{crit}} = \rho_{\text{crit}} c_{\text{s}}^2$ (beyond this the large-scale turbulent pressure exceeds the gas pressure; i.e., the size of a thermally supported core is about the sonic length). In all cases, we find the outer part ($\sim 10^4$ AU) of the profile has a plasma-beta of $\beta \sim 1$ (note the ratio of blue and green lines in the Figure gives $\beta$). This is to be expected for $\mathcal{M}_{\text{A},0} > 1$ since the local Alfvén Mach number in the turbulence is of order unity, so $P_B \sim \rho\sigma_{\text{nt}}^2 \sim \rho c_{\text{s}}^2$ at the sonic length. For $\mathcal{M}_{\text{A},0} = 0.35$, the turbulence does not significantly affect the field, so $B$ remains nearly constant until the gas pressure grows to the point that it is comparable to the field pressure; thereafter, the collapse proceeds anisotropically with $B \propto \rho^{1/2}$, thus $\beta$ remains close to unity all the way to the center of the core. However, if the mean magnetic field is subdominant to the kinetic energy density ($\mathcal{M}_{\text{A},0} > 1$) then the magnetic field grows faster towards the center (since $B \propto \rho^{2/3}$). We also plot the kinetic energy density profile (and its non-radial component), which dominates over the gas pressure. Our cores have not formed any disks on these scales (there is no evidence of a Keplerian rotation profile); the non-radial component of the kinetic energy density originates from the large-scale turbulent motions. In weak mean-field cases ($\mathcal{M}_{\text{A},0} > 1$), the magnetic field, growing faster than the other quantities towards the center, is in near equipartition with the kinetic energy density at the center. The collapse is in approximate Virial equilibrium, which is an assumption used in the turbulent core model (McLaughlin & Pudritz 1997; McKee & Tan 2003) and in the turbulent collapse model of Murray & Chang (2015). It should be noted these latter authors considered cores that are dominated by turbulent pressure rather than thermal pressure. For such cores, McKee & Tan (2003) found an $r^{-3/2}$ profile from observations of star-forming regions, and Murray & Chang (2015) inferred such a profile in the vicinity of a protostar from theory.

The normalized mass-to-flux ratios in our cores have evolved from the initial value of the box to: $\mu_{\Phi,0} : 80 \rightarrow 12.7$, $8 \rightarrow 16.5$, $2.7 \rightarrow 12.1$, $0.8 \rightarrow 5.8$ at a core-size of $10^4$ AU. This is consistent with reconnection diffusion in our simulations. The mass-to-flux ratio cannot increase under flux-frozen, ideal-MHD conditions. Our strong-field simulation is originally subcritical $\mu_{\Phi,0} = 0.8$, and the simulation should not allow collapse unless reconnection diffusion is present, which leads to a mass-to-flux ratio above unity. In the calculation of the mass-to-flux ratio, the volume-averaged magnetic field in a spherical region of diameter $10^4$ AU is used. We note that the transition from sub-critical ISM clouds to super-critical cores is observed via 21-cm, OH and CN Zeeman observations and that no sub-critical cores are observed in the sample of Crutcher et al. (2010).

Reconnection in our numerical simulations is enabled by numerical resistivity, but in this fast turbulent reconnection diffusion regime the simulation mimics the actual physical process because the reconnection rate is independent of the strength of the resistivity (Kowal et al. 2009). Previous studies have found mass-to-flux ratios numerically converged with resolution (Li et al. 2015b), supporting the idea that a simulation with resolution such as ours captures the physical process accurately.

## 5.6 DISCUSSION

We have presented basic scaling relationships of density and magnetic field, and radial profiles, obtained from novel high-resolution simulations, important for both theoretical models and observations of star formation. In a sense, the simulations advance the simple spherical, self-similar isothermal analytic collapse model (Larson 1969; Shu 1977), with the inclusion of full 3D effects of magneto-turbulence. The classic $r^{-2}$ radially-averaged pressure profile scaling is still recovered in all cases, with similar normalization across simulations. The same $r^{-2}$ scaling is seen in simulations of turbulence-dominated, nearly isothermal atomic cooling halos in Becerra et al. (2015). Our simulations do not show inside-out collapse, which would lead to a $r^{-3/2}$ profile (Shu 1977). We point out that we stop the simulations before we would expect stars to form, meaning, our cores are pre-stellar. Thus we do not yet see a $r^{-3/2}$ scaling in the vicinity of the star (inside the sphere of influence, after the star forms), as predicted by turbulent models for star formation in compact massive clouds from non-hydrostatic initial conditions of Murray & Chang (2015), and as observed in the simulation setup of Murray et al. (2015).

Collapse in the turbulent medium occurs where the gas pressure exceeds the background turbulent pressure; i.e., above the critical density $\rho_{\rm crit}$. At these outer-scales of collapse, we find the plasma beta is always near unity regardless of mean-field strength, indicating equipartition between the magnetic and gas pressures in the turbulent environment. A plasma beta near unity occurs in the $\mathcal{M}_{\rm A,0} > 1$ simulations because in the turbulent (uncollapsed) environment the magnetic field and density are not well correlated, instead the local Alfvén Mach number in the turbulence is of order unity, so at the sonic length $P_B \sim \rho\sigma_{\rm nt}^2 \sim \rho c_{\rm s}^2$. In the strong-field regime, the field strength is not affected much by turbulence, so $B$ remains nearly constant until the gas pressure grows to the point that it is comparable to the field pressure (which happens at the tail of the log-normal distribution of density which develops from turbulence).

Anisotropic collapse with $B \propto \rho^{1/2}$ is exhibited in the sub-Alfvénic simulation, and we form cores with a classic hourglass-like magnetic field morphology, similar to NGC 6334 (Li et al. 2015a). But when the mean-field is weak ($\mathcal{M}_{\rm A,0} > 1$), the collapse is spherical and hence $B \propto \rho^{2/3}$, which means that the plasma beta decreases toward the center. Interestingly, due to the $B \propto \rho^{2/3}$ scaling, the weak-field case actually allows for a stronger magnetic field in the core than in the strong-field ($\mathcal{M}_{\rm A,0} = 0.35$) case, where the magnetic field does not rise as fast with density. Constant plasma beta self-similarity in the collapse is broken in the weak-field case. There are two clear regimes of magnetic field evolution we observe, but we do not mean to conclude or imply that the transition is very sharp, occurring exactly at $\mathcal{M}_{\rm A,0} = 1$.

Even if the initial large-scale mean-field is weak, turbulence amplifies it considerably prior to collapse. We attribute the decrease in plasma beta in the super-Alfvénic simulations as a result of the small-scale turbulent dynamo process. Our simulations show the initial plasma beta evolves as: $\langle\beta\rangle\ :\ 0.0025\ \rightarrow\ 0.0025, 0.028\ \rightarrow\ 0.025, 0.25\ \rightarrow\ 0.064, 25\ \rightarrow\ 3.2;$

i.e., the initial plasma beta shrinks in the super-Alfvénic cases. The average plasma beta is not increased significantly in the strong mean magnetic field run by turbulence. We note all simulations are driven with the same amplitude, with sonic Mach number 10. The small-scale turbulent dynamo is very efficient in amplifying the magnetic field and may in fact be more efficient in the super-Alfvénic limit (Cho et al. 2009).

As the turbulent simulations evolve and collapse, magnetic field is generated by the stretching and twisting of magnetic field lines and through flux conservation. However, turbulence also acts to remove field lines from collapsing regions via reconnection diffusion and the magnetic field changes its topology in just an eddy turn over time (Lazarian & Vishniac 1999; Vishniac et al. 2003; Lazarian et al. 2004). Once rapid collapse begins, reconnection diffusion, which depends only on the properties of turbulence/turbulence amplitude, removes magnetic field from the contracting clouds in competition with the amplification the field experiences due to contraction and dynamo processes. Future studies will determine how fast reconnection diffusion is compared to the dynamo process in such simulations in order to quantify the competition between flux removal and field amplification. Our simulations do show evidence for reconnection diffusion through the increase of the mass-to-flux ratios in the cores (§ 5.5).

We note that our results should be as applicable to observations as they are to theoretical predictions. In all the simulations, we transformed micro-Gauss level large-scale fields into milli-Gauss level core-scale fields, in agreement with various observational estimates of field-strengths (Crutcher et al. 2010; Girart et al. 2006, 2009; Stephens et al. 2013; Houde et al. 2016). Despite different scaling relationships and core morphologies between the sub- and super-Alfvénic simulations, all our simulations reproduce *similar* magnetic field strengths on core scales. The star formation process is imprinted with the self-similar nature of turbulence and gravitational collapse despite different initial environmental conditions. What sets formation with different mean-field strengths apart is the orientation of the mean-field on various length scales relative to the large-scale value (Figure 5.3). The orientation remains well-preserved to $100$ AU scales (ALMA resolution) *only* in our strong-field simulation ($\mathcal{M}_{\rm A,0} = 0.35$). If the magnetic field is moderately strong ($\mathcal{M}_{\rm A,0} \gtrsim 1$) then the mean-field only remains aligned to scales of $10000$ AU (resolution of the Combined Array for Research in Millimeter-wave Astronomy; CARMA). More precisely, the field remains aligned to less than $30$ degrees from its large-scale value down to scales of $10^{2.0}$ AU, $10^{3.7}$ AU, $10^{4.0}$ AU, $10^{5.5}$ AU for our four (strong→weak) simulations, as listed in Table 5.2.

Figure 5.3 shows the angle of magnetic field alignment averaged over the core as a function of scale, as well as the fraction of gas in a given radius that is aligned within 30 degrees of the large-scale mean-field. Table 5.2 also lists the fraction of gas aligned within 30 degrees of the large-scale mean-field on a scale of 10000 AU. The field is strongly correlated in the large-scale strong-field case and virtually uncorrelated if the large-scale mean-field is very weak. The correlation is in between for the intermediate mean-field cases. (Note the curves for $\mathcal{M}_{\rm A,0} = 1.2$ and $\mathcal{M}_{\rm A,0} = 3.5$ cross each other: there is a certain amount of variance to be expected in the correlation as function of $\mathcal{M}_{\rm A,0}$ for a large population of cores, which we do not have the statistics to probe in our current simulation because we focus on resolving single cores.) Observationally, Li et al. (2009) found a strong correlation between orientation on the 10000 AU scales and large scales, whereas Hull et al. (2014) did not for smaller scales. However, there is some ambiguity on the latter since it could be confused by toroidal wrapping in a disk, and CARMA also only provides a few independent polarization vectors, not enough to determine the mean-field direction with robust statistics. This makes ALMA paramount for the study of the importance of magnetic fields on scales less than 10000 AU.

We note that the magnetic field, which is found to be always strong in the core regardless of the large-scale value (local Alfvénic Mach number is order unity in the core), has a significant effect on the angular momentum of the accreting gas and thus on the properties of circumstellar, including protoplanetary, disks, that are to form. Future studies resolving the core collapse beyond the isothermal collapse stage will help explain the ultimate fate of the protostar. The present study serves as providing useful initial conditions to this problem. An interest of study is the 'magnetic braking catastrophe', where magnetic fields can in theory prevent the formation of circumstellar discs around young stars (e.g., see Wurster et al. (2016) and references therein). Our chaotic magnetic field morphologies in the weak mean-field simulations perhaps could be one way around the magnetic braking catastrophe, through the effects of flux loss via reconnection diffusion. The influence of turbulence in reducing magnetic torques has been examined in a number of papers (Seifried et al. 2012; Joos et al. 2013).

Our $B \propto \rho^{2/3}$ scaling relation for the weak-field simulations is in agreement with the Zeeman observations of diffuse and molecular clouds of Crutcher et al. (2010), which see $\langle B\rangle_M \propto \langle\rho\rangle^{0.65}$. We note, however, that the relationship between $B$ and $\rho$ in our simulations, as indicated by the moving-average fits (yellow lines) in Figure 5.4, shows the slope of the correlation transitioning from a flatter-than-$2/3$ value in the turbulent medium to the $2/3$ slope in the collapsed cores. The tight scaling of $B \propto \rho^{2/3}$ is seen on scales of $r = 10^3$-10 AU (i.e., $\rho > 500\rho_{\rm crit}$). The slope is actually closer to $B \propto \rho^{0.5}$ in the collapsed-regions with $\rho_{\rm crit} < \rho < 500\rho_{\rm crit}$, similar to the simulations of Collins et al. (2012). That is, we find that the slope is actually shallower than $2/3$ on scales of $r = 10^3$-$10^4$ AU due to the transitioning between the turbulent medium and cores. These scales are more relevant for the clump sizes observed in Crutcher et al. (2010) for deducing the observational scaling relation. Li et al. (2015b) carried out a more thorough analysis of reproducing the Crutcher et al. (2010) relation adding in all of the observational effects, including convolution with a beam size of $\sim$ 5000 AU. Taking density-averaged (as measured by Zeeman observations) as opposed to volume-averaged magnetic field strengths, Li et al. (2015b) found a value of $\alpha$ consistent with $0.65$ for a moderately strong initial magnetic field ($\mathcal{M}_{\rm A,0} = 1$) but only marginally so for a weak initial field ($\mathcal{M}_{\rm A,0} = 10$). In contrast, the $B$–$\rho$ relation measured on a cell by cell basis on these scales has a flatter power. This demonstrates the importance of adding observational effects to simulation results when interpreting data. Similarly, Li et al. (2015b) show that in the calculation of the mass-to-flux ratio of clumps, the average area-weighted (i.e., flux/area) field is somewhat less than the *observed* mass-averaged field, so that the actual mass to flux ratio is about $0.7$ times the value inferred from line-of-sight values, rather than (0.25-0.5) times the line-of-sight value, as is often used. Again this signifies the importance of putting simulation data through an observational pipeline.

Our simulations also demonstrate the importance of having a high-dynamic range calculation. The theoretically expected scaling of $B \propto \rho^{2/3}$ in magnetic field density phase-space is accurately resolved by being able to simulate scales of $r = 10^3$-10 AU; i.e., convergence of the slope of the relation is achieved on the smallest scales; on larger scales the slope is flatter as it transitions to the uncollapsed background turbulent environment. In contrast, previous AMR simulations of this type have resolved down to scales of 120 AU Collins et al. (2012) and 500 AU Li et al. (2015b). Our simulations are expected to have less numerical magnetic reconnection (which can remove magnetic flux and affect the scaling relation) as well as significantly reduced advection errors (which can be quite significant in supersonic flows) due to the quasi-Lagrangian nature of the moving-mesh formulation.

Comparing with the results of various observation of the ISM (e.g. Crutcher et al. 2010 and Li et al. 2015a), our simulations suggest that $\mathcal{M}_{\rm A,0} \sim 1$ may be typical in many ISM regions (where '$\sim$' means the coefficient of the relation is unconstrained by an order of magnitude). The magnetic field is often observed to be coherent on large-scales and the density structure is filamentary (thus we do not expect $\mathcal{M}_{\rm A,0} \gg 1$). Our simulations suggest that the existing observations for star formation provide evidence that the collapse occurs in *both* the regimes $\mathcal{M}_{\rm A,0} \gtrsim 1$ and $\mathcal{M}_{\rm A,0} \lesssim 1$. The former is supported by $\langle B \rangle_M \propto \langle \rho \rangle^{0.65}$ Zeeman splitting observations of dense molecular cloud clumps (Crutcher et al. 2010) while the latter is supported by multiple observations of NGC 6334, which show self-similar, aligned magnetic field structure from 100 pc to 0.01 pc scales with $B \propto \rho^{0.41}$ (Li et al. 2015a). This is assuming that the determination of the slope of the magnetic field density relation in Li et al. (2015a) is robust to the indirect methods used. Note, we do not claim that the transition between regimes occurs as a *sharp* transition at $\mathcal{M}_{\mathrm{A},0} = 1$, just that two different regimes of magnetic field evolution (under the ideal MHD assumptions) exist.

Regions in the ISM with stronger magnetic fields may have suppressed star formation. This is seen in the strong-field box, which takes longer to collapse and form the first core because it is initially slightly sub-critical and requires turbulent reconnection to reach criticality to collapse under self-gravity. Even in the other simulations, the time of the collapse of the first core correlates weakly with magnetic field strength, because the magnetic field provides extra pressure support against collapse. This effect may have relevance for the star formation in the galactic center, where star formation is observed to be suppressed and the magnetic field is strong: $500~\mu\mathrm{G}$–$5\mathrm{mG}$ (Pillai et al. 2016; Kauffmann 2016).

We discuss the caveat that turbulent collapsing simulations such as ours generate hundreds of cores over a single free-fall timescale. However, our simulation strategy was to resolve features on $< 100~\mathrm{AU}$ scales (relevant for ALMA observations) and therefore we did not impose any minimum spatial resolution or sink particles. This comes with a trade-off, however: the timestep of the simulation decreases exponentially as the first core forms, thus we are only able to resolve (at $< 100~\mathrm{AU}$) the first-prestellar core that collapses, which happens early on, at $< 0.4 t_{\mathrm{ff}}$. We are not able to say much about a large statistical sample of collapsed cores in the present work, because most cores have not yet collapsed to such spatial scales. Importantly, however, the collapsed cores we investigate are not outliers from a powerlaw distribution of masses, as they all have similar masses. (Their core masses are also not extreme compared to the masses of the other turbulently fragmented cores in the box which are at an earlier stage of collapse; see Section 5.8.). It is plausible that certain geometries (e.g. relative orientation between the magnetic field and angular momentum vector) would collapse first in a turbulent medium, so there could be other types of bias present in the types of cores that collapse first. We defer analysis of a statistical sample of cores to upcoming future work, in which we will modify our simulation strategy and trade-off resolution and the capture of the exact collapse process with the use of sink particles.

## 5.7 CONCLUSIONS

We have simulated the formation of pre-stellar cores in a supersonic, turbulent, magnetic interstellar medium under self-gravity, resolving the initial isothermal collapse phase down to a few AU, relevant for future ALMA polarization observations of Class 0 protostars. We studied the effects of the mean-field strength, and have arrived at the following main conclusions:

- If the turbulent kinetic energy density of the ISM dominates over the mean-field magnetic pressure, then collapse occurs approximately isotropically on small scales ($r < 10^4$ AU), with $B \propto \rho^{2/3}$. But in the case of strong large-scale magnetic field, the collapse is anisotropic with $B \propto \rho^{1/2}$.
- On the larger scales of collapsed cores ($r > 10^4$ AU), the scaling of magnetic field with gas density (looking at it on a simulation cell-by-cell basis) is flatter, close to $B \propto \rho^{1/2}$ in all cases, as the gas transitions to the turbulent background medium. The results of Li et al. (2015b) show that if one instead looks at the scaling of the *density-averaged* magnetic field (convolved with the telescope beam) $\langle B\rangle_M$ with $\langle\rho\rangle$, the slope of the correlation is steeper, closer to $0.64$. Crutcher et al. (2010) observe cores have $\langle B\rangle_M \propto \langle\rho\rangle^{0.65}$ via Zeeman splitting measurements on scales of $r > 10^4$ AU. This highlights the importance of modeling observational biases when interpreting physical results and comparing observations with simulations.

- Our simulations of collapsing pre-stellar cores all follow similar radially-averaged $r^{-2}$ profiles (as predicted by analytic spherical isothermal collapse model), regardless of mean-field strength. In the weak-field case, even though the collapse is isotropic, the $B \propto \rho^{2/3}$ scaling means the collapse is not self-similar in the sense that $\beta \equiv P_{\rm gas}/P_B$ decreases towards the center and the Alfvénic Mach number also drops with radius. These quantities are approximately constant in the case of strong-field collapse. Collapse occurs in approximate Virial equilibrium.

- Regardless of cloud scale mean-field strength, the outer regions ($\sim 10^4$ AU) of the cores have $\beta \sim 1$ and the magnetic field reaches equipartition with the thermal energy, which in turn is comparable to the average kinetic energy density in the simulation box.

- The magnetic field in the center of the cores is actually slightly stronger (by about a factor 3 on 100 AU scales) if the large-scale mean-field is weaker than the turbulent kinetic energy density because of the $B \propto \rho^{2/3}$ scaling as opposed to $B \propto \rho^{1/2}$.

- The mass-to-flux ratios in our cores increase by a factor of a few from the large-scale value, indicating fast reconnection diffusion.

- If the large (pc) scale mean-field is subdominant to the turbulent kinetic energy density ($\mathcal{M}_{\rm A,0} > 1$), then the magnetic field on 100 AU core scales has uncorrelated direction with the mean-field (although may still be correlated on larger core scales $\sim 0.1$ pc). If the field is strong, the field direction remains correlated on all scales, and has a classic hourglass-like morphology. Correlation on intermediate scales (10000 AU) is a function of $\mathcal{M}_{\rm A,0}$, ranging from strongly correlated ($\mathcal{M}_{\rm A,0} = 0.35$) to virtually no correlation ($\mathcal{M}_{\rm A,0} = 35$) as shown in Figure 5.3. The fact that correlation extends to smaller scales as $\mathcal{M}_{\rm A,0}$ decreases makes future ALMA observations very useful for constraining $\mathcal{M}_{\rm A,0}$ of the ISM.

- In terms of upcoming directions/opportunities in this subfield, observationally quantifying the scale at which the orientation correlation drops in a statistically significant sample of molecular cloud cores will be very useful in improving our knowledge of the ISM.

## 5.8 TURBULENT FRAGMENTATION IN SIMULATIONS

Turbulent fragmentation leads to the collapse of hundreds of cores inside our simulation volume, as has been seen previously (Collins et al. 2011, 2012; Li et al. 2015b). In this paper, we have focused our simulation efforts on capturing the collapse of the first core that forms. Here we compare some of the properties of these cores to the larger samples of pre-stellar cores in our boxes, which are at an earlier stage of collapse (typically the core has only collapsed to scales of $10^3$ AU). Cores are identified by selecting local maxima of the density field within a radius of $1500$ AU.

The analysis allows us to learn about how wide spread is the existence of hourglass figures. Figure 5.6 shows the field morphologies for the $9$ most-collapsed cores in each of the simulations. We see that in the case of a strong magnetic field ($\mathcal{M}_\mathrm{A} = 0.35$) the field lines align well with the mean-field direction. The morphologies are mostly linear on this scale, with some amount of pinching towards the core, and are likely to form hourglass shapes as the cores continue to collapse. But in the case of the simulations where the turbulent kinetic energy dominates the magnetic field, the morphologies can be quite chaotic on scales of $1000$ AU, even in some of the less-collapsed cores. Therefore, the hourglass shape may be uncommon in such environments. The possibility of hourglass shapes is not excluded, however: a few cores show fairly linear morphologies with small amount of pinching towards the core center, which may end up evolving into an hourglass shape.

We also look at how the first-collapsed cores in each simulation compare to a larger sample of turbulent fragmentation cores. Figure 5.7 shows the radial density profiles of the $30$ most-collapsed cores in each of the simulations. We see that there is variation among the normalization of the core profiles (as expected, since the turbulent fragmentation process is known to yield a powerlaw distribution of masses). The first-collapsed cores are not outliers in terms of their total mass. From Figure 5.7 we see that some of the less-collapsed cores have a density profile shallower than $\rho \propto r^{-2}$ towards their centers; but reach $\rho \propto r^{-2}$ as they collapse further. This is true regardless of the mean-field strength.

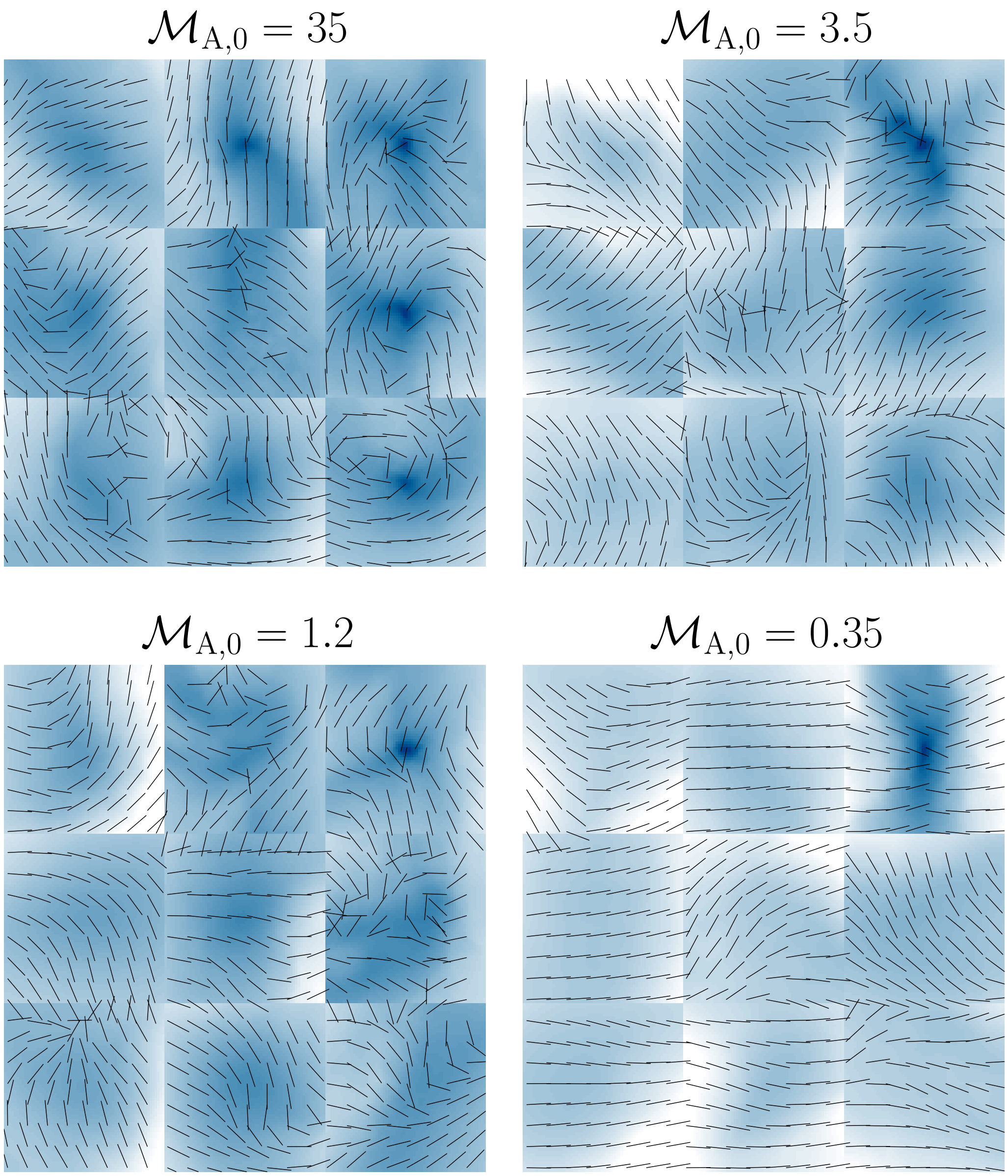

**Figure 5.6:** Magnetic field and density projections of the $9$ most-collapsed cores in each of the simulations. Similar to Figure 5.1. When the field is strong ($\mathcal{M}_{\rm A} = 0.35$) the magnetic field aligns well with the mean-field and shows simple structure. In the other cases, there is evidence for chaotic field morphology even in some of the less-collapsed cores.

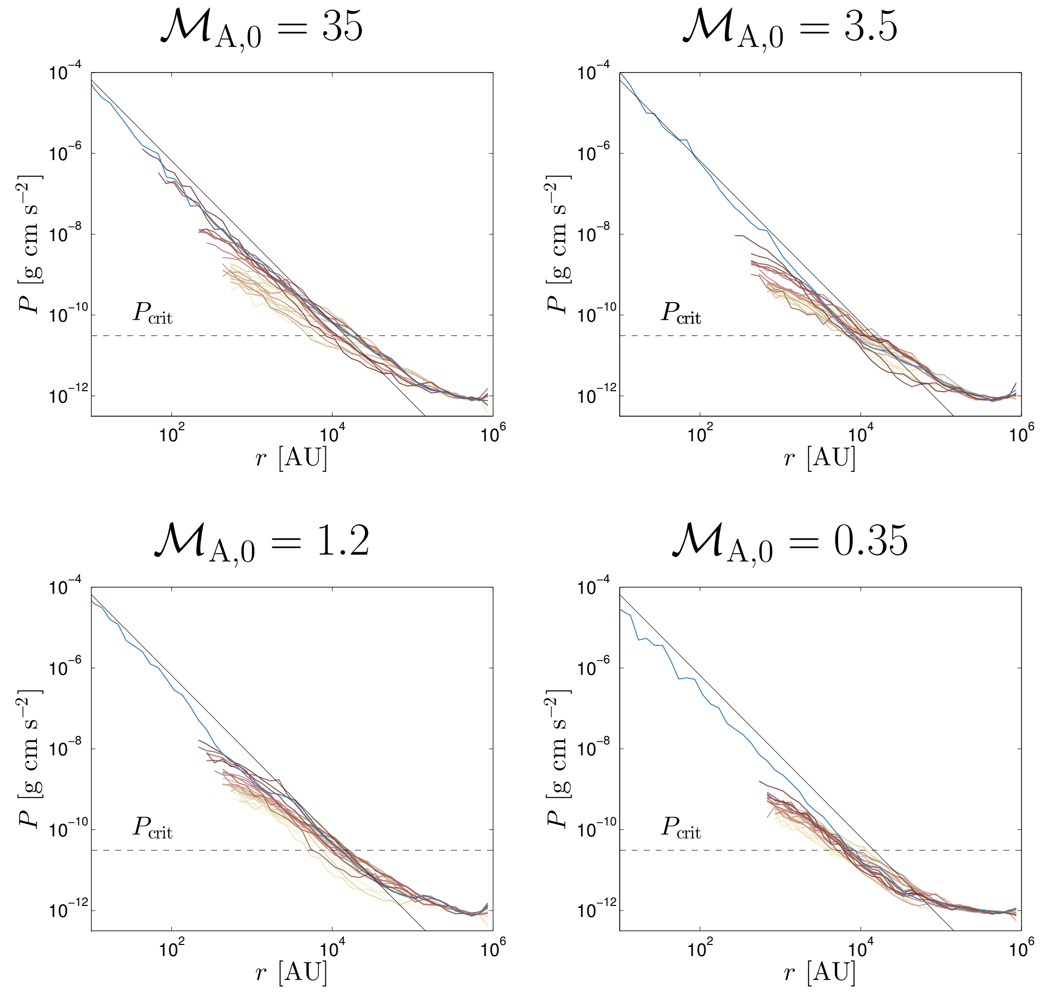

**Figure 5.7:** Radial profiles of the density (plotted as gas pressure $P_{\rm gas} = \rho c_{\rm s}^2$) for the $30$ most-collapsed cores in each of the simulations. Similar to Figure 5.5. The most collapsed core in each simulation, which we analyzed in this work, is plotted in blue.

*I decided that if I could paint that flower in a huge scale, you could not ignore its beauty.*

Georgia O'Keeffe

# 6

# Moving mesh simulations of cosmological magnetic fields

– based on –

Marinacci, F., Vogelsberger, M., Mocz, P., & Pakmor, R. (2015). The large-scale properties of simulated cosmological magnetic fields. *MNRAS*, 453, 3999–4019.

We perform large-scale cosmological simulations with a primordial magnetic field using the moving mesh code AREPO. We run simulations featuring the fiducial feedback model of the ILLUSTRIS simulation as well as runs with adiabatic gas physics only. We also test the significance of the initial seed field strength. Magnetic field amplification initially follows a $B \propto \rho^{2/3}$ law due flux-freezing under isotropic collapse. Shear flows and turbulence enhances amplification at high baryon overdensities. Radiative cooling and feedback further help amplify the field, and the field strength saturates to equipartition values inside halos (reaching $10 - 100\ \mu$G) with tangled morphology, erasing information about the primordial seed field strength.

## 6.1 INTRODUCTION

Magnetic fields are known to play a key role in many small scale astrophysical systems: from star formation (Crutcher et al. 2010) to accretion onto compact objects (Balbus 2003) to relativistic jets (Blandford & Znajek 1977) to particle acceleration via the Fermi mechanism (Fermi 1949) to radio lobes and halos in galaxy clusters (Fabian et al. 2002) and more.

The existence of magnetic fields beyond the scale of halos is poorly constrained, however. Indirect constraints of an intergalactic seed field of $B > 3 \times 10^{-16}$ G come from the non-observation of GeV gamma-ray emission from electromagnetic cascade initiated by tera-electron volt gamma rays in intergalactic medium (Neronov & Vovk 2010). Intergalactic magnetic fields are thought to be weak and dynamically unimportant ($B < 10^{-9}$ G) which makes detection in low density regions difficult. They are at or below the detection limit of the current instrumentation, even though this should improve with the next generation of radio instruments such as SKA (Beck 2007). The magnetic field would become dynamically important for cosmological structure formation at around $B = 10^{-9}$ G.

As such is the current state of observations, numerical simulations play a vital role in making observational predictions, by offering guidance to observational strategies and giving an understanding of how we could learn whether cosmological magnetic fields are of primordial origin or generated inside galaxies. Magnetogenesis is the theoretical process under which seed magnetic fields may be generated during inflation (Widrow et al. 2012). Alternatively the Biermann battery mechanism (Biermann 1950) may operate at cosmological accretion shocks to generate magnetic fields from nothing (Ryu et al. 1998a), or at cosmological ionization fronts during reionization (Gnedin et al. 2000).

Here we study the effects of a very week seed magnetic field on cosmological (25 Mpc) scales using simulations. The goal is to study the general properties of cosmological magnetic fields, the dependence on the initial feed strength, the coupling to full physics baryonic feedback, and the amplification by turbulence. In Section 6.2 we describe the numerical setup. Section 6.3 discusses the large-scale properties of the magnetic field in the cosmological volume. Some properties at the individual halo scale are presented in Section 6.4. In Section 6.5 we offer discussion and concluding remarks.

## 6.2 NUMERICAL SETUP

We simulate $25h^{-1}$ Mpc cosmological volumes using the AREPO code with the ILLUSTRIS feedback model (Vogelsberger et al. 2014b,a), some of which have been presented in Chapter 3.

The simulations have resolutions of $2 \times 256^3$ particles. They consider a standard $\Lambda$ cold dark matter ($\Lambda$CDM) cosmology, with the most recent cosmological parameters deduced from *Planck* (Spergel et al. 2015). The simulations are started at $z = 127$ using the transfer function computed with CAMB (Lewis & Bridle 2002).

The moving mesh code AREPO (Springel 2010) solves self-gravitating collisionless dynamics via a standard TreePM method, splitting the gravitational force into a long range and short range contribution. The long range contribution is calculated in Fourier space on a mesh, and the short-range contribution is found using an oct-tree algorithm. The fluid equations are solved in finite-volume form on a discretized unstructured Voronoi tessellation that moves with the fluid motions. To evolve the magnetic field, the constraint transport algorithm of Mocz et al. (2016) is used.

In ideal MHD, the volume averaged mean-field is an invariant and there are no source terms in the equation; therefore it is impossible to generate magnetic fields out of nothing. Therefore, in these simulations we consider the effect of a small uniform primordial magnetic field present at $z = 127$. We investigate how the initial strength of the field impacts the evolution to the present time at $z = 0$.

The galaxy formation physics used in the simulations are those specifically developed for the *Illustris* simulations, initially presented in Vogelsberger et al. (2013). The model is calibrated against the cosmic star formation history and the galaxy stellar mass function, and is able to reproduce a wide range of observed galaxy properties and statistics at $z = 0$.

We present 3 simulations here. The 3 simulations are [1] adiabatic and [2] full physics runs with an initial (weak) seed field of $B = 10^{-14}$ G, and [3] a full physics run with stronger initial seed field ($B = 10^{-10}$ G). Additional simulations with varied parameters may be found in Marinacci et al. (2015), supporting the same picture presented here (those simulations were performed with the Powell scheme). The magnetic fields quoted here are the physical magnetic field strengths rescaled to $z = 0$ to factor out the effects of cosmological expansion: $\mathbf{B} = \mathbf{B}_0/a^2$, where $a = (1+z)^{-1}$ is the cosmological expansion factor, and $\mathbf{B}_0$ is the rescaled intensity of the $B$-field at $z = 0$.

## 6.3 LARGE-SCALE PROPERTIES

We begin by analyzing the large-scale properties of the magnetic field in a cosmological volume, looking at the correlation between magnetic field intensity and density. Figure 6.1 shows a slice of density in the box in our 3 simulations (adiabatic weak seed, full physics weak seed, full physics stronger seed). Slices are shown at redshifts $z = 2$ and at $z = 0.2$. Figure 6.2 shows the magnetic field strength in the same slices. What is clearly evident from the visualizations is that the magnetic field traces the cosmic density structure. The strongest

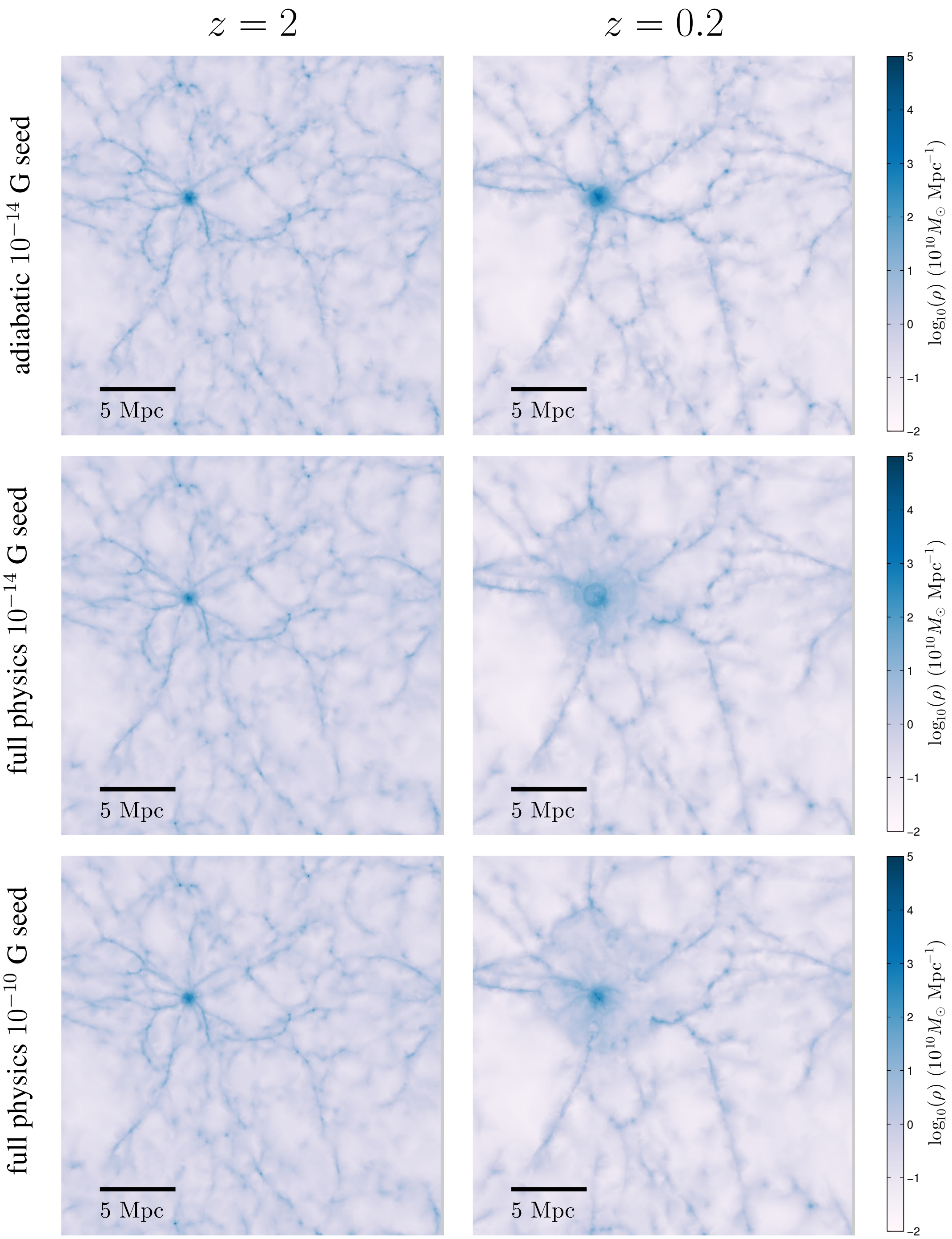

**Figure 6.1:** Slices of density at $z = 2$ and $z = 0.2$ for the 3 simulations.

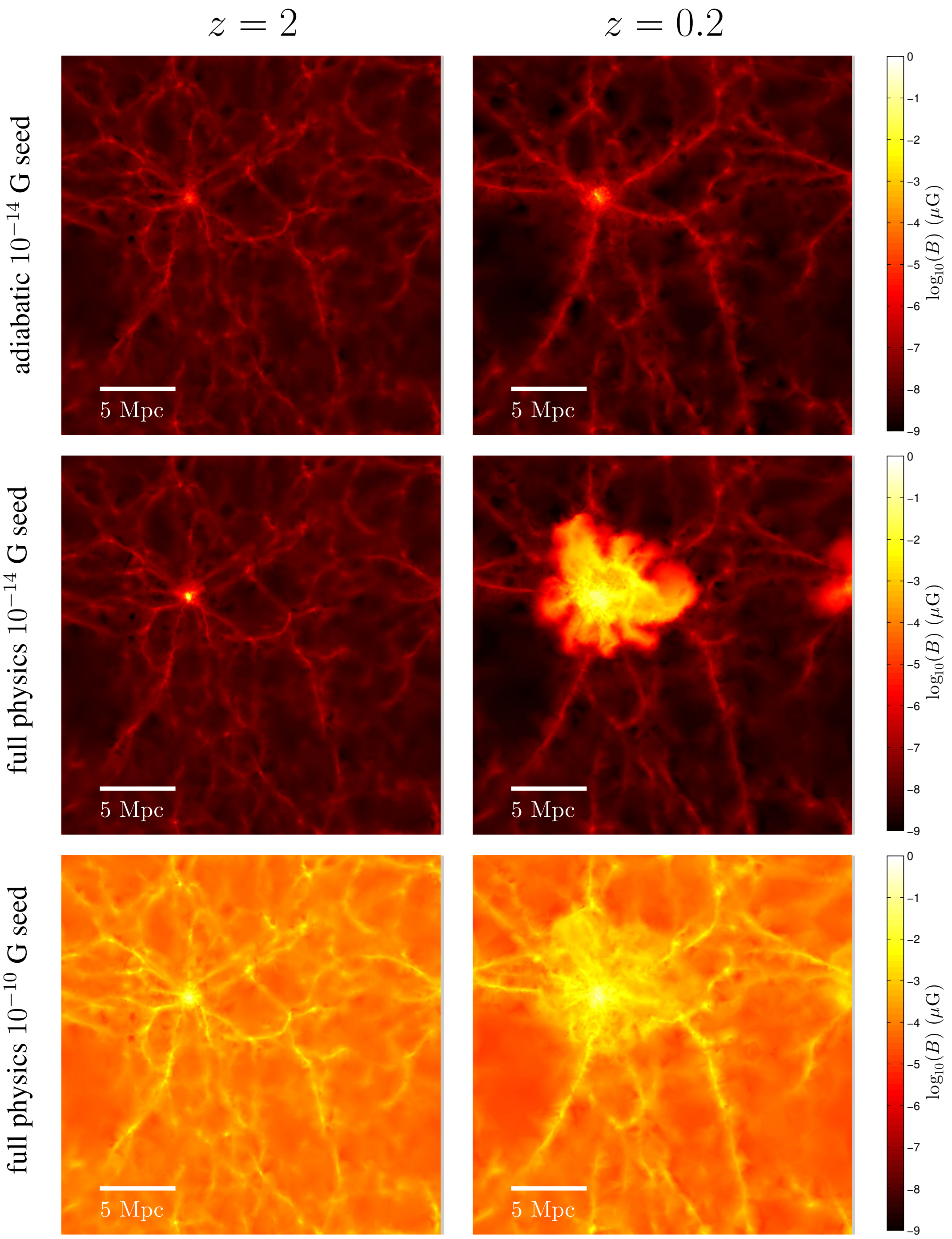

**Figure 6.2:** Slices of the magnetic field strength at $z = 2$ and $z = 0.2$ for the 3 simulations. Compare with Figure 6.1, the magnetic field strengths are seen to trace cosmic structure.

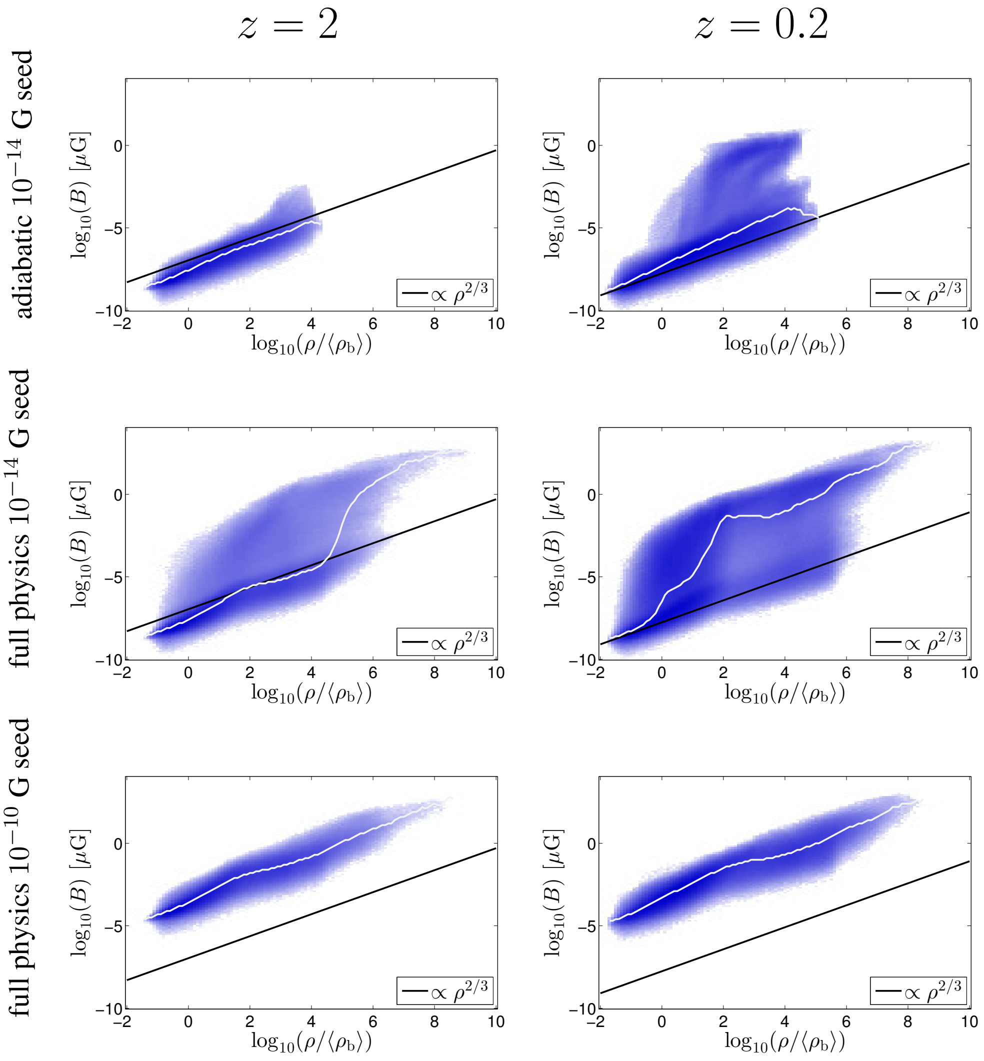

**Figure 6.3:** Distribution of the magnetic field strength as a function of density. Homogeneous contraction with flux freezing predicts a $B \propto \rho^{2/3}$ scaling. Cosmic expansion reduces the normalization of the physical magnetic field strength with time by a factor of $(1+z)^{-2}$. Small scale turbulence and shearing motions in the full physics runs are seen to saturate the magnetic field at high overdensities irrespective of initial field strength.

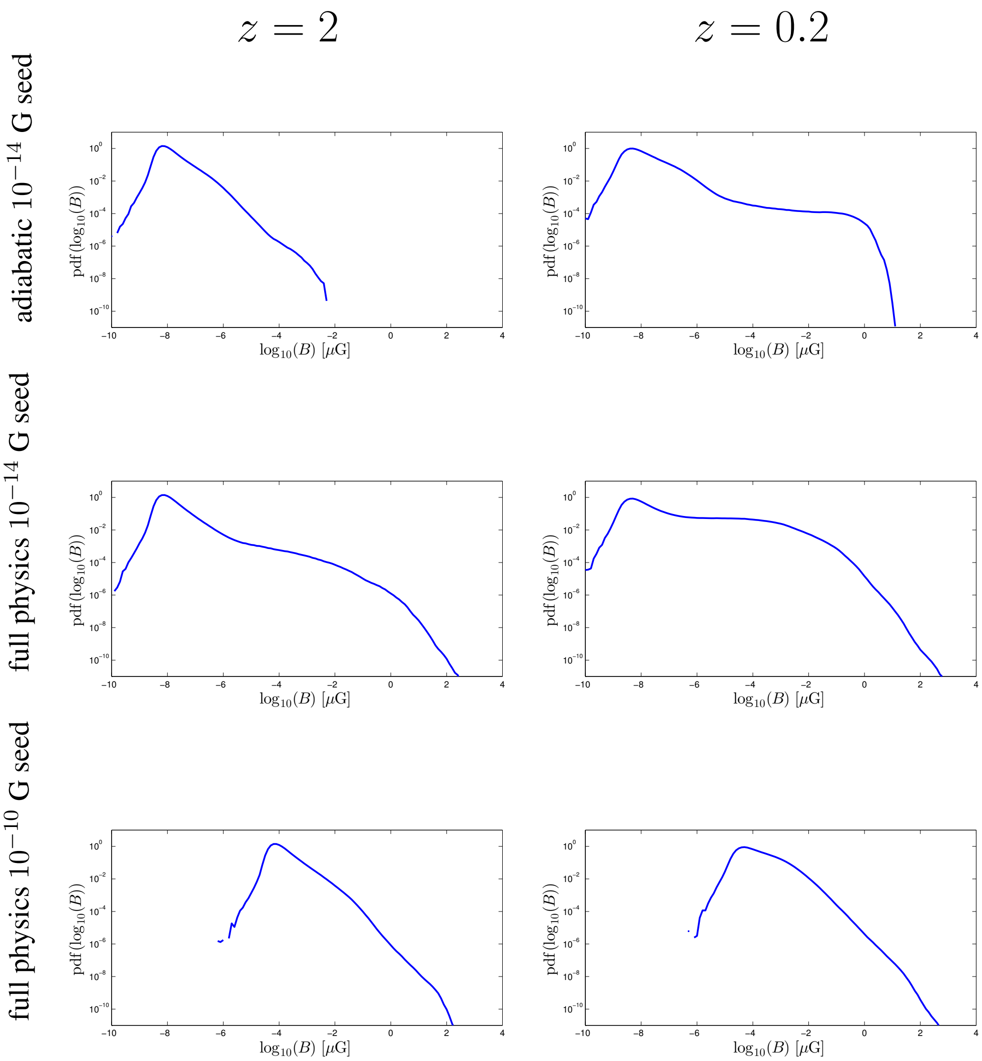

**Figure 6.4:** Probability density distribution of magnetic field strengths in the 3 simulations at redshifts $z = 2$ and $z = 0.2$. Low magnetic field values are found in cosmic voids and filaments and the distribution between adiabatic and full physics runs is unchanged. The high end of the distribution is stretched due to additional amplification in the full physics runs. The high end distribution is very similar for both full physics runs with very weak ($10^{-14}$ G) and weak ($10^{-10}$ G) seed fields.

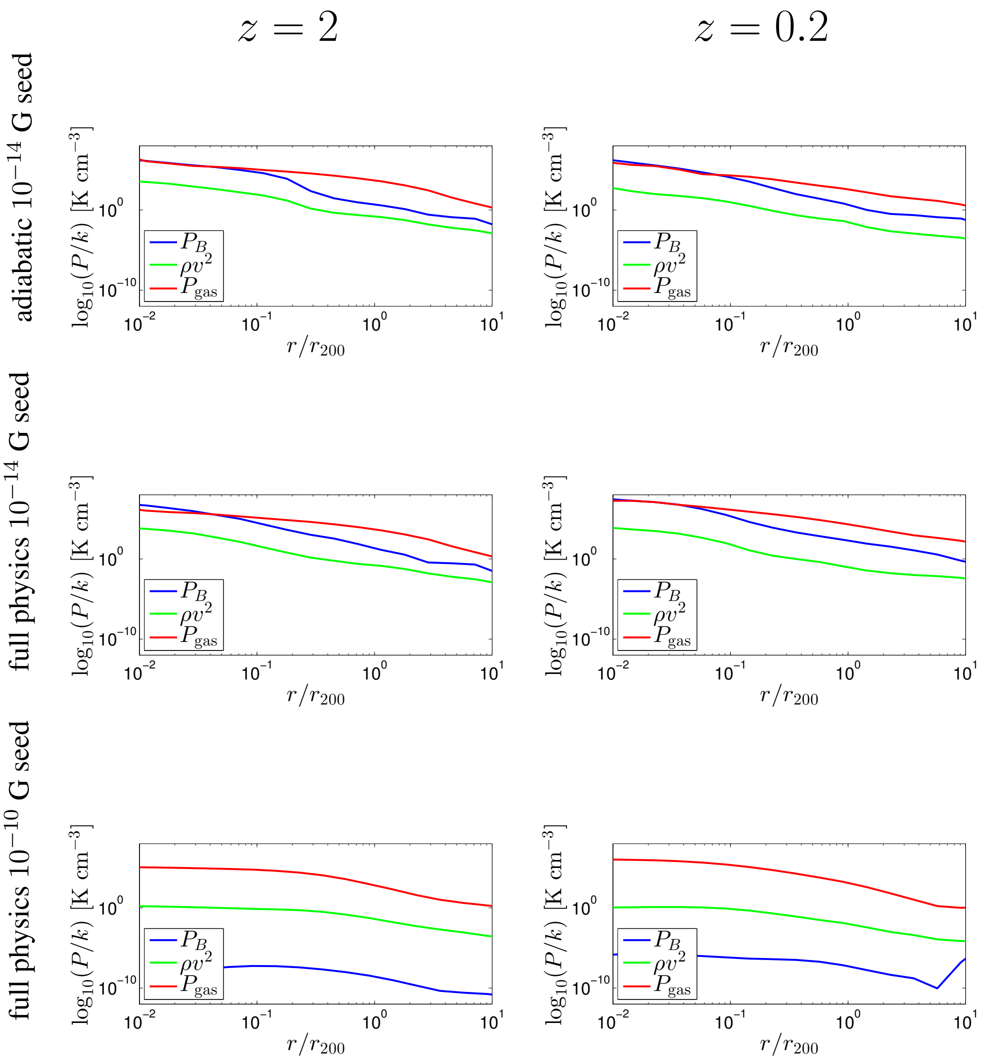

**Figure 6.5:** Radial profile of the thermal gas pressure, magnetic energy density, and kinetic energy density in the most massive halos of each simulation. In adiabatic runs, the profiles are seen to be fully self-similar, and magnetic field amplification at the very center of the halos is weak. With full physics runs, an equipartition is reached at the centers of halos within the virial radius due to additional amplification by small scale shearing motions and turbulence.

magnetic fields are located at density peaks. This is expected, due to the flux-frozen nature of the magnetic field (which is a consequence of the divergence-free condition). Namely, in the case of adiabatic and isotropic contraction, the magnetic field evolves with density $\rho$ as:

$$\mathbf{B} = \mathbf{B}_0/a^2 \propto \rho^{2/3} \tag{6.1}$$

The normalization is given by the initial seed field value. Notably, the net effect of cosmic expansion is to decrease the physical intensity of the $B$-field.

The magnetic field in the full physics simulations are seen to reach much higher values at the centers of halos. The magnetic field amplification goes several orders of magnitude higher than simple adiabatic flux freezing. Radiative cooling and feedback are responsible. Radiative cooling allows gas to reach higher densities than via adiabatic contraction only, and gas outflows from stellar and black hole feedback stir turbulence and add shear to the gas, boosting the $B$-field amplification. This effect becomes especially marked at low redshift. Additionally, the black hole feedback from the center of the galaxies is seen to expand low density bubbles of gas to Mpc scales, in which the magnetic field is strong. This can be a useful way to increase the volume filling factor of strong magnetic fields in the cosmic web (Mocz et al. 2011). It is important to point out that the black hole feedback model does not add a source term to the magnetic field in the simulations. Potentially the magnetic fields may be even stronger in the radio bubbles from the AGN.

The field strengths in low-density regions and in voids are similar in the simulations with and without cooling and feedback. But the $B$-field strength can be somewhat larger in certain low-density areas with the inclusion of baryon physics since stellar and AGN feedback can eject highly magnetized gas from the centers of halos in the intergalactic space.

The distribution of the magnetic field strength in the gas cells as a function of density is shown in Figure 6.3. Isotropic contraction with flux freezing predicts a $B \propto \rho^{2/3}$ scaling, which is seen in the low density gas parcels (these correspond to voids and filaments). Cosmic expansion reduces the normalization of the physical magnetic field strength with time by a factor of $(1+z)^{-2}$. Small scale turbulence and shearing motions in the full physics runs are seen to saturate the magnetic field at high overdensities irrespective of initial field strength. The final saturation strength is an equipartition state with the gas thermal pressure and kinetic energy density (Section 6.4).

Figure 6.4 shows the probability density distributions of the magnetic field strengths in the volume of the box. Low magnetic field values are found in cosmic voids and filaments and the distribution between adiabatic and full physics runs at a fixed initial seed strength is unchanged. The high end of the distribution is stretched due to additional amplification of the magnetic field in the full physics runs. The high end distribution is very similar for both full physics runs with very weak ($10^{-14}$ G) and weak ($10^{-10}$ G) seed fields, demonstrating that the magnetic fields have saturated at high overdensities.

## 6.4 MAGNETIC FIELD IN HALOS

The radial profile of the thermal gas pressure, magnetic energy density, and kinetic energy density in the most massive halos of each simulation is shown in Figure 6.5. In adiabatic runs, the profiles are seen to be fully self-similar, and magnetic field amplification at the very center of the halos is weak, a few orders of magnitude below observed values of $10 - 100\ \mu$G. With full physics runs, an equipartition is reached at the centers of halos within the virial radius due to additional amplification by small scale shearing motions and turbulence, and typical field strengths agree with observations. The outer parts of halos are still unsaturated, and follow a self-similarity, with typical plasma betas of around $\beta \sim 100 - -1000$. This non-equipartition self-similarity can be deduced from a self-similar energetics scaling argument of turbulence (Miniati & Beresnyak 2015). The source of all energy in the turbulent cascade initially comes from gravitational potential energy. This is in part converted to kinetic energy via accretion flows. The flows generate shear and accretion shocks which helps induce fluid instabilities via the baroclinic term that leads to turbulent flows. The shocks do not dissipate tangential flows, which generate a combination of shear, shocks, and turbulence. The turbulence enters a turbulent cascade. Compressive modes dissipate into heat, while turbulent dynamo action (small-scale vorticity) converts a fraction of the turbulent energy to magnetic fields. Assuming an approximately constant efficiency of turbulence generation from the gravitational energy, the ratio of the thermal to turbulent to magnetic energy densities is expected to remain constant. Halos never stop contracting, so the process continues as more gravitational potential

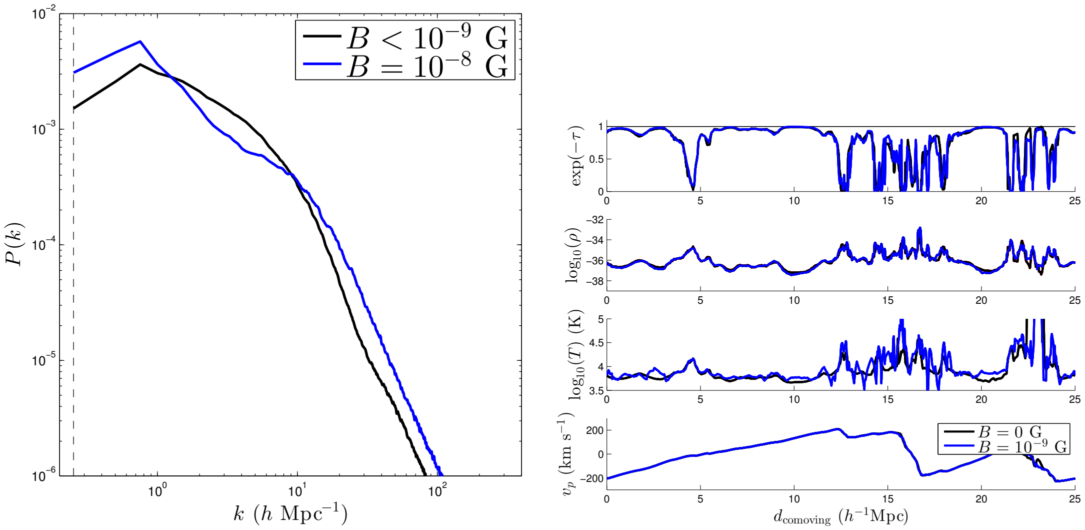

**Figure 6.6:** Lyman-alpha flux power spectra statistics change if the primordial magnetic field is strong enough to have a small dynamical effect on structure formation. Line-of-sight gas properties are affected (e.g. increased fluctuations). But the signature is essentially unchanged if the seed field is dynamically week ($B < 10^{-9}$ G), as expected from current observational upper limits on the primordial field strength.

energy is tapped. This process (with $\beta \sim 100 - -1000$) is observed in the halo profiles of the adiabatic runs, and the outer halos profiles of the full physics runs in Figure 6.5.

## 6.5 Discussion and concluding remarks

Dependence on initial seed strength is largely erased inside halos, as equipartition is reached, and memory of initial field topology is also lost. In some sense this is useful because predictions for observables such as Faraday rotation measures in halos are unaffected by the choice of seed magnetic field, which is not known from observations (Faraday rotation observation predictions are made in Marinacci et al. (2015)). However, this also makes observational strategies to constrain primordial magnetic fields, if they exist, difficult. The best bet is to observe signatures affected by magnetic fields (such as rotation measures) in low density regions, such as outer parts of halos or potentially filaments. This will take future generation telescopes to have the required sensitivity to observe.

We have also taken a look at the effect of the initial field strength on the Lyman-alpha forest, notably the 1D flux power spectrum (Figure fig:LyAlpha), which probes low-density cosmic structure. The Lyman-alpha flux power-spectra was calculated taking random lines of sight in the simulation volume and creating mock spectra by extracting line-of-sight features such as HI density, temperature, and peculiar velocity, following Theuns et al. (1998). As expected, if the magnetic field is dynamically unimportant ($B < 10^{-9}$ G) as known from current observational upper limits, then cosmic structure on large scales is unaffected and so is the flux power spectrum. However, this picture can chance slightly if line widths are additionally turbulently broadened on the smallest scales. Such effects are not captured by our simulation due to the numerical resolution. The additional broadening would be proportional to the field strength. The effect would be a small perturbation in the flux power spectrum towards larger scales. Figure fig:LyAlpha also demonstrates the perturbation on the flux power spectrum once the magnetic field starts becoming dynamically important ($B = 10^{-8}$ G), which is of theoretical interest, but observationally this strong seed field value is ruled out.

Our simulations have chosen the simplest initial magnetic field configuration at $z = 127$, a uniform field. We have also explored more complicated initial field topologies, such as tangled magnetic fields with a characteristic scale of 1 Mpc and $k^-4$ power-law power-spectrum tail in magnetic power, but found the overall picture does not change: in low density regions the magnetic fields amplify by adiabatic contraction according to the flux frozen condition, and in high density regions the magnetic fields saturate. There is no significant inverse-cascade processes due to a tangled field attempting to reduce it's energy configuration by straightening itself out. The primordial field topology is preserved in filaments and voids. Future generation telescopes will be very useful in constraining the magnetic field topology in such regions.

With the inclusion of cooling and feedback, halos with realistic magnetic field strengths $(10 - 100\ \mu\mathrm{G})$ are produced self-consistently by the simulations. The simulations show that the field strengths that are observed correspond to an equipartition fluid state in the interior of the halo.

# 7

# Conclusions and future directions

## 7.1 IMPORTANCE OF CONSTRAINED TRANSPORT

The importance of preserving physical symmetries at the discretized level is seen to have important consequences for the stability and accuracy of simulations. Various examples of this have been presented in Chapters 2, 3, and 4. The moving mesh constrained transport method presented in this dissertation is the first numerical formulation of the MHD equations that is both Galilean invariant and divergence-preserving. This property was seen most readily in the almost-trivial test problem of advecting a magnetic field loop: Fig. 3.7. The field loop is simply expected to translate at constant velocity, as it does with moving mesh CT, but it is seen that using an Eulerian fixed grid breaks Galilean invariance by introducing diffusion errors (in the direction of motion), as does using a Powell 'correction' term. The Powell scheme, while extremely stable numerically, can lead to a false sense of security in the accuracy solution. While it often performs well, the danger is illustrated well in the case of a turbulent box simulation (Fig. 4.3), where the mean-field, another invariant of ideal MHD, actually grows in the moving mesh simulations due to the Powell source terms. The CT approach does keep the mean-field time-steady by construction (Chapter 2).

Chapter 4 demonstrated the numerical side effects of the Powell scheme in astrophysical setting, where magnetic fields in turbulent regions with dynamo processes such as a rotating galactic disk may be over-amplified significantly. It is important to note that these effects may be mitigated with increased resolution. However, it is sometimes impossible to reach the required resolution in large scale simulations with current computational technology.

In summary, constrained transport offers a gold standard solution (machine-precision control) on maintaining important symmetries of the MHD equations, and can be adapted to arbitrary meshes. The use of a moving-mesh offers the advantages of Galilean-invariance and automatic mesh adaptability which is especially useful for resolving regions collapsing under self-gravity.

## 7.2 COMPARISON OF FUNDAMENTAL MAGNETIC AND TURBULENT PROCESSES IN STAR FORMATION AND COSMOLOGY

Chapters 5 and Chapters 6 discussed the formation processes of collapsing halos and protostars. Despite cosmological structure formation being *anti-hierarchical* (the smallest gravitationally bound structures such as matter peaks that contain the first stars and stellar clusters form first, and are subsequently merged to form galaxies, followed by galaxy groups, clusters and superclusters) and star formation being *hierarchical* (large congregations of gas consist of small structures which themselves also fragment and collapse in to stellar objects), the the physical processes have related physics. They both fall into the category of structure formation in magneto-gravo-turbulence. There is a general transfer of energies from gravitational potential energy to kinetic and magnetic energies. Much of the star formation process is in the (optically-thin) isothermal limit, unlike in the cosmological context, which means that the gas cannot be heated in the collapse (heating is a sort of sink term for collapse in the cosmological context which adds additional pressure support against collapse).

Flux freezing is an important condition for describing the overall picture of how the magnetic field grows in cosmological and star forming systems. Flux freezing gives a scaling of magnetic field with density that is just determined by the geometry of collapse. The collapse is isotropic overall in the case of cosmology, yielding $B \propto \rho^{2/3}$, and can vary between isotropic and anisotropic in the case of star formation, yielding $B \propto \rho^{1/2}$ in the case that the mean-magnetic field is strong. But turbulence further plays a role in amplifying the field. In the case of cosmology, turbulence is generated by accretion shocks, which allows small-scale dynamo action and shearing motions to further amplify the magnetic field beyond simple flux-freezing scaling arguments. Galactic feedback processes and cooling provide enough stirring and shear to the gas that the magnetic field can saturate at equipartition levels at halo centers and inside galaxies. Star formation in galaxies has starting conditions from a saturated turbulent environment, where turbulent stirring is present on scales larger than the collapsing molecular cloud region. The stirring may come from both cosmological turbulence cascading down to the smallest scales and also from stirring due to supernova explosions. Collapse under self-gravity under these conditions (free-fall timescale is less than sound-crossing timescale) will cause the magnetic field to scale according to flux freezing. However, flux freezing actually breaks a little in this turbulent regime, due to the fast turbulent reconnection diffusion mechanism. An arbitrarily small amount of resistivity can cause magnetic reconnection, breaking the flux-frozen condition. The interstellar medium will physically have a small resistivity, and numerical resistivity is also unavoidably present in the code, and it turns out the effect of turbulent reconnection in this regime is independent of the strength of resistivity, so the physical process is accurately captured by the code. Reconnection allows the mass-to-flux ratio in cores to change as the core collapses (an invariant in pure ideal MHD). Our simulations show that reconnection can even allow for regions which are initially slightly magnetically sub-critical to collapse.

The pictures of collapse under self-gravity in magneto-gravo-turbulence that we have painted show that while there are common physical themes, there is also diversity in behavior in different physical regimes.

## 7.3 FUTURE DIRECTIONS

Future work will propel in the direction of performing larger simulations with more detail physics and resolution. In the case of star formation, it will be useful to repeat the simulations without the isothermal assumption to continue following collapse into the adiabatic phase and see whether our simulations form disks (e.g., see whether turbulence can solve the magnetic breaking catastrophe). Such simulations will likely require the use of sink particles and radiative feedback to accurately capture the process.

The star formation simulations may be used to help interpret future ALMA observations of young protostellar systems. We have made theoretical predictions for how the magnetic field orientation correlations with the Alfvénic mach number of the system as a function of length scale.

In the case of cosmological simulations, it will be interesting to study the effects of magnetic fields inside galaxies in higher resolution simulations (such as the new ILLUSTRIS++ simulations which have improved the galactic feedback modules and include magnetic fields), to study how it effects star formation rate and changes the disk scale height and outflow properties. Adding in magnetic field generation from accretion shocks and reionization fronts would be also very useful as a way to directly distinguish between these mechanisms.

Aside from these two applications, the MHD module in AREPO can be applied to study any astrophysical magnetic process with large dynamical range in densities more accurately than before. Some interesting applications include tidal disruption events, circumbinary disks, and radio mode feedback from active galactic nuclei.

## REFERENCES

ALMA Partnership, Brogan, C. L., Pérez, L. M., Hunter, T. R., Dent, W. R. F., Hales, A. S., Hills, R. E., Corder, S., Fomalont, E. B., Vlahakis, C., Asaki, Y., Barkats, D., Hirota, A., Hodge, J. A., Impellizzeri, C. M. V., Kneissl, R., Liuzzo, E., Lucas, R., Marcelino, N., Matsushita, S., Nakanishi, K., Phillips, N., Richards, A. M. S., Toledo, I., Aladro, R., Broguiere, D., Cortes, J. R., Cortes, P. C., Espada, D., Galarza, F., Garcia-Appadoo, D., Guzman-Ramirez, L., Humphreys, E. M., Jung, T., Kameno, S., Laing, R. A., Leon, S., Marconi, G., Mignano, A., Nikolic, B., Nyman, L.-A., Radiszcz, M., Remijan, A., Rodón, J. A., Sawada, T., Takahashi, S., Tilanus, R. P. J., Vila Vilaro, B., Watson, L. C., Wiklind, T., Akiyama, E., Chapillon, E., de Gregorio-Monsalvo, I., Di Francesco, J., Gueth, F., Kawamura, A., Lee, C.-F., Nguyen Luong, Q., Mangum, J., Pietu, V., Sanhueza, P., Saigo, K., Takakuwa, S., Ubach, C., van Kempen, T., Wootten, A., Castro-Carrizo, A., Francke, H., Gallardo, J., Garcia, J., Gonzalez, S., Hill, T., Kaminski, T., Kurono, Y., Liu, H.-Y., Lopez, C., Morales, F., Plarre, K., Schieven, G., Testi, L., Videla, L., Villard, E., Andreani, P., Hibbard, J. E., & Tatematsu, K. (2015). The 2014 ALMA Long Baseline Campaign: First Results from High Angular Resolution Observations toward the HL Tau Region. *ApJ*, 808, L3.

Balbus, S. A. (2003). Enhanced Angular Momentum Transport in Accretion Disks. *ARA&A*, 41, 555–597.

Balbus, S. A. & Hawley, J. F. (1998). Instability, turbulence, and enhanced transport in accretion disks. *Reviews of Modern Physics*, 70, 1–53.

Balsara, D. S. (2001). Divergence-Free Adaptive Mesh Refinement for Magnetohydrodynamics. *Journal of Computational Physics*, 174, 614–648.

Balsara, D. S. (2004). Second-Order-accurate Schemes for Magnetohydrodynamics with Divergence-free Reconstruction. *ApJS*, 151, 149–184.

Balsara, D. S. (2009). Divergence-free reconstruction of magnetic fields and WENO schemes for magnetohydrodynamics. *Journal of Computational Physics*, 228, 5040–5056.

Balsara, D. S. (2012). A two-dimensional HLLC Riemann solver for conservation laws: Application to Euler and magnetohydrodynamic flows. *Journal of Computational Physics*, 231, 7476–7503.

Balsara, D. S. (2014). Multidimensional Riemann problem with self-similar internal structure. Part I - Application to hyperbolic conservation laws on structured meshes. *Journal of*

*Computational Physics*, 277, 163–200.

Balsara, D. S. (2015). Three dimensional HLL Riemann solver for conservation laws on structured meshes; Application to Euler and magnetohydrodynamic flows. *Journal of Computational Physics*, 295, 1–23.

Balsara, D. S., Amano, T., Garain, S., & Kim, J. (2016). A high-order relativistic two-fluid electrodynamic scheme with consistent reconstruction of electromagnetic fields and a multidimensional Riemann solver for electromagnetism. *Journal of Computational Physics*, 318, 169–200.

Balsara, D. S. & Dumbser, M. (2015a). Divergence-free MHD on unstructured meshes using high order finite volume schemes based on multidimensional Riemann solvers. *Journal of Computational Physics*, 299, 687–715.

Balsara, D. S. & Dumbser, M. (2015b). Multidimensional Riemann problem with self-similar internal structure. Part II - Application to hyperbolic conservation laws on unstructured meshes. *Journal of Computational Physics*, 287, 269–292.

Balsara, D. S., Dumbser, M., & Abgrall, R. (2014). Multidimensional HLLC Riemann solver for unstructured meshes - With application to Euler and MHD flows. *Journal of Computational Physics*, 261, 172–208.

Balsara, D. S. & Kim, J. (2004). A Comparison between Divergence-Cleaning and Staggered-Mesh Formulations for Numerical Magnetohydrodynamics. *ApJ*, 602, 1079–1090.

Balsara, D. S. & Spicer, D. S. (1999). A Staggered Mesh Algorithm Using High Order Godunov Fluxes to Ensure Solenoidal Magnetic Fields in Magnetohydrodynamic Simulations. *Journal of Computational Physics*, 149, 270–292.

Bauer, A. & Springel, V. (2012). Subsonic turbulence in smoothed particle hydrodynamics and moving-mesh simulations. *MNRAS*, 423, 2558–2578.

Becerra, F., Greif, T. H., Springel, V., & Hernquist, L. E. (2015). Formation of massive protostars in atomic cooling haloes. *MNRAS*, 446, 2380–2393.

Beck, A. M., Lesch, H., Dolag, K., Kotarba, H., Geng, A., & Stasyszyn, F. A. (2012). Origin of strong magnetic fields in Milky Way-like galactic haloes. *MNRAS*, 422, 2152–2163.

Beck, R. (2007). Measurements of Cosmic Magnetism with LOFAR and SKA. *Advances in*

*Radio Science*, 5, 399–405.

Beck, R., Brandenburg, A., Moss, D., Shukurov, A., & Sokoloff, D. (1996). Galactic Magnetism: Recent Developments and Perspectives. *ARA&A*, 34, 155–206.

Biermann, L. (1950). Über den Ursprung der Magnetfelder auf Sternen und im interstellaren Raum (miteinem Anhang von A. Schlüter). *Zeitschrift Naturforschung Teil A*, 5, 65.

Blandford, R. D. & Payne, D. G. (1982). Hydromagnetic flows from accretion discs and the production of radio jets. *MNRAS*, 199, 883–903.

Blandford, R. D. & Znajek, R. L. (1977). Electromagnetic extraction of energy from Kerr black holes. *MNRAS*, 179, 433–456.

Brackbill, J. (1985). Fluid modeling of magnetized plasmas. *Space Science Reviews*, 42, 153–167.

Brackbill, J. U. & Barnes, D. C. (1980). The effect of nonzero product of magnetic gradient and B on the numerical solution of the magnetohydrodynamic equations. *Journal of Computational Physics*, 35, 426–430.

Burkhart, B., Falceta-Gonçalves, D., Kowal, G., & Lazarian, A. (2009). Density Studies of MHD Interstellar Turbulence: Statistical Moments, Correlations and Bispectrum. *ApJ*, 693, 250–266.

Burkhart, B., Lee, M.-Y., Murray, C. E., & Stanimirović, S. (2015). The Lognormal Probability Distribution Function of the Perseus Molecular Cloud: A Comparison of HI and Dust. *ApJ*, 811, L28.

Burkhart, B., Stalpes, K., & Collins, D. (2016). The Razor's Edge of Collapse: The Transition Point from Lognormal to Powerlaw in Molecular Cloud PDFs. *ArXiv e-prints*.

Cho, J., Vishniac, E. T., Beresnyak, A., Lazarian, A., & Ryu, D. (2009). Growth of Magnetic Fields Induced by Turbulent Motions. *ApJ*, 693, 1449–1461.

Christlieb, A. J., Rossmanith, J. A., & Tang, Q. (2014). Finite difference weighted essentially non-oscillatory schemes with constrained transport for ideal magnetohydrodynamics. *Journal of Computational Physics*, 268, 302–325.

Ciolek, G. E. & Mouschovias, T. C. (1994). Ambipolar diffusion, interstellar dust, and the formation of cloud cores and protostars. 3: Typical axisymmetric solutions. *ApJ*, 425, 142–160.

Collins, D. C., Kritsuk, A. G., Padoan, P., Li, H., Xu, H., Ustyugov, S. D., & Norman, M. L. (2012). The Two States of Star-forming Clouds. *ApJ*, 750, 13.

Collins, D. C., Padoan, P., Norman, M. L., & Xu, H. (2011). Mass and Magnetic Distributions in Self-gravitating Super-Alfvénic Turbulence with Adaptive Mesh Refinement. *ApJ*, 731, 59.

Crutcher, R. M. (2012). Magnetic Fields in Molecular Clouds. *ARA&A*, 50, 29–63.

Crutcher, R. M., Wandelt, B., Heiles, C., Falgarone, E., & Troland, T. H. (2010). Magnetic Fields in Interstellar Clouds from Zeeman Observations: Inference of Total Field Strengths by Bayesian Analysis. *ApJ*, 725, 466–479.

Cunningham, A. J., Frank, A., Varnière, P., Mitran, S., & Jones, T. W. (2009). Simulating Magnetohydrodynamical Flow with Constrained Transport and Adaptive Mesh Refinement: Algorithms and Tests of the AstroBEAR Code. *ApJS*, 182, 519–542.

Dai, W. & Woodward, P. R. (1998a). A Simple Finite Difference Scheme for Multidimensional Magnetohydrodynamical Equations. *Journal of Computational Physics*, 142, 331–369.

Dai, W. & Woodward, P. R. (1998b). On the Divergence-free Condition and Conservation Laws in Numerical Simulations for Supersonic Magnetohydrodynamical Flows. *ApJ*, 494, 317–335.

Dedner, A., Kemm, F., Kröner, D., Munz, C.-D., Schnitzer, T., & Wesenberg, M. (2002). Hyperbolic Divergence Cleaning for the MHD Equations. *Journal of Computational Physics*, 175, 645–673.

Del Zanna, L., Bucciantini, N., & Londrillo, P. (2003). An efficient shock-capturing central-type scheme for multidimensional relativistic flows. II. Magnetohydrodynamics. *A&A*, 400, 397–413.

Donati, J.-F. & Landstreet, J. D. (2009). Magnetic Fields of Nondegenerate Stars. *ARA&A*, 47, 333–370.

Douma, M. (2017). Pointillism: Seurat's grande jatte and circus. `http://www.webexhibits.org/colorart/jatte.html/`, (accessed 2017-03-29).

Dubois, Y. & Teyssier, R. (2010). Magnetised winds in dwarf galaxies. *A&A*, 523, A72.

Duffell, P. C. & MacFadyen, A. I. (2011). TESS: A Relativistic Hydrodynamics Code on a Moving Voronoi Mesh. *ApJS*, 197, 15.

Duffell, P. C. & MacFadyen, A. I. (2015). High-frequency Voronoi noise reduced by smoothed-mesh motion. *MNRAS*, 449, 2718–2722.

Etienne, Z. B., Paschalidis, V., Haas, R., Mösta, P., & Shapiro, S. L. (2015). IllinoisGRMHD: an open-source, user-friendly GRMHD code for dynamical spacetimes. *Classical and Quantum Gravity*, 32(17), 175009.

Evans, C. R. & Hawley, J. F. (1988). Simulation of magnetohydrodynamic flows - A constrained transport method. *ApJ*, 332, 659–677.

Fabian, A. C., Celotti, A., Blundell, K. M., Kassim, N. E., & Perley, R. A. (2002). The properties of the X-ray holes in the intracluster medium of the Perseus cluster. *MNRAS*, 331, 369–375.

Federrath, C. (2015). Inefficient star formation through turbulence, magnetic fields and feedback. *MNRAS*, 450, 4035–4042.

Federrath, C., Chabrier, G., Schober, J., Banerjee, R., Klessen, R. S., & Schleicher, D. R. G. (2011a). Mach Number Dependence of Turbulent Magnetic Field Amplification: Solenoidal versus Compressive Flows. *Physical Review Letters*, 107(11), 114504.

Federrath, C. & Klessen, R. S. (2012). The Star Formation Rate of Turbulent Magnetized Clouds: Comparing Theory, Simulations, and Observations. *ApJ*, 761, 156.

Federrath, C., Klessen, R. S., & Schmidt, W. (2008). The Density Probability Distribution in Compressible Isothermal Turbulence: Solenoidal versus Compressive Forcing. *ApJ*, 688, L79.

Federrath, C., Roman-Duval, J., Klessen, R. S., Schmidt, W., & Mac Low, M.-M. (2010). Comparing the statistics of interstellar turbulence in simulations and observations. Solenoidal versus compressive turbulence forcing. *A&A*, 512, A81.

Federrath, C., Sur, S., Schleicher, D. R. G., Banerjee, R., & Klessen, R. S. (2011b). A New Jeans Resolution Criterion for (M)HD Simulations of Self-gravitating Gas: Application to Magnetic Field Amplification by Gravity-driven Turbulence. *ApJ*, 731, 62.

Fermi, E. (1949). On the Origin of the Cosmic Radiation. *Physical Review*, 75, 1169–1174.

Florinski, V., Guo, X., Balsara, D. S., & Meyer, C. (2013). Magnetohydrodynamic Modeling of Solar System Processes on Geodesic Grids. *ApJS*, 205, 19.

Fromang, S., Hennebelle, P., & Teyssier, R. (2006). A high order Godunov scheme with constrained transport and adaptive mesh refinement for astrophysical magnetohydrodynamics. *A&A*, 457, 371–384.

Gaburov, E., Johansen, A., & Levin, Y. (2012). Magnetically Levitating Accretion Disks around Supermassive Black Holes. *ApJ*, 758, 103.

Gaburov, E. & Nitadori, K. (2011). Astrophysical weighted particle magnetohydrodynamics. *MNRAS*, 414, 129–154.

Gardiner, T. A. & Stone, J. M. (2005). An unsplit Godunov method for ideal MHD via constrained transport. *Journal of Computational Physics*, 205, 509–539.

Gardiner, T. A. & Stone, J. M. (2008). An unsplit Godunov method for ideal MHD via constrained transport in three dimensions. *Journal of Computational Physics*, 227, 4123–4141.

Girart, J. M., Beltrán, M. T., Zhang, Q., Rao, R., & Estalella, R. (2009). Magnetic Fields in the Formation of Massive Stars. *Science*, 324, 1408.

Girart, J. M., Rao, R., & Marrone, D. P. (2006). Magnetic Fields in the Formation of Sun-Like Stars. *Science*, 313, 812–814.

Gnedin, N. Y., Ferrara, A., & Zweibel, E. G. (2000). Generation of the Primordial Magnetic Fields during Cosmological Reionization. *ApJ*, 539, 505–516.

Goldreich, P. & Sridhar, S. (1995). Toward a theory of interstellar turbulence. 2: Strong alfvenic turbulence. *ApJ*, 438, 763–775.

Gopal-Krishna & Wiita, P. J. (2001). Was the Cosmic Web of Protogalactic Material Permeated by Lobes of Radio Galaxies During the Quasar Era? *ApJ*, 560, L115–L118.

Goudis, A. (2017). The starry night by vincent van gogh (1889). `http://www.annagoudis.me/the-starry-night/`, (accessed 2017-03-29).

Gourlay, M. J. (2017). Fluid simulation for video games (part

6). https://software.intel.com/en-us/articles/fluid-simulation-for-video-games-part-6/, (accessed 2017-03-29).

Grasso, D. & Rubinstein, H. R. (2001). Magnetic fields in the early Universe. *Physics Reports*, 348, 163–266.

Groe, P. (2017). Piet mondrian. https://www.tes.com/lessons/lUMZUSLI22ua7g/piet-mondrian/, (accessed 2017-03-29).

Hawley, J. F., Gammie, C. F., & Balbus, S. A. (1996). Local Three-dimensional Simulations of an Accretion Disk Hydromagnetic Dynamo. *ApJ*, 464, 690.

Helzel, C., Rossmanith, J. A., & Taetz, B. (2011). An unstaggered constrained transport method for the 3D ideal magnetohydrodynamic equations. *Journal of Computational Physics*, 230, 3803–3829.

Helzel, C., Rossmanith, J. A., & Taetz, B. (2012). A high-order unstaggered constrained transport method for the 3D ideal magnetohydrodynamic equations based on the method of lines. *ArXiv e-prints*.

Hopkins, P. F. (2015). A new class of accurate, mesh-free hydrodynamic simulation methods. *MNRAS*, 450, 53–110.

Hopkins, P. F. & Raives, M. J. (2016). Accurate, meshless methods for magnetohydrodynamics. *MNRAS*, 455, 51–88.

Houde, M., Hull, C. L. H., Plambeck, R. L., Vaillancourt, J. E., & Hildebrand, R. H. (2016). Dispersion of Magnetic Fields in Molecular Clouds. IV. Analysis of Interferometry Data. *ApJ*, 820, 38.

Hull, C. L. H., Mocz, P., Burkhart, B. K., Miquel Girart, J., Goodman, A. A., Cortes, P., Li, Z.-Y., Lai, S.-P., Hernquist, L., & Springel, V. (2017). Probing turbulent, magnetized star formation with ALMA observations and next-generation AREPO simulations. In *American Astronomical Society Meeting Abstracts*, volume 229 of *American Astronomical Society Meeting Abstracts* (pp. 153.01).

Hull, C. L. H., Plambeck, R. L., Kwon, W., Bower, G. C., Carpenter, J. M., Crutcher, R. M., Fiege, J. D., Franzmann, E., Hakobian, N. S., Heiles, C., Houde, M., Hughes, A. M., Lamb, J. W., Looney, L. W., Marrone, D. P., Matthews, B. C., Pillai, T., Pound, M. W., Rahman, N., Sandell, G., Stephens, I. W., Tobin, J. J., Vaillancourt, J. E., Volgenau, N. H.,

& Wright, M. C. H. (2014). TADPOL: A 1.3 mm Survey of Dust Polarization in Star-forming Cores and Regions. *ApJS*, 213, 13.

Joos, M., Hennebelle, P., Ciardi, A., & Fromang, S. (2013). The influence of turbulence during magnetized core collapse and its consequences on low-mass star formation. *A&A*, 554, A17.

Kauffmann, J. (2016). Star Formation in the Galactic Center. *ArXiv e-prints*.

Kelley, L. Z., Tchekhovskoy, A., & Narayan, R. (2014). Tidal disruption and magnetic flux capture: powering a jet from a quiescent black hole. *MNRAS*, 445, 3919–3938.

Kowal, G., Lazarian, A., Vishniac, E. T., & Otmianowska-Mazur, K. (2009). Numerical Tests of Fast Reconnection in Weakly Stochastic Magnetic Fields. *ApJ*, 700, 63–85.

Kraichnan, R. H. (1965). Inertial-Range Spectrum of Hydromagnetic Turbulence. *Physics of Fluids*, 8, 1385–1387.

Kritsuk, A. G., Norman, M. L., Padoan, P., & Wagner, R. (2007). The Statistics of Supersonic Isothermal Turbulence. *ApJ*, 665, 416–431.

Krumholz, M. R. & McKee, C. F. (2005). A General Theory of Turbulence-regulated Star Formation, from Spirals to Ultraluminous Infrared Galaxies. *ApJ*, 630, 250–268.

Larson, R. B. (1969). Numerical calculations of the dynamics of collapsing proto-star. *MNRAS*, 145, 271.

Larson, R. B. (1981). Turbulence and star formation in molecular clouds. *MNRAS*, 194, 809–826.

Lazarian, A., Esquivel, A., & Crutcher, R. (2012). Magnetization of Cloud Cores and Envelopes and Other Observational Consequences of Reconnection Diffusion. *ApJ*, 757, 154.

Lazarian, A. & Vishniac, E. T. (1999). Reconnection in a Weakly Stochastic Field. *ApJ*, 517, 700–718.

Lazarian, A., Vishniac, E. T., & Cho, J. (2004). Magnetic Field Structure and Stochastic Reconnection in a Partially Ionized Gas. *ApJ*, 603, 180–197.

Lewis, A. & Bridle, S. (2002). Cosmological parameters from CMB and other data: A Monte Carlo approach. *Phys. Rev. D*, 66(10), 103511.

Li, H.-b., Dowell, C. D., Goodman, A., Hildebrand, R., & Novak, G. (2009). Anchoring Magnetic Field in Turbulent Molecular Clouds. *ApJ*, 704, 891–897.

Li, H.-B., Yuen, K. H., Otto, F., Leung, P. K., Sridharan, T. K., Zhang, Q., Liu, H., Tang, Y.-W., & Qiu, K. (2015a). Self-similar fragmentation regulated by magnetic fields in a region forming massive stars. *Nat*, 520, 518–521.

Li, P. S., McKee, C. F., & Klein, R. I. (2015b). Magnetized interstellar molecular clouds - I. Comparison between simulations and Zeeman observations. *MNRAS*, 452, 2500–2527.

Marinacci, F. & Vogelsberger, M. (2016). Effects of simulated cosmological magnetic fields on the galaxy population. *MNRAS*, 456, L69–L73.

Marinacci, F., Vogelsberger, M., Mocz, P., & Pakmor, R. (2015). The large-scale properties of simulated cosmological magnetic fields. *MNRAS*, 453, 3999–4019.

McCourt, M., Sharma, P., Quataert, E., & Parrish, I. J. (2012). Thermal instability in gravitationally stratified plasmas: implications for multiphase structure in clusters and galaxy haloes. *MNRAS*, 419, 3319–3337.

McKee, C. F., Li, P. S., & Klein, R. I. (2010). Sub-Alfvénic Non-ideal MHD Turbulence Simulations with Ambipolar Diffusion. II. Comparison with Observation, Clump Properties, and Scaling to Physical Units. *ApJ*, 720, 1612–1634.

McKee, C. F. & Ostriker, E. C. (2007). Theory of Star Formation. *ARA&A*, 45, 565–687.

McKee, C. F. & Tan, J. C. (2003). The Formation of Massive Stars from Turbulent Cores. *ApJ*, 585, 850–871.

McKee, C. F., Zweibel, E. G., Goodman, A. A., & Heiles, C. (1993). Magnetic Fields in Star-Forming Regions - Theory. In E. H. Levy & J. I. Lunine (Eds.), *Protostars and Planets III* (pp. 327).

McKinney, J. C., Tchekhovskoy, A., Sadowski, A., & Narayan, R. (2014). Three-dimensional general relativistic radiation magnetohydrodynamical simulation of super-Eddington accretion, using a new code HARMRAD with M1 closure. *MNRAS*, 441, 3177–3208.

McLaughlin, D. E. & Pudritz, R. E. (1997). Gravitational Collapse and Star Formation in Logotropic and Nonisothermal Spheres. *ApJ*, 476, 750–765.

Mestel, L. (1965). Problems of Star Formation I, II. *Quarterly Journal of the Royal Astronomical Society*, 6, 161.

Mestel, L. (1966). The magnetic field of a contracting gas cloud. I,Strict flux-freezing. *MNRAS*, 133, 265.

Mignone, A., Bodo, G., Massaglia, S., Matsakos, T., Tesileanu, O., Zanni, C., & Ferrari, A. (2007). PLUTO: A Numerical Code for Computational Astrophysics. *ApJS*, 170, 228–242.

Mignone, A., Zanni, C., Tzeferacos, P., van Straalen, B., Colella, P., & Bodo, G. (2012). The PLUTO Code for Adaptive Mesh Computations in Astrophysical Fluid Dynamics. *ApJS*, 198, 7.

Miniati, F. & Beresnyak, A. (2015). Self-similar energetics in large clusters of galaxies. *Nat*, 523, 59–62.

Miniati, F. & Martin, D. F. (2011). Constrained-transport Magnetohydrodynamics with Adaptive Mesh Refinement in CHARM. *ApJS*, 195, 5.

Miyoshi, T. & Kusano, K. (2005). A multi-state HLL approximate Riemann solver for ideal magnetohydrodynamics. *Journal of Computational Physics*, 208, 315–344.

Mocz, P. (2017a). Correspondence between constrained transport and vector potential methods for magnetohydrodynamics. *Journal of Computational Physics*, 328, 221–233.

Mocz, P. (2017b). Shocks and the riemann problem in full 3d simulations. `https://www.cfa.harvard.edu/~pmocz/shocks/numerical.html/`, (accessed 2017-03-29).

Mocz, P., Fabian, A. C., & Blundell, K. M. (2011). Inverse-Compton ghosts and double-lobed radio sources in the X-ray sky. *MNRAS*, 413, 1107–1120.

Mocz, P., Pakmor, R., Springel, V., Vogelsberger, M., Marinacci, F., & Hernquist, L. (2016). A moving mesh unstaggered constrained transport scheme for magnetohydrodynamics. *MNRAS*, 463, 477–488.

Mocz, P., Vogelsberger, M., & Hernquist, L. (2014a). A constrained transport scheme for MHD on unstructured static and moving meshes. *MNRAS*, 442, 43–55.

Mocz, P., Vogelsberger, M., Sijacki, D., Pakmor, R., & Hernquist, L. (2014b). A discontinuous

Galerkin method for solving the fluid and magnetohydrodynamic equations in astrophysical simulations. *MNRAS*, 437, 397–414.

Mouschovias, T. C. (1976a). Nonhomologous contraction and equilibria of self-gravitating, magnetic interstellar clouds embedded in an intercloud medium: Star formation. I Formulation of the problem and method of solution. *ApJ*, 206, 753–767.

Mouschovias, T. C. (1976b). Nonhomologous contraction and equilibria of self-gravitating, magnetic interstellar clouds embedded in an intercloud medium: Star formation. II - Results. *ApJ*, 207, 141–158.

Murray, D. W., Chang, P., Murray, N. W., & Pittman, J. (2015). Collapse in Self-gravitating Turbulent Fluids. *ArXiv e-prints*.

Murray, N. & Chang, P. (2015). Star Formation in Self-gravitating Turbulent Fluids. *ApJ*, 804, 44.

Myers, A. T., McKee, C. F., Cunningham, A. J., Klein, R. I., & Krumholz, M. R. (2013). The Fragmentation of Magnetized, Massive Star-forming Cores with Radiative Feedback. *ApJ*, 766, 97.

National Museum of Mathematics (2017). Graph theory. `http://momath.org/home/educator-session-option-graph-theory/`, (accessed 2017-03-29).

Nelson, D., Pillepich, A., Genel, S., Vogelsberger, M., Springel, V., Torrey, P., Rodriguez-Gomez, V., Sijacki, D., Snyder, G. F., Griffen, B., Marinacci, F., Blecha, L., Sales, L., Xu, D., & Hernquist, L. (2015). The illustris simulation: Public data release. *Astronomy and Computing*, 13, 12–37.

Neronov, A. & Vovk, I. (2010). Evidence for Strong Extragalactic Magnetic Fields from Fermi Observations of TeV Blazars. *Science*, 328, 73.

Orszag, S. A. & Tang, C.-M. (1979). Small-scale structure of two-dimensional magnetohydrodynamic turbulence. *Journal of Fluid Mechanics*, 90, 129–143.

Pakmor, R., Bauer, A., & Springel, V. (2011). Magnetohydrodynamics on an unstructured moving grid. *MNRAS*, 418, 1392–1401.

Pakmor, R., Marinacci, F., & Springel, V. (2014). Magnetic Fields in Cosmological Simulations of Disk Galaxies. *ApJ*, 783, L20.

Pakmor, R., Pfrommer, C., Simpson, C. M., & Springel, V. (2016a). Galactic winds driven by isotropic and anisotropic cosmic ray diffusion in disk galaxies. *ArXiv e-prints 1605.00643*.

Pakmor, R. & Springel, V. (2013). Simulations of magnetic fields in isolated disc galaxies. *MNRAS*, 432, 176–193.

Pakmor, R., Springel, V., Bauer, A., Mocz, P., Munoz, D. J., Ohlmann, S. T., Schaal, K., & Zhu, C. (2016b). Improving the convergence properties of the moving-mesh code AREPO. *MNRAS*, 455, 1134–1143.

Parker, E. N. (1966). The Dynamical State of the Interstellar Gas and Field. *ApJ*, 145, 811.

Parker, E. N. (1967). The Dynamical State of the Interstellar Gas and Field. III. Turbulence and Enhanced Diffusion. *ApJ*, 149, 535.

Penston, M. V. (1969). Dynamics of self-gravitating gaseous spheres-II. Collapses of gas spheres with cooling and the behaviour of polytropic gas spheres. *MNRAS*, 145, 457.

Pfrommer, C., Pakmor, R., Schaal, K., Simpson, C. M., & Springel, V. (2016). Simulating cosmic ray physics on a moving mesh. *ArXiv e-prints 1604.07399*.

Picone, J. M. & Dahlburg, R. B. (1991). Evolution of the Orszag-Tang vortex system in a compressible medium. II - Supersonic flow. *Physics of Fluids B*, 3, 29–44.

Pillai, T., Kauffmann, J., Wiesemeyer, H., & Menten, K. M. (2016). CN Zeeman and dust polarization in a high-mass cold clump. *A&A*, 591, A19.

Powell, K. G., Roe, P. L., Linde, T. J., Gombosi, T. I., & de Zeeuw, D. L. (1999). A Solution-Adaptive Upwind Scheme for Ideal Magnetohydrodynamics. *Journal of Computational Physics*, 154, 284–309.

Price, D. J. & Federrath, C. (2010). A comparison between grid and particle methods on the statistics of driven, supersonic, isothermal turbulence. *MNRAS*, 406, 1659–1674.

Qiu, K., Zhang, Q., Menten, K. M., Liu, H. B., Tang, Y.-W., & Girart, J. M. (2014). Submillimeter Array Observations of Magnetic Fields in G240.31+0.07: An Hourglass in a Massive Cluster-forming Core. *ApJ*, 794, L18.

Rao, R., Girart, J. M., Marrone, D. P., Lai, S.-P., & Schnee, S. (2009). IRAS 16293: A ”Magnetic” Tale of Two Cores. *ApJ*, 707, 921–935.

Rieder, M. & Teyssier, R. (2016). A small-scale dynamo in feedback-dominated galaxies as the origin of cosmic magnetic fields - I. The kinematic phase. *MNRAS*, 457, 1722–1738.

Ryu, D., Kang, H., & Biermann, P. L. (1998a). Cosmic magnetic fields in large scale filaments and sheets. *A&A*, 335, 19–25.

Ryu, D., Miniati, F., Jones, T. W., & Frank, A. (1998b). A Divergence-free Upwind Code for Multidimensional Magnetohydrodynamic Flows. *ApJ*, 509, 244–255.

Sanders, J. S., Fabian, A. C., Churazov, E., Schekochihin, A. A., Simionescu, A., Walker, S. A., & Werner, N. (2013). Linear Structures in the Core of the Coma Cluster of Galaxies. *Science*, 341, 1365–1368.

Sądowski, A., Narayan, R., McKinney, J. C., & Tchekhovskoy, A. (2014). Numerical simulations of super-critical black hole accretion flows in general relativity. *MNRAS*, 439, 503–520.

Seifried, D., Banerjee, R., Pudritz, R. E., & Klessen, R. S. (2012). Disc formation in turbulent massive cores: circumventing the magnetic braking catastrophe. *MNRAS*, 423, L40–L44.

Shu, F. H. (1977). Self-similar collapse of isothermal spheres and star formation. *ApJ*, 214, 488–497.

Shu, F. H., Adams, F. C., & Lizano, S. (1987). Star formation in molecular clouds - Observation and theory. *ARA&A*, 25, 23–81.

Solomon, J. & Butscher, A. (2017). Discrete laplacians. `https://graphics.stanford.edu/courses/cs468-13-spring/assets/lecture12.pdf/`, (accessed 2017-03-29).

Spergel, D. N., Flauger, R., & Hložek, R. (2015). Planck data reconsidered. *Phys. Rev. D*, 91(2), 023518.

Springel, V. (2005). The cosmological simulation code GADGET-2. *MNRAS*, 364, 1105–1134.

Springel, V. (2010). E pur si muove: Galilean-invariant cosmological hydrodynamical simulations on a moving mesh. *MNRAS*, 401, 791–851.

Stephens, I. W., Looney, L. W., Kwon, W., Hull, C. L. H., Plambeck, R. L., Crutcher, R. M., Chapman, N., Novak, G., Davidson, J., Vaillancourt, J. E., Shinnaga, H., & Matthews, T.

(2013). The Magnetic Field Morphology of the Class 0 Protostar L1157-mm. *ApJ*, 769, L15.

Stone, J. M., Gardiner, T. A., Teuben, P., Hawley, J. F., & Simon, J. B. (2008). Athena: A New Code for Astrophysical MHD. *ApJS*, 178, 137–177.

Strong, A. W. & Moskalenko, I. V. (1998). Propagation of Cosmic-Ray Nucleons in the Galaxy. *ApJ*, 509, 212–228.

Susskind, L. (2003). Superstrings. *Physics world*, 16(11), 29.

Tang, Y.-W., Ho, P. T. P., Koch, P. M., Girart, J. M., Lai, S.-P., & Rao, R. (2009). Evolution of Magnetic Fields in High-Mass Star Formation: Linking Field Geometry and Collapse for the W51 e2/e8 Cores. *ApJ*, 700, 251–261.

Theuns, T., Leonard, A., Efstathiou, G., Pearce, F. R., & Thomas, P. A. (1998). P^3M-SPH simulations of the Lyalpha forest. *MNRAS*, 301, 478–502.

Thummalapalli, R. (2017). Fourier transform: Natures way of analyzing data. `http://www.yalescientific.org/2010/12/fourier-transform-natures-way-of-analyzing-data/`, (accessed 2017-03-29).

Toro, E. F. (2013). *Riemann solvers and numerical methods for fluid dynamics: a practical introduction*. Springer Science & Business Media.

Tóth, G. (2000). The $\nabla \cdot \mathbf{B} = 0$ constraint in shock-capturing magnetohydrodynamics codes. *J. Comput. Phys.*, 161(2), 605–652.

Tóth, G. (2000). The $\nabla\cdot$ B=0 Constraint in Shock-Capturing Magnetohydrodynamics Codes. *Journal of Computational Physics*, 161, 605–652.

Tricco, T. S. (2015). Simulating Astrophysical Magnetic Fields with Smoothed Particle Magnetohydrodynamics. *ArXiv e-prints 1505.04494*.

Tricco, T. S. & Price, D. J. (2013). A switch to reduce resistivity in smoothed particle magnetohydrodynamics. *MNRAS*, 436, 2810–2817.

Tricco, T. S., Price, D. J., & Federrath, C. (2016). A comparison between grid and particle methods on the small-scale dynamo in magnetised supersonic turbulence. *ArXiv e-prints*

*1605.08662*.

Tritsis, A., Panopoulou, G. V., Mouschovias, T. C., Tassis, K., & Pavlidou, V. (2015). Magnetic field-gas density relation and observational implications revisited. *MNRAS*, 451, 4384–4396.

Truelove, J. K., Klein, R. I., McKee, C. F., Holliman, II, J. H., Howell, L. H., & Greenough, J. A. (1997). The Jeans Condition: A New Constraint on Spatial Resolution in Simulations of Isothermal Self-gravitational Hydrodynamics. *ApJ*, 489, L179–L183.

Van Leer, B. (2006). Upwind and high-resolution methods for compressible flow: From donor cell to residual-distribution schemes. *Communications in Computational Physics*, 1(192-206), 138.

Vazquez-Semadeni, E., Ballesteros-Paredes, J., & Rodriguez, L. F. (1997). A Search for Larson-Type Relations in Numerical Simulations of the ISM: Evidence for Nonconstant Column Densities. *ApJ*, 474, 292.

Vishniac, E. T., Lazarian, A., & Cho, J. (2003). Problems and Progress in Astrophysical Dynamos. In E. Falgarone & T. Passot (Eds.), *Turbulence and Magnetic Fields in Astrophysics*, volume 614 of *Lecture Notes in Physics, Berlin Springer Verlag* (pp. 376–401).

Vogelsberger, M., Genel, S., Sijacki, D., Torrey, P., Springel, V., & Hernquist, L. (2013). A model for cosmological simulations of galaxy formation physics. *MNRAS*, 436, 3031–3067.

Vogelsberger, M., Genel, S., Springel, V., Torrey, P., Sijacki, D., Xu, D., Snyder, G., Bird, S., Nelson, D., & Hernquist, L. (2014a). Properties of galaxies reproduced by a hydrodynamic simulation. *Nat*, 509, 177–182.

Vogelsberger, M., Genel, S., Springel, V., Torrey, P., Sijacki, D., Xu, D., Snyder, G., Nelson, D., & Hernquist, L. (2014b). Introducing the Illustris Project: simulating the coevolution of dark and visible matter in the Universe. *MNRAS*, 444, 1518–1547.

Wang, P. & Abel, T. (2009). Magnetohydrodynamic Simulations of Disk Galaxy Formation: The Magnetization of the Cold and Warm Medium. *ApJ*, 696, 96–109.

White, C. J., Stone, J. M., & Gammie, C. F. (2016). An Extension of the Athena++ Code Framework for GRMHD Based on Advanced Riemann Solvers and Staggered-mesh Constrained Transport. *ApJS*, 225, 22.

Widrow, L. M., Ryu, D., Schleicher, D. R. G., Subramanian, K., Tsagas, C. G., & Treumann,

R. A. (2012). The First Magnetic Fields. *Space Science Reviews*, 166, 37–70.

WikiArt (2017). Lee krasner. `https://www.wikiart.org/en/lee-krasner/`, (accessed 2017-03-29).

Wurster, J., Price, D. J., & Bate, M. R. (2016). Can non-ideal magnetohydrodynamics solve the magnetic braking catastrophe? *MNRAS*, 457, 1037–1061.

Xu, G. (1995). A New Parallel N-Body Gravity Solver: TPM. *ApJS*, 98, 355.

Yee, K. (1966). Numerical solution of inital boundary value problems involving maxwell's equations in isotropic media. *IEEE Transactions on Antennas and Propagation*, 14, 302–307.

Zhu, C., Pakmor, R., van Kerkwijk, M. H., & Chang, P. (2015). Magnetized Moving Mesh Merger of a Carbon-Oxygen White Dwarf Binary. *ApJ*, 806, L1.

Zweibel, E. G. & McKee, C. F. (1995). Equiparatition of energy for turbulent astrophysical fluids: Accounting for the unseen energy in molecular clouds. *ApJ*, 439, 779–792.